Asteroseismology with 3D magneto-hydrodynamical simulations of stellar convection

Yixiao Zhou

A thesis submitted for the degree of
Doctor of Philosophy
The Australian National University

August 2021

I hereby declare that the work in this thesis is that of the candidate alone, except where indicated below or in the text of the thesis. The work was undertaken between February 2017 and January 2021 at the Australian National University (ANU), Canberra. It has not been submitted in whole or in part for any other degree at this or any other university.

This thesis has been submitted as a Thesis by Compilation in accordance with the relevant ANU policies. The main chapters are articles that are in review or published in a peer-reviewed astronomy journal. The status of each article and extent of the contribution of the candidate to the research and authorship is indicated below:

- Chapter 2: Yixiao Zhou, Martin Asplund and Remo Collet, The Amplitude of Solar p-mode Oscillations from Three-dimensional Convection Simulations, 2019, The Astrophysical Journal, 880:13.

  I (Y.Z.) led the project, with help and supervision from M.A. and R.C. The idea of this project was proposed by M.A. Y.Z. and R.C. developed the numerical techniques and produced the stellar models used in this work, and Y.Z. performed the post-processing of simulation data. All authors discussed the results and contributed to the writing of the manuscript.

- Chapter 3: Yixiao Zhou, Martin Asplund, Remo Collet and Meridith Joyce, Convective Excitation and Damping of Solar-like Oscillations, 2020, Monthly Notices of the Royal Astronomical Society, 495, 4904.

  Y.Z. led the project, with help and supervision from M.A., R.C. and M.J. The idea of this project was proposed by M.A. and Y.Z. Stellar atmosphere and interior models used in this study were generated by Y.Z. under the supervision of M.A. and R.C. Y.Z. combined the stellar atmosphere and interior models and did the asteroseismic analysis. All authors discussed the results and contributed to the writing of the manuscript.

- Chapter 4: Yixiao Zhou, Thomas Nordlander, Luca Casagrande, Meridith Joyce, Yaguang Li, Anish M. Amarsi, Henrique Reggiani and Martin Asplund, The relationship between photometric and spectroscopic oscillation amplitudes from 3D stellar atmosphere simulations, 2021, Monthly Notices of the Royal Astronomical Society, 503, 13.

  Y.Z. led the project under the supervision of T.N., L.C., M.J. and M.A. The idea of this project was proposed by M.A., Y.Z. and L.C. Y.Z. developed the stellar atmosphere models used in this work. Y.L. and Y.Z. analysed the luminosity power spectrum predicted from the stellar models. Y.Z., T.N., L.C. and M.J. contributed to the calculation of the bolometric correction. Spectral line formation calculations were carried out by T.N. and Y.Z. with the line formation code provided by A.M.A. and the model atom provided by H.R. Y.Z. did the radial velocity analysis, with the help from T.N., L.C. and M.J. All authors discussed the results and contributed to the writing of the manuscript.

Yixiao Zhou
30 August 2021

Acknowledgments

I want to express my highest gratitude to my supervisors Martin Asplund, Remo Collet, Meridith Joyce, Thomas Nordlander, Luca Casagrande and Christoph Federrath, for their valuable advices, guidance, inspiration and support on my PhD, and more importantly for teaching me how to do research in general. I am grateful to my collaborators Yaguang Li and Anish Amarsi for their valuable contributions and fruitful discussions. I have visited several research institutes in my PhD. I would like to thank Dennis Stello, Tim Bedding, Aaron Dotter, Saskia Hekker, Åke Nordlund and Stellar Astrophysics Centre at Aarhus University for their hospitality during my visit. I also want to express my thanks to people in my institute, especially to my officemates and astronomers in the GASP research group, for their help on research and programming.

This PhD thesis is dedicated to my mother Wei Wu, my father Yanming Zhou, my grandparents Huifen Wu and Xueyuan Tian and my partner Yao Wang, the people I love the most.

Abstract

The last decade has seen a rapid development in asteroseismology thanks to the CoRoT and *Kepler* missions. With more detailed asteroseismic observations available, it is becoming possible to infer exactly how oscillations are driven and dissipated in solar-type stars. To study this problem from a theoretical perspective, I carried out three-dimensional (3D) stellar atmosphere simulations together with one-dimensional (1D) stellar structural models of the Sun as well as key benchmark turn-off and subgiant stars. Mode excitation and damping rates are extracted from 3D and 1D stellar models based on analytical expressions. Mode velocity amplitudes are determined by the balance between stochastic excitation and linear damping, which then allows the estimation of the frequency of maximum oscillation power, $\nu_{\rm max}$, for the first time based on *ab initio* and parameter-free modelling. I have made detailed comparisons between my numerical results and observational data and achieved very encouraging agreement for all of the target stars. This opens the exciting prospect of using such realistic 3D hydrodynamical stellar models to predict solar-like oscillations across the Hertzsprung-Russell diagram, thereby enabling accurate estimates of stellar properties such as mass, radius, and age.

Solar-like oscillations can be observed in photometry and spectroscopy. The photometry method, represented by space-borne missions such as CoRoT, *Kepler* and TESS, detects stellar oscillations by measuring the variation of stellar luminosity. The spectroscopy method, represented by ground-based telescopes such as BiSON and SONG, use the wavelength shift of spectral lines as a probe to stellar oscillation. The relationship between the two types of measurement is of great importance, as it can not only guide asteroseismic observations but also serves as an additional constraint to stellar atmosphere models. I have carried out *ab initio*, 3D hydrodynamical numerical simulations of stellar atmosphere as well as realistic spectral line formation calculations to quantify the ratio between luminosity and radial velocity amplitude for the Sun and the red giant ϵ Tau. Luminosity amplitudes are computed based on the bolometric flux predicted by 3D simulations. Radial velocity amplitudes are determined from the wavelength shift of synthesized spectral lines with methods closely resemble BiSON and SONG observations. The resulting amplitude ratios are directly comparable with corresponding observations, and encouraging agreements between predicted and observed values are achieved for both the Sun and ϵ Tau. The numerical method presented here provides a novel way of simulating asteroseismic observations from detailed modelling and meanwhile opens an exciting prospect of bridging luminosity and radial velocity amplitude of solar-like oscillations with 3D stellar model atmospheres.

Contents

List of Figures

List of Tables

Chapter 1

Introduction

A significant fraction of our understanding of the Universe comes from stars. Observations of stars give us their distances, chemical compositions and ages, revealing the history of our Milky Way. Stars produce all elements heavier than lithium, which comprise the Earth and ourselves. The study of Cepheid stars and supernovae provides clues about the distances in the Universe. Stars are also natural laboratories to study some of the fundamental laws of physics. Of course, the foundation of all these prospects is our understanding of the stars themselves.

Stars are born from molecular clouds in the interstellar medium. Effects such as collision between molecular clouds and supersonic turbulence will create overdense regions which will collapse under the influence of gravity. The gravitational contraction process will eventually heat up the center of the cloud and form a very luminous protostar. Once the protostar reaches hydrostatic equilibrium, it enters the pre-main-sequence evolutionary phase. Owing to their high luminosity, stars in the beginning of pre-main-sequence are fully convective. As the temperature of a fully convective star must be above a certain value to fulfil the hydrostatic condition, a star in the early stage of the pre-main-sequence evolves with roughly constant surface temperature and decreasing luminosity. This pattern in the Hertzsprung-Russell (HR) diagram is referred as the Hayashi track. Along the Hayashi track the stellar luminosity decreases while the central temperature increases. For stars more massive than about $0.1M_{\odot}$, their central temperature will become high enough to ignite thermonuclear fusion of Hydrogen into Helium. When the star reaches a point where nuclear fusion completely dominates the energy production, it is said to be in the main-sequence phase of their evolution. Stars will spend a large fraction of their lifetime in the main-sequence phase.

The Sun is an example of a typical main-sequence star. The central temperature of the Sun is about 1.5×10^7 K. At this temperature, the source of nuclear energy generation is the proton-proton chain that converts Hydrogen into Helium. The inner 70 % of the Sun is radiative. Convection becomes the main energy transfer mechanism from roughly $0.7R_{\odot}$ to the solar optical surface.

Once Hydrogen in the stellar core is exhausted, the core starts to contract and the stellar envelope expands to transport the increasing luminosity (Applegate, 1988). Hydrogen burning now takes place at the Hydrogen shell surrounding the Helium core. At this time, the star has evolved off the main-sequence and enters the subgiant branch and subsequently the red giant branch. Red giant stars have large convection envelopes, therefore their evolution closely follows the Hayashi track as well.

As my work focuses on the evolution of solar-like stars in the main sequence and red giant phases, evolution after the red giant branch is beyond the scope of this thesis. I refer the interested reader to relevant textbook such as Kippenhahn & Weigert (1990) and Hansen et al. (2004) for comprehensive description of stellar evolution and structure in general.

All of the starlight visible to us comes from a thin layer around the stellar photosphere. What happens beneath the surface seems invisible and inaccessible. Fortunately, with the advances of modern science, the vibration of star can now be "heard" by modern telescopes from which we can then use to probe the stellar interior. The study of stellar oscillations to learn about the interiors of stars is called asteroseismology.

1.1 Asteroseismology

Musical instruments are created to make beautiful melodies, where the structure of the instrument is designed to enhance particular frequencies. Asteroseismology is, in some sense, an inverse of this mechanism: the purpose of "hearing" the star is to figure out the composition and structure of the instrument, that is, the star itself. In order to achieve this goal, one must understand how and why star oscillates.

Similar to musical instruments, stars have various modes of oscillation and tones. In general, a stellar oscillation is described by the mode displacement vector (Aerts et al. 2010 Chapter 3.3.1)

$$\delta\vec{r} = \mathfrak{Re}\left\{\left[\xi_r(r)Y_{lm}(\theta,\phi)\vec{e}_r + \xi_h(r)\left(\partial_\theta Y_{lm}(\theta,\phi)\vec{e}_\theta + \frac{1}{\sin\theta}\partial_\phi Y_{lm}(\theta,\phi)\vec{e}_\phi\right)\right]e^{-i\omega t}\right\}, \tag{1.1}$$

where r is radius, θ and ϕ are the polar and azimuthal angles, respectively. The term ω is angular frequency and t denotes time. The functions ξ_r and ξ_h are the amplitude functions (also named mode eigenfunctions from numerical point of view), and $Y_{lm}(\theta,\phi)$ are the spherical harmonic functions with l, m being the spherical degree and azimuthal order, respectively[1]. The numbers l, m, as well as the radial order n (that is, the number of zero point, exclude the center of the star, of ξ_r), characterise the normal modes in a spherically symmetric star. Radial component of $\delta\vec{r}$ for several example normal modes are schematically illustrated in Fig. 1.1. From Fig. 1.1 it is clear that $|m|$ is the number of node on an arbitrary semi-circle of latitude, while the number of surface nodes along a given longitude line equals to $l - |m|$. Oscillation modes with no radial node ($n = 0$) are called fundamental modes (f-modes), $n = 1, 2$ modes are called the first and the second overtone modes respectively, and so on (Aerts 2021 section I). For each radial number n, the purely radial mode is the special case of $l = 0$. In these scenarios, the star oscillates while preserving its spherical

[1] $\mathfrak{Re}\{f\}$ ($\mathfrak{Im}\{f\}$) means the real (imagery) part of complex function f.

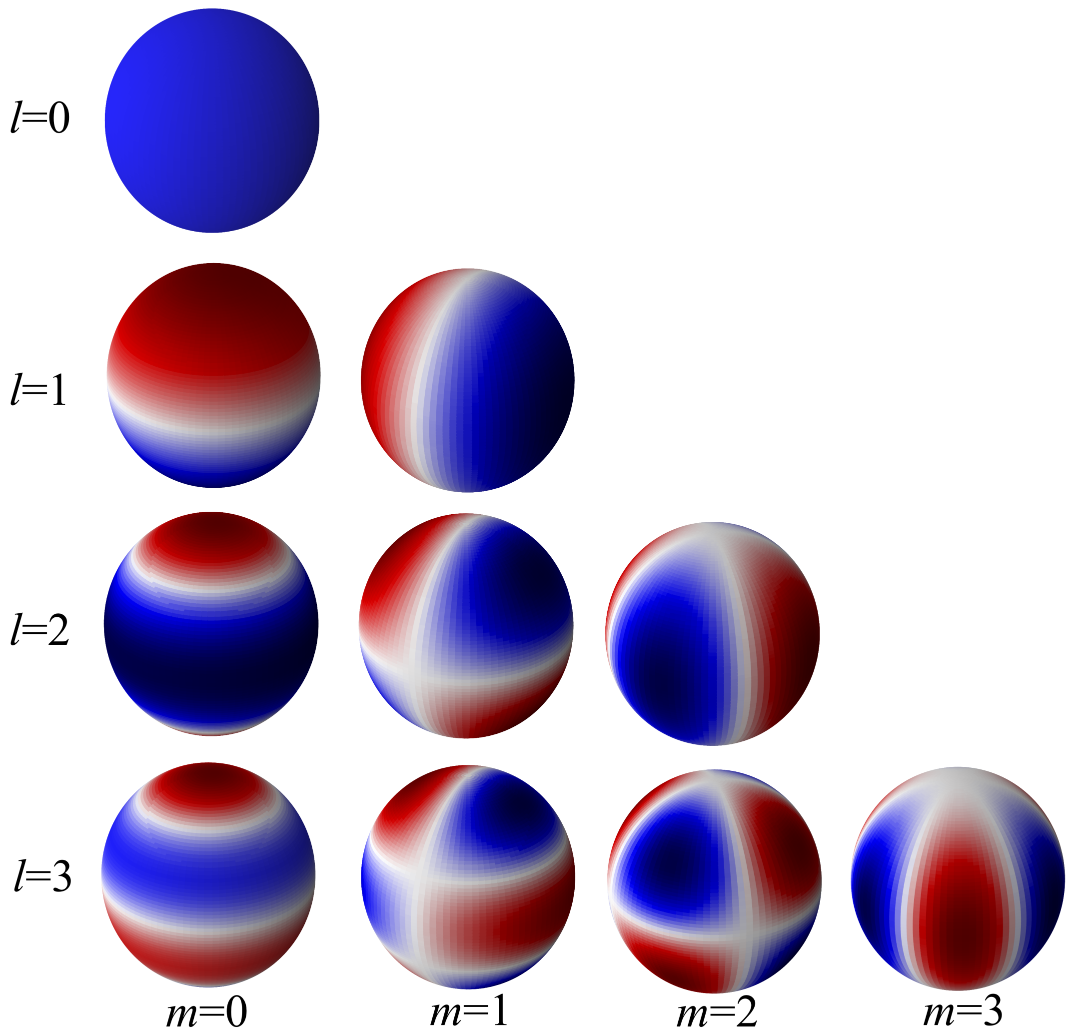

Figure 1.1: Radial component of the mode displacement vector for several example normal modes. The blue and red regions are moving inward/outwards, whereas the white lines are roughly the surface nodes. Note that at given radius, the radial component of normal mode are described by spherical harmonics.

symmetry at the same time. A special case is the $l = 0$ fundamental mode, in which the whole star simply expands and contracts. The other harmonics are called the dipole ($l = 1$), the quadrupole ($l = 2$), etc. Also, with same radial order n and degree l, there are $2l + 1$ distinct modes ($m = -l, -l + 1, ..., 0, ..., l - 1, l$) that have different azimuthal properties. For non-rotating stars, normal modes with same (n, l) have identical oscillation frequency. The frequency degeneracy breaks down in rotating stars, with the amount of frequency shift (compared to the non-rotating case) depend on m. This is called rotational splitting of oscillation modes.

1.1.1 Basic oscillation modes

Despite the richness of oscillation modes, they can be divided into two main categories for non-rotating spherical stars, namely, the pressure (or p) mode and the gravity (or g) modes.

Pressure-modes (p-modes) are standing sound waves that are trapped in the star. Sound waves are a basic physical phenomenon in any compressible fluid. A perturbation to compressible fluid will result in periodic compression and rarefaction in density ρ and pressure P at a given location. The oscillatory motion is sustained by pressure gradient which serves as a restoring force. Therefore, sound waves are also called pressure waves. The wave front propagates in the speed of sound, and the relationship between angular frequency ω, sound speed c_s and wave vector $\vec{k}$ (i.e. the dispersion relation) for sound wave is

$$\omega^2 = c_s^2 |\vec{k}|^2. \tag{1.2}$$

The frequency of stellar p-modes depends on the composition and structure of the star as well as the (n, l, m) number of the resonant mode in general.

The oscillation cavity of stellar p-mode depends mainly on its frequency and degree l. Detailed theoretical analysis (see, for example, Aerts et al. 2010 Chapter 3.4.2) shows that for p-modes, the radial amplitude function ξ_r is oscillatory when

$$|\omega| > \frac{\sqrt{l(l+1)}c_s}{r}, \tag{1.3}$$

and exponentially decay otherwise. Therefore, radial ($l = 0$) p-modes oscillate throughout the entire star, because (1.3) is always valid if $l = 0$. As sound speed increases from the stellar surface to the interior, non-radial ($l > 0$) p-modes are confined in the outer part of the star where (1.3) is satisfied. Also, for p-modes with similar oscillation frequency, modes with higher degree are confined to a narrower region of the outer stellar envelope. The fact that p-modes with different ω and l oscillate in different parts of the star enables accurate determination of structure and composition of stellar interior through asteroseismology (e.g. Basu et al. 2009).

Gravity modes (g-modes) are standing internal gravity waves in stars[2]. Internal

[2] There is also surface gravity wave that propagates at the surface of fluid. A familiar example is wind waves we see on the lake or sea.

gravity waves are present in the interior of a stratified fluid (that is, fluid under a gravitational acceleration g) with buoyancy being the restoring force. In a stable stratified fluid, if a fluid parcel is perturbed upward (e.g. toward the stellar surface), gravity will win over buoyancy and the net force will be downward, and vice versa. Therefore oscillatory motion is maintained. The dispersion relation for an internal gravity wave is (Aerts et al. 2010 Eq. 3.76)

$$\omega^2 = \frac{N^2}{1 + k_r^2/k_h^2}, \tag{1.4}$$

where k_r and k_h are the radial and horizontal wave numbers, respectively. The term N^2 is the square of buoyancy frequency (also called Brunt-Väisälä frequency). From Eq. (1.4) we can see that internal gravity waves cannot be purely radial; they must have a horizontal component ($k_h \neq 0$). Also worth noting is that the condition for stable stratification is $N^2 > 0$; negative N^2 leads to convection. This also provides insight about the oscillation cavity of g-modes: they oscillate in convectively stable regions while becoming evanescent in convection zones.

Since p- and g-modes emerge from different physical processes, they demonstrate distinct properties. First, as the radial order n increases the frequencies of the p-modes increase, but the frequencies of the g-modes decrease. Second, for high-overtone low-degree ($n \gg l$) modes, the asymptotic theory of stellar oscillation shows that p-modes are approximately equally spaced in frequency while g-modes are approximately equally spaced in period. Another difference between p- and g-mode is their oscillation cavity, as introduced above. For example, in the Sun, non-radial p-modes oscillate in the outer-most layers of the solar interior and decay exponentially in the inner part, whereas solar g-modes oscillate in the inner radiative region and decay exponentially in the surface convection zone. This discrepancy has a profound influence on helioseismology. As p-modes oscillate with higher amplitudes in the outer part of the Sun, the observed solar oscillations are mostly p-modes with radial orders $n = 20 - 30$ which have frequencies in the vicinity of five minute (the so-called solar five-minute oscillation). However, unambiguous detection of solar g-modes remains a long-standing problem in helioseismology (see Appourchaux et al. 2010 for a review on this problem).

Apart from p- and g-modes, there are other categories of oscillation modes, for example, the toroidal mode. In non-rotating stars, the displacement vector of toroidal mode satisfies $\xi_r = 0$ and $\nabla \cdot \delta\vec{r} = 0$ (Papaloizou & Pringle, 1978), which means toroidal modes do not have a radial component and cause no compression or expansion hence cannot be detected. In rotating stars, however, the toroidal mode couples with the Coriolis force and is referred as a Rossby mode (r-mode). R-modes in rotating stars were first detected by Van Reeth et al. (2016).

In this thesis, I focus primarily on radial p-modes.

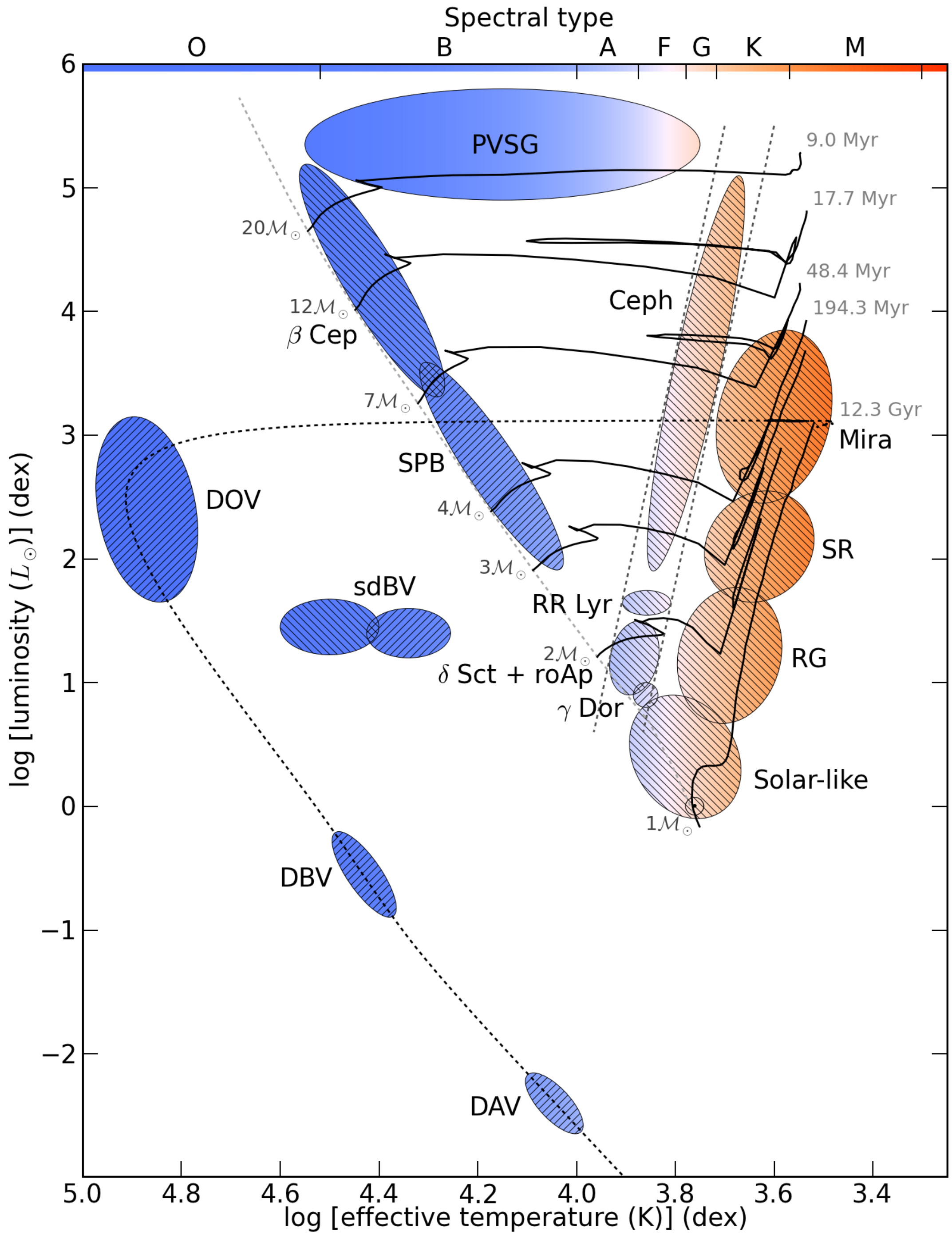

Figure 1.2: A pulsation HR diagram showing various types of variable stars and their location within the HR diagram. The spectral type are colour-coded as indicated in the top of the figure. Evolution tracks for different stellar masses are depicted in solid black lines, while the grey dotted line marks the position of the zero-age-main-sequence. Two parallel vertical black dotted lines denotes the classical instability strip. The symbol "\\" represents that a certain type of star oscillates with p-mode while "//" represents g-mode. Figure from Schmid (2018, their Fig. 1.5), see also Fig. 1.12 of Aerts et al. (2010).

1.1.2 Stellar oscillation across the HR diagram

Stellar variability is ubiquitous across the HR diagram. As shown in the "pulsation HR diagram" 1.2, p- or g-mode oscillations can be found in pre-main-sequence stars, low and high mass main-sequence stars, red giants, stars in horizontal branch, as well as compact stars such as white dwarfs. The frequency and amplitude of oscillations provide valuable information about the physical processes taking place in the stellar interior, thereby opening a new channel to study stars across the HR diagram.

In the low-mass end of Fig. 1.2 resides our Sun. The Sun is an oscillating star that shows a wide spectrum of p-mode oscillations with amplitudes on the order of 10 cm/s. Thanks to the CoRoT (Michel et al., 2008), *Kepler* (Borucki et al., 2010) and TESS (Ricker et al., 2015) space missions, thousands of solar-like oscillating stars have now been found, including solar-type main-sequence stars, subgiants and red giants. These solar-like oscillators are typically in the F, G, and K spectral classes with effective temperature $T_{\rm eff}$ ranges from 4000 to 7000 K and stellar masses between 0.8 and 1.5 $M_{\odot}$. Solar-like oscillations are p-modes driven stochastically by convective turbulence in surface convection zone. In principle, these oscillations should present in every star with a surface convection zone. I will discuss solar-like oscillation in detail in Sect. 1.1.3.

Moving upwards and left along the main-sequence takes us to another type of pulsating stars, the γ Dor. γ Dor stars are A and F stars with masses ranging from approximately 1.5 to 1.8 $M_{\odot}$ and effective temperatures typically between 6500 and 7500 K. γ Dor stars do not show stochastically excited p-modes but oscillate in high-order g-modes. The unstable g-modes have amplitudes on the order of 1 km/s, much larger than p-mode oscillations observed in the Sun. As first proposed by Guzik et al. (2000), these high-order g-modes are excited by the "convective flux blocking" mechanism that operates at the bottom of their surface convection zone where abrupt transition from radiative to convective heat transport takes place. The convective time scale (pressure scale height divided by the convective velocity) at the base of the surface convection zone is comparable with the period of g-mode, therefore makes mode excitation efficient. The suggested excitation mechanism was later confirmed by Dupret et al. (2005) using the time-dependent convection model of Grigahcène et al. (2005). In addition, γ Dor stars are usually fast rotators therefore permitting r-mode oscillations to be detected (Van Reeth et al., 2016; Li et al., 2019).

Another group of oscillating stars with $T_{\rm eff}$ slightly higher than γ Dor, but which still oscillate via p-modes, are δ Sct stars. They are A or F type main-sequence stars located in the classical instability strip. The effective temperatures of δ Sct stars are typically between 7000 and 8000 K. In this temperature range, the stellar surface convection zone is very thin or may even disappear, therefore it is unlikely to find stochastically excited p-modes in δ Sct stars. Instead, the observed p-mode oscillations are driven by the opacity mechanism, which is frequently called κ-mechanism because κ usually denotes opacity. The κ-mechanism works on the region where the opacity increase notably with increasing temperature. In such region, if gas sinks inward it becomes denser, hotter and more opaque, and hence impedes radiation transfer. Consequently, the layer below the gas heats up and its pressure increases, thereby pushing the gas outward. When the gas expands, the temperature and opacity reduce so that radiation can pass through, then gravity dominates over radiation and pulls the gas back in. The result is that gas moving inward and outward periodically. For δ Sct stars, pulsations driven by the κ-mechanism typically occur in the second Helium ionization zone (see Houdek & Dupret 2015 Fig. 5).

Moving up further along the classical instability strip, we find RR Lyrae and Cepheid stars. The Cepheid star δ Cephei is the first known variable star, discovered by John Goodricke in 1784. Cepheid stars typically oscillate with a single mode, usually the fundamental or the first overtone radial mode excited via the κ-mechanism. This does not provide adequate information about their interior structure, so that RR Lyrae and Cepheid stars are not perfectly suitable for asteroseismic studies. Nevertheless, their period-luminosity relation makes them ideal distance indicators for the Universe, i.e. the "standard candle". Cepheid and RR Lyrae stars are therefore of great importance in galactic astronomy and cosmology. Although RR Lyrae and Cepheid have many similarities, it is worth noting that RR Lyrae stars are metal poor, $0.6 - 0.8 M_{\odot}$ stars in the horizontal branch of their evolution, whereas Cepheid are much more massive stars (greater than $5 M_{\odot}$) in their blue loop phase of evolution[3].

Other types of oscillating stars including slowly pulsating B (SPB) stars, which are intermediate mass B type stars that show g-mode oscillation; β Cep stars, which are intermediate and high mass main-sequence stars that oscillates in both p- and g-mode; pulsating white dwarfs (DAV, DBV, DOV) which oscillate in g-mode. I refer the reader to chapter 2 of Aerts et al. (2010) for a thorough introduction of these topics. This thesis contributes to the understanding of solar-like oscillations, which I discuss in detail in the subsequent section.

1.1.3 Solar-like oscillations

Asteroseismology starts with helioseismology. The study of solar oscillation has a history of more than half a century. The first groundbreaking progress was made by Leighton et al. (1962), who measured the Doppler velocity field in the solar atmosphere. They found large cells of horizontally moving material in the scale of 10 Mm, which are now referred as supergranulation. In addition, the measured vertical velocity field shows periodicity with a period of approximately 5 minutes and the velocity amplitude is in the order of 1 km/s.

The discovery by Leighton et al. (1962) marks the dawn of helioseismology. The oscillation in the solar atmosphere was then linked to standing sound waves by Ulrich (1970). Inspired by the key insight from Ulrich (1970) that the observed photospheric fluctuations are caused by standing sound waves trapped in the solar interior, Ando & Osaki (1975) computed the eigenfrequency and the stability of nonradial normal modes of the Sun using their theoretical formulations for non-adiabatic stellar oscillation. Their theoretical angular frequency - wave number ($\omega - k$) rela-

[3]The blue loop is an evolutionary phase right after the red giant branch for stars with mass between roughly $5 M_{\odot}$ and $8 M_{\odot}$ (Walmswell et al., 2015).

tionship agrees well with the corresponding observational results by Deubner (1975). Two years later, In the same period, Stein & Leibacher (1974) and Goldreich & Keeley (1977b) proposed that solar p-modes are excited by turbulent convection, which is now the widely accepted excitation mechanism for solar-like oscillations. The global oscillation of the Sun was first confirmed by Claverie et al. (1979) and Grec et al. (1980). The former measured the Doppler velocity shift over the whole solar disk using a spectrograph which is the prototype of the BiSON (Birmingham Solar Oscillations Network, Chaplin et al. 1996) instrument, while the latter performed full disk observations of the Sun with a spectrograph located at the South Pole. It is therefore reasonable to state that the basis of helioseismology was established in the 1970s, when solar oscillations were unambiguously detected and preliminarily understood.

The discovery of solar oscillations opened a unique window to probe the interior condition of the Sun. As different p-modes oscillate in different cavities of the Sun, the observed oscillation frequencies can be used to infer the properties of the entire solar interior. This technique is called helioseismic inversion, see Gough (1985) and Christensen-Dalsgaard (2002) for a review of this field. A basic application of helioseismic inversion is to infer the solar internal rotation through the rotational splitting of p-modes. The result of this inversion shows that the solar radiative zone rotates nearly uniformly, and the bottom boundary of the solar convection zone (the tachocline) appears to be a transition region between the uniformly rotating radiative zone and the differentially rotating convection zone. The finding that the solar tachocline is in fact a shear layer has a profound impact on solar physics and provided some clues to the generation of the solar large scale dynamo. A comparatively more challenging problem in heliosiesmic inversion is to constrain the solar interior structure through oscillation frequencies. This was achieved by Christensen-Dalsgaard et al. (1985), who quantified the solar sound speed as a function of radius. Based on the inferred sound speed, Christensen-Dalsgaard et al. (1991) and Basu & Antia (1997) accurately determined the size of solar convection zone. In addition, solar oscillations also tightly constrain the abundance of Helium (cf. Basu & Antia 1995 and Houdek & Gough 2007), which is difficult to measure using spectroscopy.

Helioseismology has revolutionized our understanding of the Sun by revealing the structure, composition and dynamics of its interior. Therefore, a natural motivation is to apply the techniques used in helioseismology to other stars. It is anticipated that all stars with a surface convection zone will show a broad spectrum of stochastically excited p-modes, i.e. solar-like oscillations, from which we can infer their interior properties as we did for the Sun. The search for solar-like oscillation in other stars began in the 1990s. The first evidence of solar-like oscillations in other stars was presented by Brown et al. (1991), who found the signature of p-modes in Procyon A from the Doppler velocity measurement[4]. The oscillation in Procyon A was unambiguously confirmed by Arentoft et al. (2008) and Bedding et al. (2010). Kjeldsen et al. (1995) reported oscillations in the G type subgiant η Boo based on the

[4]In the same paper, they also proposed that the frequency of maximum oscillation power, $\nu_{\rm max}$, scales with $g/\sqrt{T_{\rm eff}}$, which is the basis of the seismic scaling relation widely used in asteroseismology. I will discuss this topic in some detail in Sect. 1.1.3.2.

change of equivalent width of the Balmer lines, which is the first definite detection of solar-like oscillation in other stars. In the following years, solar-like oscillations were found in several nearby bright stars including α Cen A and B (Bouchy & Carrier, 2001, 2003; Bedding et al., 2004; Kjeldsen et al., 2005), the subgiant β Hyi (Bedding et al., 2001) and the red giant ξ Hya (Frandsen et al., 2002), marking the beginning of asteroseismology of solar-type stars. I refer the readers to Bedding & Kjeldsen (2003) for a review of observational progresses in the early days of asteroseismology.

Until about 2010, only a handful of solar-like oscillating stars were confirmed (see Fig. 2.2 of Aerts et al. 2010 for a clear illustration). However, over the past decade, oscillations in thousands of solar-type main-sequence stars, subgiants and red giants have been detected by the CoRoT (Convection, Rotation and planetary Transits), *Kepler* and TESS (Transiting Exoplanet Survey Satellite) satellites. These space-based telescopes have paved the way to a new epoch of ensemble asteroseismology. With more detailed asteroseismic observations available in recent days, it is important to fully understand how oscillations are driven and dissipated in solar-type stars. I introduce the basics about this topic in the subsequent section. The theoretical formulation and numerical technique used for quantifying the excitation and damping of solar-like oscillation will be detailed in chapters 2 and 3.

1.1.3.1 Excitation and damping of solar-like oscillations

According to the law of conservation of energy, oscillations cannot emerge by themselves. To make oscillations possible, energy must be injected into the modes via driving mechanisms. At the same time, oscillation modes continually lose their energy through the damping effects. Therefore, the observed oscillation can only continue if there is a balance between mode driving and damping. There are two major driving mechanisms of stellar oscillations, the κ-mechanism, which I briefly introduced in Sect. 1.1.2, and the stochastic driving mechanism. Stochastic driving is in essential the coupling between convection and oscillation. Just like tuning forks will vibrate in a noisy environment, oscillations in solar-like stars are excited when their intrinsic vibration frequencies (normal modes) resonance with stochastic noise caused by convective motion.

I start with the general case where a damped linear oscillator is subject to external forcing. The equation of motion of the oscillator is written as

$$\frac{d^2a(t)}{dt^2} + 2\eta\frac{da(t)}{dt} + \omega_0^2 a(t) = f(t), \tag{1.5}$$

where $a(t)$ represents displacement and ω_0 is the angular frequency in the case of free (undamped, no external forcing) oscillation. The function $f(t)$ is the forcing function, while η denotes damping rate (or growth rate if $\eta < 0$). This differential equation can be solved using the Fourier transform method, giving

$$A(\omega) = \frac{F(\omega)}{(\omega^2 - \omega_0^2) - 2i\eta\omega}, \tag{1.6}$$

where $F(\omega)$ and $A(\omega)$ are the Fourier transforms of functions $f(t)$ and $a(t)$, respectively. Eq. (1.6) suggests that we can predict the oscillation amplitude if both the forcing function and the damping rate are available. Another important issue is the stability of the star to oscillation. Specifically, consider the simplest scenario where there is no external forcing ($f = 0$), the solution of Eq. (1.5) has the form $a(t) \propto \exp(-i\omega t - \eta t)$. Therefore, the sign of damping rate η dictates the (linear) stability of oscillation. Positive η means the oscillation is damped, whereas negative η suggests the star is unstable to oscillation, also referred as "self-excited" oscillations.

In the context of solar-like oscillations, determining the forcing function, which characterizes the mode excitation process, and the damping rate are of great importance, as they not only allow a prediction of oscillation amplitudes but also reveal the stability of oscillation modes. The quantification of mode excitation and damping requires a realistic model of near-surface convection. The model should also take into account the interaction between convection and oscillation, which is a particularly challenging problem, as it is well known that the description of convection is a notable shortcoming in stellar physics.

Nevertheless, considerable efforts have been made to fully understand how solar-like oscillations are excited and damped. Following the key insight by Goldreich & Keeley (1977a,b) that solar p-mode oscillations are driven by turbulent convection and dissipated by turbulent viscosity, Balmforth (1992a,b) analytically quantified the excitation rate (or energy injection rate) and damping rate of solar p-modes using the non-local time-dependent mixing length theory of convection developed by Gough (1977) and Balmforth (1992a). The non-local theory does not rely on the questionable assumption that the mixing length L is much smaller than the scale height of the stellar envelope, which is usually violated in solar-type and red giant stars. The analytical treatment of mode excitation and damping of Balmforth (1992a,b) included the contribution from both the convective turbulence and the entropy fluctuation (i.e. non-adiabatic effects). Their results agreed reasonably well with helioseismic observations and showed that solar oscillations are stable. Based on Balmforth (1992a)'s theoretical formulation, Houdek et al. (1999) studied excitation, damping rates and velocity amplitudes of solar-like oscillations for the Sun and a grid of 1D models that corresponds to main-sequence stars. Their results indicate that oscillations in solar-type main-sequence stars are stochastically driven and intrinsically damped by convection, as in the case of the Sun. Another non-local time-dependent convection theory was developed by Gabriel (1996) and Grigahcène et al. (2005) following the original ideas of Unno (1967). This theoretical formulation was adopted by Dupret et al. (2009) and Belkacem et al. (2012) to evaluate p-mode damping rates for solar-type main-sequence and red giant stars. Good agreements were achieved between their theoretical damping rates and the corresponding CoRoT and *Kepler* observations.

These and other studies (e.g. Goldreich et al. 1994 and Xiong et al. 2000, see also Houdek & Dupret 2015 for a comprehensive review of this topic) have greatly improved our understanding of how p-modes in solar-type stars are driven and damped. However, due to the lack of a realistic theory of convection, the theoretical prescriptions adopted in these works inevitably involve adjustable parameters, making independent theoretical predictions of excitation and damping difficult. An alternative approach that has shown great promise for overcoming this difficulty is to evaluate excitation and damping rates from first principles using 3D hydrodynamical convection simulations. Nordlund & Stein (2001) and Stein & Nordlund (2001) extracted the excitation rates of solar radial modes directly from 3D simulations of near-surface layers of the solar convective zone. This *ab initio* numerical approach was further applied by Stein et al. (2004) to study the excitation of p-mode oscillations for several F, G, K type stars across the HR diagram. Meanwhile, the 3D near-surface convection simulations were used to constrain the analytical model of p-mode excitation. For stars investigated in Samadi et al. (2003, 2007), the turbulent spectrum in Samadi & Goupil (2001)'s mode excitation model was constrained by the corresponding 3D simulation. In this thesis, I expand the idea of using 3D near-surface convection simulations to quantify the mode excitation process and further explore the possibility of modelling the damping of solar-like oscillations based on 3D simulations in a parameter-free manner.

1.1.3.2 The seismic scaling relation

The knowledge of how and why stars oscillate, in conjunction with observed oscillation frequencies and amplitudes, will allow us to infer the structure and properties of stars. One of the most important applications of asteroseismology is the determination of basic stellar parameters, such as radius, mass and age. These fundamental parameters are of great significance not only for stellar physics but also for astronomy in general. For instance, in planetary science, well-measured stellar parameters are prerequisites for determining the habitability of potential exoplanet hosts. Moreover, coupling stellar parameter measurements with large spectroscopic surveys will provide strong constraints on the age – radial velocity and age – metallicity relations in different parts of the Milky Way, therefore enabling us to reveal the kinetics and evolution of our Galaxy (see e.g., Casagrande et al. 2016). A classical approach to this problem is to measure the relative luminosity (in solar units) and temperature of a star, then its radius is calculated from the definition of luminosity and its mass can be extracted from the HR diagram. An alternative and complementary method is asteroseismology. For solar-like oscillating stars, the stellar mass M and radius R can be inferred from the relations (Ulrich, 1986; Brown et al., 1991; Kjeldsen & Bedding, 1995)

$$\Delta\nu \propto \sqrt{\bar{\rho}} = \left(\frac{M}{\frac{4}{3}\pi R^3}\right)^{1/2}, \tag{1.7}$$

$$\nu_{\rm max} \propto \nu_{\rm ac} \propto \frac{g}{\sqrt{T_{\rm eff}}} \propto \frac{M}{R^2\sqrt{T_{\rm eff}}}. \tag{1.8}$$

Here the asteroseismic parameters $\Delta\nu$ and $\nu_{\rm max}$ are the observed large frequency separation and frequency of maximum power, respectively, while $\nu_{\rm ac}$ is the acoustic cut-off frequency. $\bar{\rho}$, g and $T_{\rm eff}$ are mean density, surface gravitational acceleration and effective temperature of the star. To compute (1.7) and (1.8), it is beneficial to choose a reference star. Because properties of the Sun are measured to the greatest accuracy and precision of any star, it is natural to scale from the solar case to predict $\Delta\nu$ and $\nu_{\rm max}$ for an arbitrary star. This motivation gives rise to the so-called seismic scaling relations:

$$\frac{\Delta\nu}{\Delta\nu_\odot} \simeq \left(\frac{M}{M_\odot}\right)^{1/2} \left(\frac{R}{R_\odot}\right)^{-3/2}, \tag{1.9}$$

$$\frac{\nu_{\rm max}}{\nu_{\rm max,\odot}} \simeq \left(\frac{M}{M_\odot}\right) \left(\frac{R}{R_\odot}\right)^{-2} \left(\frac{T_{\rm eff}}{T_{\rm eff,\odot}}\right)^{-1/2}, \tag{1.10}$$

where the subscript "$\odot$" represents properties that are associated with the Sun. In the same way, if both $\Delta\nu$ and $\nu_{\rm max}$ of a star are available, Eq. (1.9) and (1.10) can be applied to estimate the mass and radius of this star (Stello et al., 2008; Kallinger et al., 2010). To make it clear, I rearrange these equations for mass and radius:

$$\begin{aligned} \frac{R}{R_\odot} &\simeq \left(\frac{\nu_{\rm max}}{\nu_{\rm max,\odot}}\right) \left(\frac{\Delta\nu}{\Delta\nu_\odot}\right)^{-2} \left(\frac{T_{\rm eff}}{T_{\rm eff,\odot}}\right)^{1/2}, \\ \frac{M}{M_\odot} &\simeq \left(\frac{\nu_{\rm max}}{\nu_{\rm max,\odot}}\right)^{3} \left(\frac{\Delta\nu}{\Delta\nu_\odot}\right)^{-4} \left(\frac{T_{\rm eff}}{T_{\rm eff,\odot}}\right)^{3/2}. \end{aligned} \tag{1.11}$$

In the last decade, thanks to the space-based telescopes CoRoT, *Kepler* and TESS, the measurement of asteroseismic observables $\Delta\nu$ and $\nu_{\rm max}$ is now possible for thousands of solar-like oscillating stars. The seismic scaling relations (1.11) then give the stellar mass and radius directly. This method has been extensively employed and yields satisfactory results. For example, with asteroseismic observables from the *Kepler* data, Chaplin et al. (2011) applied the seismic scaling relation as a first estimation of stellar masses and radii for over 500 solar-type stars. The reliability of the seismic scaling relation was tested by Huber et al. (2017) and Zinn et al. (2019), who compared the seismic radii derived from (1.11) with Gaia radii (both DR1 and DR2) and concluded that systematic errors in seismic radii are $\lesssim 5\%$ for stars with $R \approx 0.8 - 10\,R_\odot$ (see also Mosser et al. 2010).

Despite the wide use of the seismic scaling relations in stellar physics, they are not expected to be completely accurate because several approximations and assumptions are involved in their derivations. Moreover, a side effect of calibrating $\Delta\nu$ and $\nu_{\rm max}$ on the Sun is that the validity of the seismic scaling relation cannot be guaranteed for stars that have evolutionary stages or metallicities significantly different from the Sun. This is indeed confirmed by Epstein et al. (2014), who found that stellar masses calculated from the seismic scaling relation is higher than expected for nine metal-poor red giants. Their results may suggest the limitation of the seismic scaling relation for metal-poor red giants which is of great importance in Galactic archaeology.

This motivates us to test the validity of the seismic scaling relations from a theoretical prospective. Because the large frequency separation, the stellar mass, radius and effective temperature are all computable from theoretical stellar model, the most challenging part is the determination of $\nu_{\rm max}$. In this thesis, I calculate both the excitation and damping rate at different oscillation frequencies for solar-like oscillating stars, from which we can predict their oscillation power spectrum and obtain the theoretical $\nu_{\rm max}$ value. I show that my methodology is valid for a wide range of stellar parameters, and thereby opens the possibility to quantify the departure, if any, from the widely used seismic scaling relations from an entirely theoretical angle.

1.1.4 Observational techniques

Stellar oscillations can be observed via spectroscopy and photometry. In the spectroscopic method (also called the radial velocity method) of measuring stellar oscillations, variations in the radial (i.e. line-of-sight) velocity near the stellar photosphere are quantified by analysing the Doppler shift of certain spectral lines. The photometric method measures variations in the brightness of stars (often in a certain bandpass), which reflects the fluctuation of surface temperature due to stellar granulation and oscillations. The spectroscopic method is typically used by ground-based telescopes such as BiSON, High-Accuracy Radial velocity Planetary Searcher[5] (HARPS, Mayor et al. 2003) and the Stellar Oscillations Network Group (SONG, Grundahl et al. 2006). These instruments are able to achieve a radial velocity precision less than 1 m/s. Their detailed observations of stellar oscillations have laid the groundwork for helioseismoloy and asteroseismology (Claverie et al., 1979; Brown et al., 1991; Bedding et al., 2001).

Meanwhile, the space missions CoRoT, *Kepler* and TESS detect stellar oscillations by measuring variations in stellar luminosity. The high-quality, long time-series, extensive photometric data provided by these space-based telescopes enable accurate determination of oscillation frequencies and amplitudes for thousands of solar-like stars, thus ushering in the era of ensemble asteroseismology.

Both the spectroscopic and photometric methods have their benefits and weaknesses. For example, in the low-frequency regime, the photometric method is impaired by signals due to stellar atmospheric convection (stellar granulation), which impedes the characterisation of low-frequency oscillations. This difficulty can be avoided by observing the star using the radial velocity method, as stellar granulation noise is significantly less pronounced in radial velocity signals. Moreover, the radial velocity method has demonstrated great potential for measuring oscillations in cool dwarf stars such as α Cen B (Kjeldsen et al., 2005), which are important in exoplanet science but difficult to detect with space-based photometry due to their low intrinsic luminosity and small oscillation amplitude (Huber et al., 2019). Nonetheless, ground-based spectroscopy is limited by target brightness and the Earth's atmosphere, thus making it inferior to space-photometry in these aspects.

It follows that the spectroscopic and photometric methods of measuring stellar oscillations are highly complementary and that combining the two methods will

[5]Operates at the ESO La Silla 3.6m telescope.

yield extra information that can further constrain the properties of stars. With the commencement of the TESS mission and SONG observations, many stars will soon have both luminosity and radial velocity data available. Therefore, investigating the relationship between luminosity and radial velocity amplitude is of increasing importance. I will study this problem in detail in this thesis.

1.2 Three-dimensional stellar convection modelling

Solar-like oscillations are stochastically excited by turbulent convection near the stellar surface. The complex interplay between oscillations, convection and other details such as radiative transfer, opacities and equation of state means that a computational approach is the only feasible way to study the excitation and damping of solar-like oscillations quantitatively. In this subsection, I discuss the physical picture of stellar surface convection (Sect. 1.2.1) and the necessity of using 3D hydrodynamical simulations for asteroseismology (Sect. 1.2.2).

1.2.1 Stellar surface convection

Stars are powered by fusion taking place in their central regions. The energy generated by nuclear reactions travels through the stellar interior, then reaches the stellar surface and radiates as the starlight we see. Energy is transported by one of three ways: radiation, convection, and conduction, or some combination thereof. Conduction is important for materials in a solid state. In the astrophysical context, conduction happens in the cores of massive stars, white dwarfs, and neutron stars where electron degeneracy and crystallization takes place. Radiative and convective energy transport are commonly present in solar-type, subgiant and red giant stars, like those investigated in this thesis. Radiative transfer of energy is associated with the interaction between thermal motion and electromagnetic radiation. Macroscopically, it is characterised by the opacity of gas. A higher opacity means it is more difficult for photons to pass through the medium, therefore leading to a steeper temperature gradient. In the simple case of homogeneous chemical composition, once the temperature gradient $d\ln T/d\ln P$ exceeds the adiabatic temperature gradient $(d\ln T/d\ln P)_s$, where the subscript s denotes constant entropy, the fluid becomes unstable to convection (the Schwarzschild criterion for convection). At this point, convective heat transport is activated. Convection manifests itself as macroscopic flow of fluid elements: it is a subtle heat transport mechanism that combines the effects of gravity and buoyancy. A simple physical picture is that fluid bubbles that are warmer than their surrounding gas tend to move towards lower temperatures, where they lose their heat and then sink down to the higher temperature regime. Heat is transferred by such "cycles".

All solar-like oscillating stars harbour a surface convection zone extending from some point in the stellar interior all the way to the optical surface. Therefore, modelling stellar surface convection is crucial for the understanding of stellar structure and evolution, as well as how spectral lines are formed near the photosphere. Understanding surface convection zones is of fundamental importance in the study of solar-like oscillations because they are ultimately driven by convection.

The study of stellar convection through numerical simulation spans decades. The most widely used theory is the mixing length theory (MLT) of convection developed by Erika Böhm-Vitense (1958). The MLT is a phenomenological model motivated by the intuition that in convective regions, a rising fluid parcel will conserve its properties over some vertical length L, before mixing with the surrounding gas. As the MLT is simple and suitable for numerical calculation, it has been adopted in a variety of stellar evolutionary codes (such as PARSEC Bressan et al. 2012 and MESA Paxton et al. 2011) and stellar atmosphere codes (such as ATLAS Kurucz 1979 and MARCS Gustafsson et al. 2008). The MLT performs well in the deep convection region where the temperature gradient is very close to adiabatic. Despite its popularity and success, the MLT includes several free parameters which need to be calibrated from observations or numerical simulations (Ludwig et al., 1999; Trampedach et al., 2014b; Magic et al., 2015; Joyce & Chaboyer, 2018). The most representative free parameter is the mixing length parameter $\alpha_{\rm MLT} = L/H_P$, where $H_P = (d\ln P/dr)^{-1}$ is the local pressure scale height. The physical picture of convection described by the MLT is only approximate as well. As is clear from 3D hydrodynamical simulations (e.g. Nordlund et al. 2009), convective regions show finger-like downflows rather than distinct and coherent fluid parcels. Additionally, there are discrepancies between observations and stellar models constructed based on MLT. It was found that the theoretical p-mode frequencies computed with the standard solar model do not match the measured values at high frequencies (Christensen-Dalsgaard et al., 1996), which is due to the inadequate description of the near-surface convection zone by MLT. This is the so-called asteroseismic "surface effect", and it cannot be reconciled by adjusting the $\alpha_{\rm MLT}$ value or change to other formulation of stellar convection (e.g., the full turbulence spectrum theory by Canuto & Mazzitelli 1991).

Developing a highly realistic theory of stellar surface convection is particularly challenging, as convection is inherently a 3D dynamical process. Near the stellar surface, the fluid is highly non-adiabatic, non-local and the convective turbulence is strong. These factors further complicate the problem. A promising approach to overcome these difficulties is to construct 3D, time-dependent, radiative hydrodynamical simulations of surface convection by numerically solving the hydrodynamical equations coupled with the equation of radiative transfer. I introduce such 3D simulations in the following subsection.

1.2.2 3D radiative hydrodynamical simulation

Numerically solving the radiative hydrodynamical equations of fluid motion is a promising approach to realistically describing the physical processes within the stellar surface convection zone. The general equations governing a non-relativistic fluid

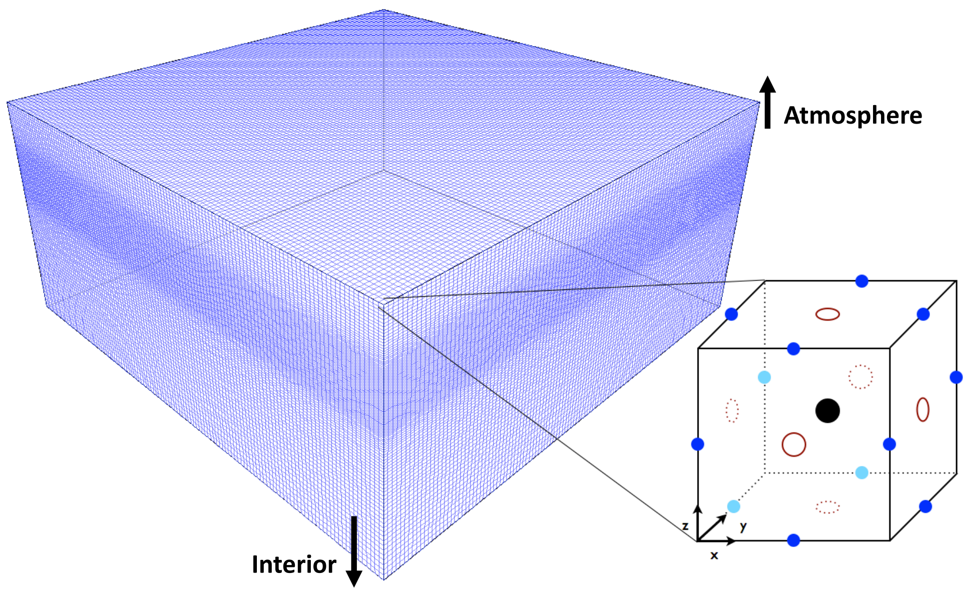

Figure 1.3: The large blue rectangular box illustrates a typical simulation domain with the Stagger code. I demonstrate also an enlarged view of an individual cell (small black cube). Scalar values are defined at the cell center (black dot), while the momentum density and magnetic fields are located at the cell faces (red circles), and the electric field at the cell edges (blue dots). Figure from Magic (2014) Fig. 2.1.

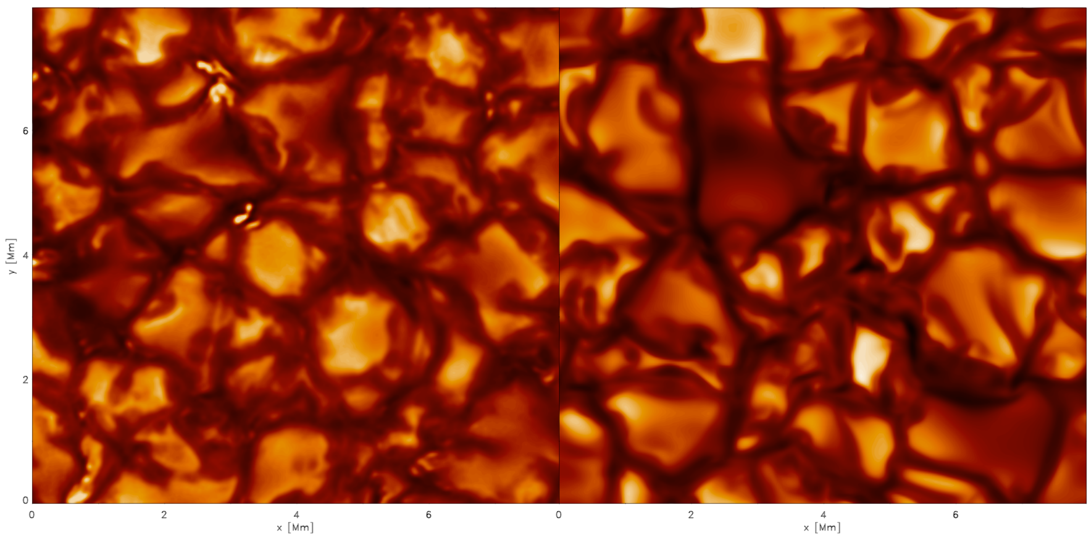

Figure 1.4: Granulation pattern observed with the Swedish Solar Telescope (left panel, resolution is 25 km) is compared with the emergent intensity predicted from the 3D solar simulation (right). The observation and simulation are nearly indistinguishable. Figure from Magic (2014, their Fig. 1.2).

are

$$\frac{\partial \rho}{\partial t} = -\nabla \cdot (\rho \vec{v}), \tag{1.12}$$
$$\frac{\partial \rho \vec{v}}{\partial t} = -\nabla \cdot (\rho \vec{v} \otimes \vec{v} + \mathbf{T}) - \nabla P_{\text{ther}} + \vec{J} \times \vec{B} + \rho \vec{g}, \tag{1.13}$$
$$\frac{\partial \vec{B}}{\partial t} = -\nabla \times \vec{E}, \tag{1.14}$$
$$\mu_0 \vec{J} = \nabla \times \vec{B}, \tag{1.15}$$
$$\vec{E} = \varrho \vec{J} - \vec{v} \times \vec{B}, \tag{1.16}$$
$$\frac{\partial e}{\partial t} = -\nabla \cdot (e\vec{v}) - P_{\text{ther}} \nabla \cdot \vec{v} + q, \tag{1.17}$$

which are often called the magneto-hydrodynamics (MHD) equations. Here, (1.12), (1.13) and (1.17) are the equations of mass, momentum and energy conservation, respectively. Eq. (1.14) is the magnetic field induction equation, Eq. (1.15) is the Ampère's circuital law, and Eq. (1.16) is the Ohm's law. The symbol $\vec{v}$ denotes the velocity vector, $\mathbf{T}$ is the viscous stress tensor, P_{ther} is thermal (gas plus radiation) pressure, e is the internal energy and q represents cooling rate including the effects of radiative cooling, viscous dissipation and Joule dissipation in general. The vector $\vec{B}$ is magnetic flux density which is divergenceless ($\nabla \cdot \vec{B} = 0$), $\vec{E}$ is electric field vector, $\vec{J}$ is the electric current density vector and ϱ is electric resistivity. Note that in the non-relativistic scenario where the fluid sound speed is far less than the speed of light, the displacement current term $\partial \vec{E}/\partial t$ can be ignored so that the general Ampère-Maxwell law can be simplfied into Eq. (1.15).

The effect of radiative transfer, which is particularly important in stellar surface convection simulations, is embedded in the cooling term q. The radiative cooling rate at a given spacial location is computed via

$$q_{\text{rad}} = \int_{\Omega} \int_0^{\infty} \chi_\lambda (I_\lambda - S_\lambda) \, d\lambda d\Omega, \tag{1.18}$$

where Ω and λ denote solid angle and wavelength, respectively. The terms χ_λ, I_λ and S_λ are the monochromatic extinction coefficient, intensity and source function, respectively. In particular, the monochromatic intensity is obtained by solving the radiative transfer equation

$$\frac{dI_\lambda}{d\tau_\lambda} = I_\lambda - S_\lambda. \tag{1.19}$$

There are multiple codes that solve the equation system (1.12)-(1.19) in 3D in the astrophysical context. In the modelling of stellar surface convection, the widely used codes include Stagger (Nordlund & Galsgaard, 1995; Kritsuk et al., 2011), MURaM (Vögler et al., 2005), antares (Muthsam et al., 2010) and co^{5}bold (Freytag et al., 2012). In this thesis, I use a customized version of the Stagger code (Collet et al., 2018), which solves Eqs. (1.12)-(1.19) on 3D staggered Eulerian mesh (see Fig. 1.3). The stellar models present in the thesis have been constructed without magnetic fields (i.e. $\vec{B} = \vec{E} = 0$). As shown in Fig. 1.3, all scalars are evaluated at cell centres, whereas vectors, such as velocity, are staggered at the centres of cell faces in order to improve numerical accuracy. The code incorporates realistic microphysics and a detailed radiative transfer scheme. An updated version of the Mihalas et al. (1988) equation of state (Trampedach et al., 2013) is adopted, which accounts for all ionization stages of the 17 most abundant elements in the Sun plus the H_2 molecule. A comprehensive collection of relevant continuous absorption and scattering sources is included as described in Hayek et al. (2010). The pre-computed, sampled line opacities are taken from the MARCS model atmosphere package. Radiative energy transport is modelled by solving the equation of radiative transfer (1.19) at every time step of the simulation for all mesh points above a certain Rosseland mean optical depth, under the assumption of local thermodynamic equilibrium (LTE). The wavelength dependence of the radiative transfer equation is approximated via the opacity binning method (Nordlund, 1982; Collet et al., 2018), in which 12 opacity bins are divided based on wavelength and strength of opacities. Consequently, the integration over wavelength reduces to the summation over 12 selected bins. The spatial dependence of the radiative transfer equation is represented by solving along a set of inclined rays in space. Nine directions – one vertical and eight inclined directions representing combinations of two polar and four azimuthal angles – are considered for all models presented in this thesis. The integration over polar angle is carried out using the Gauss-Radau quadrature scheme. The resulting radiative cooling rates enter into Eq. (1.17) and can be used to calculate the surface flux (i.e., the emergent radiative disk centre intensity at the top boundary of simulation domain), which is depicted in the left panel of Fig. 1.4 for the 3D solar simulation. The emergent flux predicted from the radiative transfer calculation is nearly indistinguishable from observations.

The STAGGER model stellar atmosphere adopted in this thesis simulates a small part of the star near the photosphere. The vertical extent of the simulation domain covers roughly the outer 1% of the stellar radius, extending from the upper part of the surface convection zone, including the entire optical surface, and reaching the lower part of the chromosphere. The size of the horizontal direction has the same order of magnitude as the vertical. The horizontal boundaries are periodic, meaning that fluid elements that going out via one horizontal boundary will come back from the opposite one. Boundaries in the vertical direction are open. The default bottom boundary condition is that outgoing flows (vertical velocities towards stellar centre) are free to carry their entropy fluctuations out of the simulation domain, whereas incoming flows (vertical velocities towards stellar surface) must have invariant entropy and thermal (gas plus radiation) pressure. The simulation domain is small but nevertheless representative, because it resides in the region where 3D effects, such as fluctuations in the horizontal plane caused by the up and down flows of fluid and the presence of strong turbulence, are most prominent. Also worth noting is that the spherical effect in our model is negligible because the vertical scale is small compared to the total stellar radius. Such a simulation set-up is often referred as the "box-in-a-star" simulation.

The "box-in-a-star" simulations of stellar surface convection have allowed for substantial contributions to many aspects of stellar physics. The early simulations of, for example, Nordlund (1985) and Stein & Nordlund (1989) revealed that surface convection operates in a way that is fundamentally different from what described by the MLT. At the photosphere, fluid becomes entropy-deficient through radiative cooling; this results in negative buoyancy, leading to streams of gas descending through the optical surface in thin convective sheets. Conservation of mass forces the surrounding, relatively entropy-rich material to rise back up through the thin optical surface, forming so-called granules. Detailed 3D solar simulations presented in Stein & Nordlund (1998) further confirm this picture, and their work demonstrated excellent agreement between simulation and observation in the granulation pattern and power spectrum. Moreover, magnetic phenomena such as sunspots can also be realistically modelled via magneto-hydrodynamic simulations of the solar surface (see Rempel et al. 2009). These *ab initio* simulations have enable the prediction of various observables in a parameter-free manner. For example, spectral line formation calculations based on 3D models agree remarkably well with corresponding observations without relying on adjustable parameters such as micro- and macro-turbulence (Asplund et al., 2000). This has important effects on the determination of the solar elemental abundance (Asplund et al., 2009). Meanwhile, 3D models can be used to improve stellar structure and evolution calculations, such as calibrating the mixing length parameter (Ludwig et al., 1999; Trampedach et al., 2014b; Magic et al., 2015), or serving as outer boundary condition for stellar evolution simulations (Mosumgaard et al., 2018; Jørgensen et al., 2018).

Previous investigations also demonstrated that 3D simulation of stellar surface convection can be used to address asteroseismology problems. Rosenthal et al. (1999) showed that the discrepancy between theoretical and measured solar p-mode frequencies, i.e. the surface effect, can be reduced by combining the averaged 3D model with 1D interior model then computing the theoretical oscillation frequency based on the patched model (see also Sonoi et al. 2015; Ball et al. 2016; Trampedach et al. 2017; Jørgensen et al. 2017; Houdek et al. 2017). The reason for the better agreement is that the averaged 3D model has more realistic stratification near the photosphere. As 3D simulations are able to describe convective turbulence from first principles, they turn out to be a promising approach to study how solar-like oscillations are excited and damped in the near-surface convection zone. A notable breakthrough in this direction has already been made by Nordlund & Stein (2001) and Stein & Nordlund (2001). In their pioneering work, the excitation rates of solar radial modes are extracted directly from 3D solar surface convection simulations.

In this thesis, I expand on their idea and further explore the possibility of modelling both mode excitation and damping using 3D simulations. I investigate also the relationship between solar-like oscillations measured via photometry and spectroscopic in detail using 3D models.

1.3 Thesis Outline

The studies presented in this thesis have contributed to the understanding of how solar-like oscillations are excited and damped in the surface convection zone. The quantitative relation between solar-like oscillations measured by photometry and spectroscopy is also analysed in detail.

In Chapter 2, I recall the necessary mathematical framework to extract the p-mode excitation rates from our 3D stellar models coupled to full 1D stellar interior and evolution models. The damping rates as a function of frequency are also predicted from 3D simulations using a novel numerical technique. Knowledge of how modes are driven and dissipated enables the estimation of their amplitude, from which a theoretical $\nu_{\rm max}$ value can be deduced. I focus on the solar case in Chapter 2 and compare my theoretical results with corresponding helioseismic observations.

In Chapter 3, I apply the theoretical framework and numerical technique introduced in Chapter 2 to several key benchmark turn-off and subgiant stars. Studying several stars enables the investigation of the relationship between mode excitation/-damping and fundamental stellar parameters. In Chapter 3, I also describe in detail how the 1D interior models are obtained from stellar evolution simulations. My numerical technique for evaluating mode damping rates from 3D simulations is also validated in Chapter 3.

In Chapter 4, I carry out 3D simulations of stellar stellar atmosphere and perform realistic spectral line formation calculations to quantify the ratio between luminosity and radial velocity amplitude for the Sun and a benchmark red giant star. Luminosity amplitudes are computed from the bolometric flux predicted by 3D simulations, with granulation background modelled the same way as asteroseismic observations. Radial velocity amplitudes are determined from the Doppler shift of synthetic spectral lines measured with methods that closely resembling those used by ground-based telescopes. The resulting amplitude ratios are directly comparable to the corresponding observations. I conclude this thesis with final remarks and future prospects in Chapter 5.

Chapter 2

The amplitude of solar p-mode oscillations from three-dimensional convection simulations

Yixiao Zhou, Martin Asplund and Remo Collet, *The Amplitude of Solar p-mode Oscillations from Three-dimensional Convection Simulations*, 2019, The Astrophysical Journal, 880:13.

Abstract

The amplitude of solar p-mode oscillations is governed by stochastic excitation and mode damping, both of which take place in the surface convection zone. However, the time-dependent, turbulent nature of convection makes it difficult to self-consistently study excitation and damping processes through the use of traditional one-dimensional hydrostatic models. To this end, we carried out *ab initio* three-dimensional, hydrodynamical numerical simulations of the solar atmosphere to investigate how p-modes are driven and dissipated in the Sun. The description of surface convection in the simulations is free from the tuneable parameters typically adopted in traditional one-dimensional models. Mode excitation and damping rates are computed based on analytical expressions whose ingredients are evaluated directly from the three-dimensional model. With excitation and damping rates both available, we estimate the theoretical oscillation amplitude and frequency of maximum power, $\nu_{\max}$, for the Sun. We compare our numerical results with helioseismic observations, finding encouraging agreement between the two. The numerical method presented here provides a novel way to investigate the physical processes responsible for mode driving and damping, and should be valid for all solar-type oscillating stars.

2.1 Introduction

Asteroseismology, the study of stellar oscillations, opens a unique window to probe various properties of stars. The analysis of the power spectra of stellar oscillations makes allows to infer the structure of stellar interiors as well as the fundamental parameters of stars (Basu et al., 2009; Kjeldsen & Bedding, 1995). In some cases, it is possible to determine the evolutionary stages (Mosser et al., 2012a), size of surface/core convection zone (Basu & Antia, 1997; Deheuvels et al., 2016), or rotation rates (Beck et al., 2012) of stars from their oscillation frequencies. Among many applications, the asteroseismic determination of fundamental stellar parameters such as masses and radii is of great significance not only to stellar physics but to astronomy in general. For instance, stellar radii are used to derive exoplanet radii from the analysis of exoplanet transit light curves. Stellar masses can be related to stellar ages, which play a fundamental role in Galactic archaeology.

Over the past decade, oscillations in thousands of solar-type stars have been detected by the CoRoT (Michel et al., 2008) and *Kepler* (Borucki et al., 2010) satellites, their number being destined to grow thanks to the current TESS (Ricker et al., 2015) mission. These space-borne telescopes have paved the way to a new epoch of ensemble asteroseismology. In this context, the asteroseismic determination of stellar parameters from special empirical seismic scaling relations (Brown et al., 1991; Kjeldsen & Bedding, 1995) has proven to be very effective. The seismic scaling relations link key seismic observables –large frequency separation $\Delta\nu$ and frequency of maximum oscillation power $\nu_{\max}$– to stellar mass, radius and effective temperature, relatively to the Sun.

The widespread application of the seismic scaling relations to stellar parameter determinations calls for a deeper investigation of the underlying physical processes behind the emergence of $\Delta\nu$ and $\nu_{\max}$. On the one hand, $\Delta\nu$, a comparatively well understood quantity, is a proxy for the mean density of star (Ulrich, 1986). On the other hand, $\nu_{\max}$, which is determined from oscillation amplitudes, has a tight connection with the driving and damping mechanisms of oscillations but its exact origin is still poorly understood. Although noticeable progress has been made towards the theoretical understanding of $\nu_{\max}$ (Belkacem et al., 2011), a complete solution to this issue still requires a thorough explanation of how modes are excited and damped in solar-type oscillators.

Previous investigations have provided insights to the physics of both mode excitation and damping. Goldreich & Keeley (1977b) first proposed that oscillations in the Sun are driven by turbulent convection. From this promise, Goldreich et al. (1994) and Samadi & Goupil (2001) developed theoretical formulations to model the stochastic excitation of oscillations by stellar surface convective motions, assuming a one-dimensional (1D) description of convection based on the mixing-length theory. Based on these theoretical prescriptions, Goldreich et al. (1994) and Belkacem et al. (2010) computed numerically the excitation rates for the Sun, finding a satisfactory match to observationally inferred values. In addition, Samadi et al. (2008) showed that the same theoretical framework for mode excitation is also applicable to other solar-like oscillators such as α Centauri A. On the other side, it is natural to analyse the stability of these stochastically-driven modes, and, if stable, the rate of their energy dissipation. The first question was examined in detail by Balmforth (1992a) and the conclusion was that all solar p-modes are stable. The second question was answered by Houdek et al. (1999) and Chaplin et al. (2005), who computed damping rates for solar p-modes using a non-local mixing-length model, finding good agreement with observed line widths (see Houdek & Dupret 2015 for a review of the model).

There is no doubt that the aforementioned studies have greatly enriched our understanding toward the nature of p-mode oscillations in solar-type stars. However, due to the lack of highly realistic analytical description of convection and turbulence, theoretical models adopted in these works are unavoidably simplified to some extent. In particular, the dynamic and chaotic nature of turbulence is embedded in free parameters that have to be calibrated either from other theoretical models or from observational data. A promising approach to overcome this difficulty is to simulate excitation and damping of modes from first principle using three-dimensional (3D) hydrodynamical numerical simulations. Noticeable breakthrough in this direction has already been made by Nordlund & Stein (2001) and Stein & Nordlund (2001). In their pioneering work, the excitation rates of solar radial modes are extracted directly from 3D simulation of near-surface layers of the solar convective region. Their results involve no free parameters and fall in line with observation. In this paper, we expand their idea and further explore the possibility of modelling both mode excitation (Sect. 2.3) and damping (Sect. 2.4) using 3D simulation. Knowledge of how modes are driven and dissipated enables us to estimate their amplitude, from which a theoretical $\nu_{\max}$ value can be deduced (Sect. 2.5). The results of these *ab initio* parameter-free numerical calculations are compared with helioseismic observations. As a first attempt on this topic, we focus on the Sun and limit our discussion to radial modes only.

2.2 Three dimensional solar atmosphere model

In this section, we briefly describe the 3D hydrodynamical model solar atmosphere used in this work. The model is computed with the Stagger code (Nordlund & Galsgaard, 1995; Collet et al., 2018), a state-of-the-art, radiative-magnetohydrodynamics code that solves the equations of mass, momentum, and energy conservation, and magnetic-field induction equation in 3D. Radiative energy transport is modelled by solving the 3D equation of radiative transfer at every time-step of the simulation along different inclined rays in space. For the present solar simulation, nine directions are used, including the vertical and eight inclined directions (a combination of two polar θ-angles and four azimuthal ϕ-angles). The code also adopts realistic micro-physics. It uses a modified version of the Mihalas et al. (1988) equation of state (Trampedach et al., 2013) that accounts for the 17 most abundant elements in the Sun as well as the H_2 and H_2^+ molecules (cf. Trampedach et al. 2013 Sect. 2.1). A com-

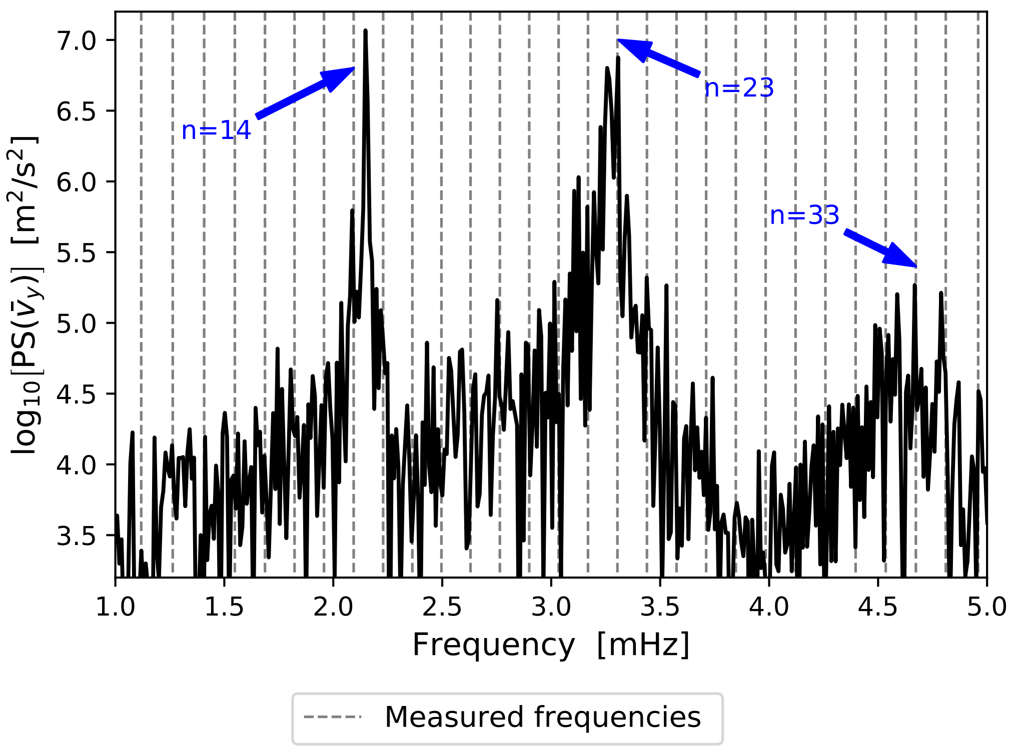

Figure 2.1: Vertical velocity power spectrum computed from 3D solar simulation, from which three simulation modes with cyclic frequency 2.148, 3.307 and 4.668 mHz are recognisable. Measured solar radial p-mode frequencies (degree $l = 0$, vertical grey dashed lines) are shown in the background with n denotes mode radial order. The observed frequency values are from Global Oscillations at Low Frequency (GOLF, GarcÍa et al. 2001; Gelly et al. 2002).

prehensive collection of relevant continuous absorption and scattering are included (Hayek et al., 2010). Line opacities are treated using opacity binning (Nordlund, 1982; Magic et al., 2013a), with 12 opacity bins divided in both wavelength and strength of opacity.

Our STAGGER model stellar atmosphere simulates a small part of the Sun near photosphere. It assumes a constant gravitational acceleration and ignores magnetic field. The simulation domain covers 6 Mm × 6 Mm area horizontally, and 3.8 Mm in the vertical (radial) direction – approximately 1 Mm above the base of the photosphere and 2.8 Mm below it. The domain is discretized on a 3D Cartesian grid, with spatial resolution 240^3, which is sufficient for studying mode excitation[1]. Scalars, such as densities and internal energies, are evaluated at cell center while vectors, such as momentum densities, are staggered at cell faces (hence the meaning of "Stagger"). The simulation domain is small but nevertheless representative, because it resides in the region where 3D effects, such as fluctuations in horizontal plane caused by up and down flow of fluid and the presence of strong turbulence, are most prominent. We note also that spherical effect in our model is negligible because the vertical scale is small compared to the total radius of the Sun. Temporally, our model spans 24 hours solar time, with one snapshot stored every 30 seconds. This sampling interval is adequately short, since doubling it will not influence our excitation and damping results (see in Sect. 2.3 and 2.4) significantly.

Global parameters of our solar model are very close to actual solar values. The mean effective temperature over 24 hours solar time is 5772.7 K, almost the same as the nominal solar value (5772.0 K, Prša et al. 2016); gravitational acceleration is set to 2.74×10^4 g/cm^2, taken from Prša et al. (2016); for element abundances we adopt the Asplund et al. (2009) solar composition.

P-mode oscillations are natural phenomena in our model. Radial p-modes can be identified by looking at the power spectrum of horizontally averaged vertical velocity:

$$\mathrm{PS}[\bar{v}_y](\omega) = \frac{1}{N}\left|\sum_{s=0}^{N-1} \bar{v}_y(t_s)e^{i\omega s\Delta\tau}\right|^2. \tag{2.1}$$

Here $\bar{v}_y$ is the horizontally averaged vertical velocity of snapshot s, ω is angular frequency, $\Delta\tau$ being the time interval between two consecutive snapshots, N the total snapshot number ($N = 2880$ in our case). The power spectrum of $\bar{v}_y$ around photosphere is shown in Fig. 2.1, the peaks represent radial p-mode naturally emerged in the simulation box. In total three simulation modes with frequency 2.148, 3.307, 4.668 mHz are identifiable from Fig. 2.1; no obvious oscillation signature is found below 1.5 mHz or above 5 mHz. Two of them have frequencies that are close to the p-mode frequencies measured in the Sun. The simulation mode with lowest frequency deviates from the observed quantity. This reflects the finite extent of the 3D simulation, since lower frequency modes have greater amplitudes at depth than higher frequency

[1]As discussed in Samadi et al. (2007), the differences between excitation rates computed based on 253 × 253 × 163 and 125 × 125 × 82 solar simulations are small, implying our adopted spatial resolution is sufficient for this problem.

ones as seen in Fig. 2.4. Had the 3D model extended to deeper interior of the Sun, the expectation is that this discrepancy would be reduced.

Although the property of simulation modes are affected by the finite spatial dimension of the simulation box[2] (hence also called "box modes"), we clarify that "box modes" are natural phenomena in 3D simulation rather than numerical noise. We further clarify the peaks in Fig. 2.1 represent radial modes rather than the radial component of low-degree non-radial modes, although their oscillation frequencies can be close to each other. The degree l of a mode indicates the number of its surface nodes (fixed point from the north pole, along the surface of the sphere, to south pole). The horizontal wavelength λ_h and the degree of a mode are related by:

$$\frac{\lambda_h}{2} \simeq \frac{\pi \mathcal{R}}{l}, \tag{2.2}$$

where $\mathcal{R}$ is the stellar radius. In order to resolve a non-radial mode in the simulation, the horizontal wavelength of this mode should be shorter than the horizontal domain of the simulation. Therefore, in our case, non-radial oscillations can be identified only if its horizontal wavelength $\lambda_h \lesssim 6$ Mm, which corresponds to $l \gtrsim 729$. In other words, non-radial low-degree (i.e. $l = 1, 2, 3$ ...) p-modes cannot be detected because of the limited simulation domain.

Stein & Nordlund (1998) have demonstrated that the granulation pattern from 3D simulation of solar atmosphere strongly resembles what observed on the Sun, after considering telescope and atmosphere seeing. The distribution of granule size from simulations is in agreement with solar observation as well (Stein & Nordlund, 1998). Asplund et al. (2000) and Pereira et al. (2013) also reported excellent match when comparing the detailed spectral lines predicted from 3D solar simulation with observation.

These facts lead us to believe that such 3D solar atmosphere model is a highly realistic representation of the physical processes taking place near the solar surface region. Our 3D Stagger solar model will be applied to the subsequent calculation of excitation rates.

2.3 Excitation rates

In the Sun, the observed p-mode oscillations are driven by near-surface convection. The driving process is quantified by (mode) excitation rate which describes how fast energy is supplied from stochastic convection to coherent fluid motion. In this section, we will specify how to extract excitation rates from 3D stellar atmosphere model (Sect. 2.3.1, 2.3.2), and present numerical results for the Sun (Sect. 2.3.3). Here we confine the discussion to radial oscillations.

[2]The property of simulation modes, as well as $\bar{v}_y$, will not enter into the subsequent computation of excitation rates, because the main effect of p-mode oscillations in the simulation is filtered out by mapping physical quantities into pseudo-Lagrangian frame (cf. Sect. 2.3.2).

2.3.1 Theoretical formulation

The expression of excitation rate for radial modes was originally derived in pioneering works by Goldreich et al. (1994), Samadi & Goupil (2001) and Nordlund & Stein (2001, abbreviated NS01 hereinafter). We follow the formulation developed in NS01, since it is more suitable for direct numerical evaluation. NS01 started with basic fluid equations in 3D, rewrote them to horizontal-averaged perturbed fluid equations. From the (1D) perturbed equations they obtained the expression of work integral (defined below) with proper approximation, then arrived at the change in mode kinetic energy per unit area over certain time interval Δt (i.e., excitation rate per unit area, NS01 Eqs. 65, 66 and 71)

$$\frac{\Delta \langle E_\omega \rangle_{\mathrm{ens}}}{\Delta t} = \frac{1}{4\Delta t} \left\langle \left| \int_{\Delta t} \int_r \delta \bar{P}_{\mathrm{nad}}(r,t) \frac{1}{E_0^{1/2}} \frac{\partial(\dot{\delta r})}{\partial r} dr\, dt \right|^2 \right\rangle_{\mathrm{ens}}, \tag{2.3}$$

with E_0 the mode kinetic energy per unit surface area (NS01 Eq. 63):

$$E_0 = \frac{\omega^2}{2} \int_r \rho \xi_r^2(r) \left(\frac{r}{R_{\mathrm{phot}}} \right)^2 dr. \tag{2.4}$$

The integral over radius r in Eq. (2.3) is the so-called "work integral", ρ is density, R_{phot} is photosphere radius, and $\delta \bar{P}_{\mathrm{nad}}$ is the horizontally averaged non-adiabatic pressure fluctuation that arises from non-adiabatic effects including entropy fluctuation and convective turbulence. The $\langle ... \rangle_{\mathrm{ens}}$ bracket stands for the ensemble average over all phases (NS01 Sect. 3.2), it is necessary because the phase differences between coherent waves and chaotic convective processes are completely random. The canonical form of mode displacement vector $\delta\vec{r}$ is written as (we refer the readers to Aerts et al. 2010 Sect. 3.3.1 for a thorough introduction)

$$\begin{aligned} \delta\vec{r} = \mathfrak{Re}\, \{ [& \xi_r(r) Y_{lm}(\theta,\phi)\vec{e}_r + \\ & \xi_h(r) \left(\partial_\theta Y_{lm}(\theta,\phi)\vec{e}_\theta + \frac{1}{\sin\theta} \partial_\phi Y_{lm}(\theta,\phi)\vec{e}_\phi \right)] \, e^{-i(\omega t + \varphi)} \Big\}, \end{aligned} \tag{2.5}$$

where ξ_r and ξ_h are the amplitude functions (also named mode eigenfunctions from numerical point of view), and $Y_{lm}(\theta,\phi)$ are the spherical harmonic functions with l, m being the angular quantum numbers[3]. Note that φ is an arbitrary phase factor, however, in our context, it is the phase difference between non-adiabatic pressure fluctuation and oscillation mode. As we are considering radial modes only, Eq. (2.5) simplifies into

$$\delta r = \mathfrak{Re} \left\{ \xi_r(r) e^{-i(\omega t + \varphi)} \right\}. \tag{2.6}$$

In Eq. (2.3), the coupling between $\delta \bar{P}_{\mathrm{nad}}$ and δr reflects the interaction between convection and pulsation which is responsible for mode excitation. Substituting Eq. (2.6)

[3] $\mathfrak{Re}\{f\}$ ($\mathfrak{Im}\{f\}$) means the real (imagery) part of complex function f.

into Eq. (2.3),

$$\begin{aligned}\frac{\Delta\langle E_\omega\rangle_{\rm ens}}{\Delta t} &= \frac{1}{4\Delta t}\left\langle\left|\mathfrak{Re}\left\{\int_r(-i\omega)e^{-i\varphi}\frac{1}{E_0^{1/2}}\frac{\partial\xi_r}{\partial r}\right.\right.\right.\\ &\left.\left.\left.\int_{\Delta t}\delta\bar{P}_{\rm nad}(r,t)e^{-i\omega t}\,dt\,dr\right\}\right|^2\right\rangle_{\rm ens}.\end{aligned} \tag{2.7}$$

The time integral in Eq. (2.7) is equivalent to the Fourier transform of non-adiabatic pressure fluctuation. Expanding Eq. (2.7) gives

$$\begin{aligned}&\frac{\Delta\langle E_\omega\rangle_{\rm ens}}{\Delta t} =\\ &\frac{\omega^2}{4\Delta t}\left\langle\sin^2\varphi\left(\int_r\frac{1}{E_0^{1/2}}\frac{\partial\xi_r}{\partial r}\mathfrak{Re}\left\{\mathcal{F}[\delta\bar{P}_{\rm nad}]\right\}\,dr\right)^2\right\rangle_{\rm ens}\\ &-\frac{\omega^2}{4\Delta t}\left\langle 2\sin\varphi\cos\varphi\left(\int_r\frac{1}{E_0^{1/2}}\frac{\partial\xi_r}{\partial r}\mathfrak{Re}\left\{\mathcal{F}[\delta\bar{P}_{\rm nad}]\right\}\,dr\right)\right.\\ &\left.\left(\int_r\frac{1}{E_0^{1/2}}\frac{\partial\xi_r}{\partial r}\mathfrak{Im}\left\{\mathcal{F}[\delta\bar{P}_{\rm nad}]\right\}\,dr\right)\right\rangle_{\rm ens}\\ &+\frac{\omega^2}{4\Delta t}\left\langle\cos^2\varphi\left(\int_r\frac{1}{E_0^{1/2}}\frac{\partial\xi_r}{\partial r}\mathfrak{Im}\left\{\mathcal{F}[\delta\bar{P}_{\rm nad}]\right\}\,dr\right)^2\right\rangle_{\rm ens}.\end{aligned} \tag{2.8}$$

The ensemble average over all phases is calculated as

$$\langle f\rangle_{\rm ens} = \frac{1}{2\pi}\int_0^{2\pi} f(\varphi)\,d\varphi. \tag{2.9}$$

Therefore, $\langle\sin^2\varphi\rangle_{\rm ens} = 1/2$, $\langle\cos^2\varphi\rangle_{\rm ens} = 1/2$, $\langle 2\sin\varphi\cos\varphi\rangle_{\rm ens} = 0$ and Eq. (2.8) simplifies into

$$\begin{aligned}\frac{\Delta\langle E_\omega\rangle_{\rm ens}}{\Delta t} =&\frac{\omega^2}{8\Delta t}\left[\left(\int_r\frac{1}{E_0^{1/2}}\frac{\partial\xi_r}{\partial r}\mathfrak{Re}\left\{\mathcal{F}[\delta\bar{P}_{\rm nad}]\right\}\,dr\right)^2\right.\\ &\left.+\left(\int_r\frac{1}{E_0^{1/2}}\frac{\partial\xi_r}{\partial r}\mathfrak{Im}\left\{\mathcal{F}[\delta\bar{P}_{\rm nad}]\right\}\,dr\right)^2\right],\end{aligned} \tag{2.10}$$

where $\mathcal{F}$ represents Fourier transform from time to frequency domain. Eq. (2.10) is essentially equivalent to Eq. 5 in Stein & Nordlund (2001, SN01), we will use (2.10) to calculate excitation rates.

2.3.2 Numerical evaluation

Two key ingredients in Eq. (2.10) are non-adiabatic pressure fluctuation $\delta\bar{P}_{\rm nad}$ and amplitude function ξ_r, representing the dynamics of convection and oscillation re-

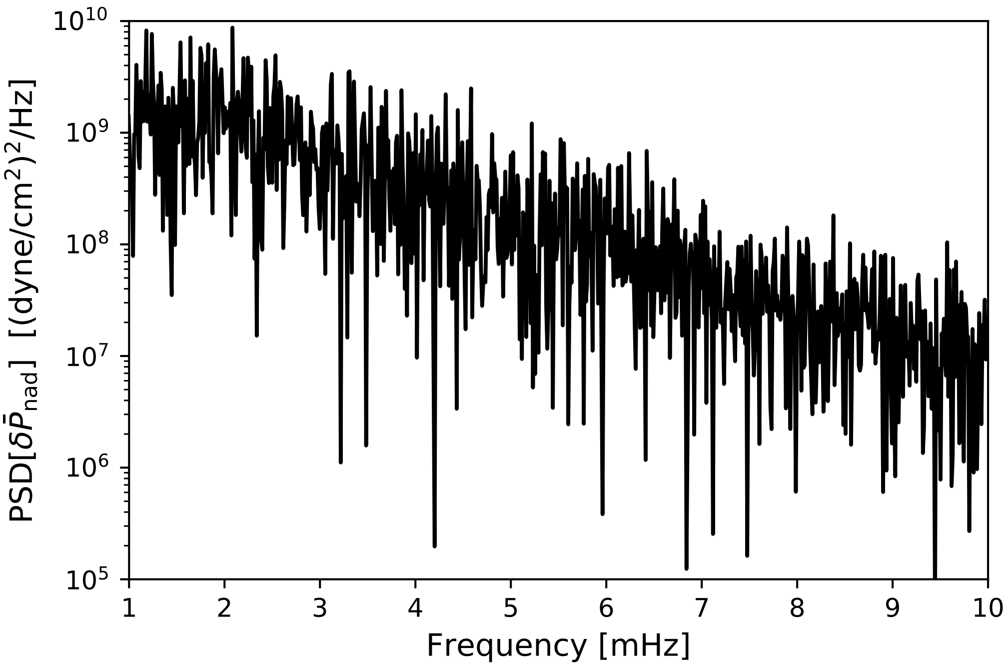

Figure 2.2: $\delta\bar{P}_{\rm nad}$ power spectrum density at 100 km below photosphere, as computed via Eq. (2.14).

spectively. In this subsection, we explain how they are computed numerically.

The time-dependent nature of 3D model allows the direct evaluation of $\delta\bar{P}_{\rm nad}$, which is the difference between total and adiabatic pressure fluctuation (SN01 Eq. 3),

$$\delta\bar{P}_{\rm nad} = \delta\bar{P} - \delta\bar{P}_{\rm ad} = (\delta\ln\bar{P} - \bar{\Gamma}_1\delta\ln\bar{\rho})\bar{P}, \tag{2.11}$$

where δ stands for Lagrangian perturbation. P and Γ_1 are total pressure and first adiabatic index respectively. As before, the bar symbol denotes horizontal averaging. In 3D hydrodynamical stellar atmosphere simulations, the change of physical quantities around their mean value consists of mainly two contributions: (a) perturbations from radiative and convective processes (b) collective fluid motions in the simulation domain (i.e. p-mode oscillations). Because (b) is approximately adiabatic, it is important to isolate (a) from (b) in order to calculate $\delta\bar{P}_{\rm nad}$. This is achieved by mapping variables from the original Cartesian frame to a frame that is co-moving with collective fluid motion. The latter is often named pseudo-Lagrangian frame, which is characterized by horizontal- and time-averaged column mass density at each geometric depth,

$$\sigma(y) = \left\langle \int_{y_{\rm top}}^{y} \bar{\rho}(y', t_s)\, dy' \right\rangle_t , \tag{2.12}$$

which filters out the main effect of radial p-modes (Rosenthal et al., 1999; Trampedach et al., 2014b). Here, $\langle ... \rangle_t$ means time average (that is, average over all snapshots), $y_{\rm top}$ is the geometric depth at the top of simulation domain, and the s index refers

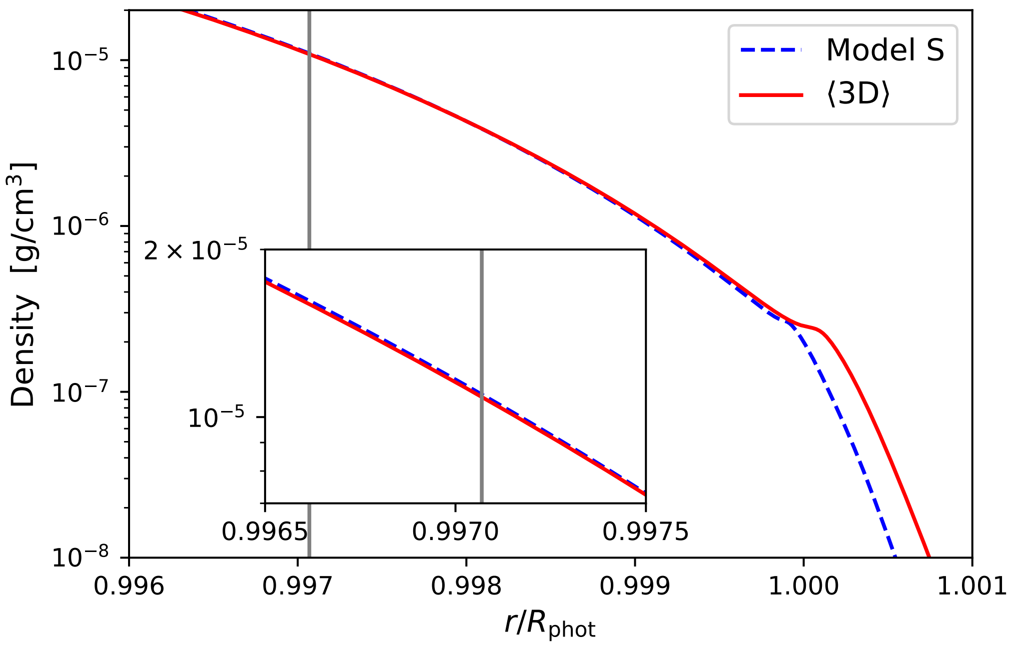

Figure 2.3: The predicted density profile in near-surface region of solar models as a function of fractional radius (normalized by radius at photosphere), with a zoom-in near matching point. Blue dashed and red solid lines represent model S and horizontal- and time-averaged 3D model respectively. Grey vertical line marks the location of interior matching point.

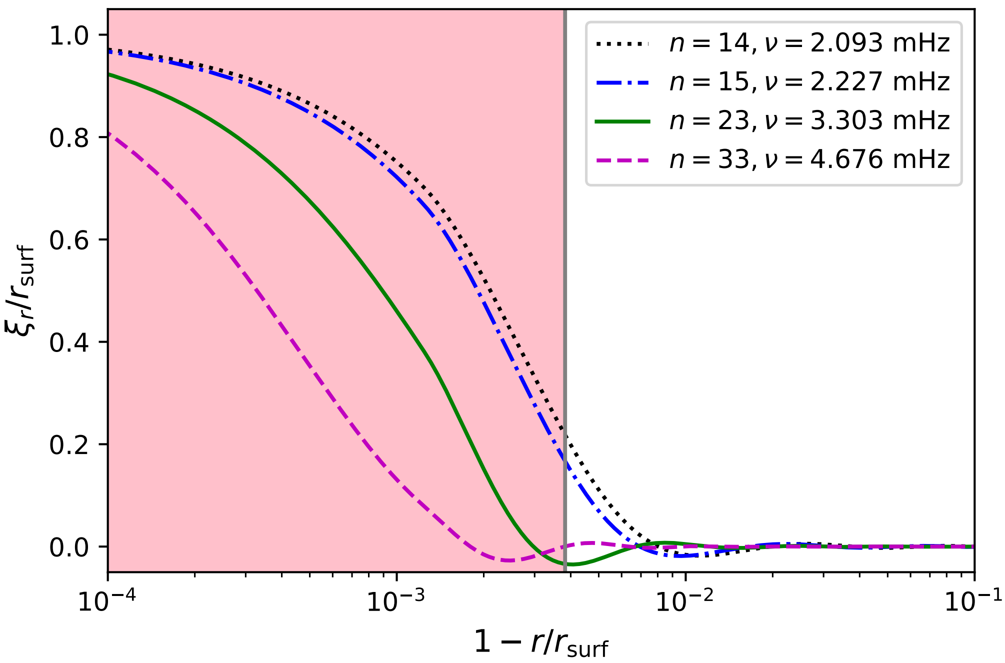

Figure 2.4: Normalized eigenfunctions for four radial modes computed from ADIPLS with the patched solar model. Here $r_{\rm surf}$ is the radius of the upper-most (surface) point of the patched model. Theoretical frequencies and radial orders of these example modes are also shown. Pink-shaded zone is the part covered by the 3D simulation. Note that the magnitude of eigenfunction in solar interior, relative to its surface value, decreases with increasing frequency.

to the snapshot number. In pseudo-Lagrangian frame, the Lagrangian perturbation changes into Eulerian perturbation[4], hence Eq. (2.11) can be simplified into

$$\begin{aligned}\delta\bar{P}_{\mathrm{nad}}(t) = [&(\ln\bar{P}_{\mathrm{L}}(t) - \ln\bar{P}_{0,\mathrm{L}}) \\ &- \bar{\Gamma}_{1,\mathrm{L}}\,(\ln\bar{\rho}_{\mathrm{L}}(t) - \ln\bar{\rho}_{0,\mathrm{L}})]\,\bar{P}_{\mathrm{L}}.\end{aligned} \tag{2.13}$$

Here quantities defined in pseudo-Lagrangian frame are marked with subscript "L", while the subscript "0" stands for the equilibrium state. Numerically, the equilibrium state is calculated by taking the temporal average over all simulation snapshots.

Non-adiabatic pressure fluctuation is computed via (2.13), its power spectrum density,

$$\mathrm{PSD}[\delta\bar{P}_{\mathrm{nad}}](\omega) = \frac{\Delta\tau}{N}\left|\sum_{s=0}^{N-1}\delta\bar{P}_{\mathrm{nad}}(t_s)e^{i\omega s\Delta\tau}\right|^2, \tag{2.14}$$

is depicted in Fig. 2.2. No obvious peak is observed in the figure, which suggests non-adiabatic pressure fluctuation is associated with turbulent convection, with no preference over any specific frequency. This is in accordance with the conclusion in SN01.

We now turn to the other component of Eq. (2.10), ξ_r, a quantity that is solely relevant to oscillation. In the case of radial mode, ξ_r describes mode amplitude distribution in the star. Contrary to $\delta\bar{P}_{\mathrm{nad}}$, we choose to compute ξ_r with patched 1D model rather than extract it from simulation. The reason is that, first of all, only three modes are clearly identifiable in 3D model, much less than the number of radial modes detected for the Sun. Secondly, although the oscillation amplitude of radial modes are largest in the near-surface region covered by the simulation, they actually propagate throughout the entire star. The patched 1D model is obtained by combining 1D interior model with horizontal- and time-averaged 3D model. Therefore, it extends from stellar center to the upper boundary of 3D model. Another advantage of patched model is that it reduces the "surface effect"[5], thereby bringing theoretical p-mode frequencies closer to measured values.

In this work, we adopt the standard solar model (also called model S, Christensen-Dalsgaard et al. 1996) as the 1D interior model. Model S is widely used as a reference model for helioseismic analysis. The model-predicted sound speed and density profile are both in good agreement with corresponding heliosismic-inferred values (cf. Basu et al. 1997 Figs. 6 and 10).

To combine horizontal- and time-averaged 3D atmosphere model with model S,

[4]Detailed explanations to Eulerian and Lagrangian perturbations is available in, e.g., Aerts et al. (2010) Chapter 3.

[5]The "surface effect" refers to the mismatch between observed and predicted p-mode oscillation frequencies at high frequencies in the Sun and other solar-type stars, which is due to the inadequate description of the outer stellar convection zone and atmospheric structure by traditional 1D models as well as the adiabatic assumption when computing theoretical mode frequencies. For efforts on this topic, consult, e.g., Rosenthal et al. (1999), Trampedach et al. (2017), Jørgensen et al. (2017) and Houdek et al. (2017).

we first select a matching point in atmosphere model which is located slightly above the bottom of simulation domain (although not exactly *at* the bottom layer, so to avoid artificial boundary effects) for the purposes of minimizing horizontal fluctuations in physical quantities. The matching point in model S is then determined by requiring the pressure to be identical to the average one at the matching point in the simulation, that is

$$\langle \bar{P}_{3D}(y_{am}) \rangle_t = P_{1D}(r_{im}), \tag{2.15}$$

where y_{am} is the geometric depth of matching point in 3D model ("am" stands for atmosphere matching point) and r_{im} is the radius of matching point in 1D model ("im" stands for interior matching point). The matching procedure ensures a continuous transition in pressure between averaged 3D and 1D model, and provides a unified depth scale (radius) between the two. We caution that due to 3D effects and different micro-physics between 3D and 1D model, there might be discontinuities for other quantities, for instance density, at the matching point. Nevertheless, the discontinuities are found to be small (Fig. 2.3) hence not likely to affect our results significantly. Finally, we trim the atmosphere and interior model by discarding all points below the atmosphere matching point in the averaged 3D model, and all points above the interior matching point in 1D model, then put them together to get the patched solar model.

We use the Aarhus adiabatic oscillation package (ADIPLS, Christensen-Dalsgaard 2008) to compute theoretical p-mode frequencies and eigenfunctions, as well as mode kinetic energy E_0, with patched solar model as input. Numerical results are depicted in Fig. 2.4 for four example p-modes. Our main focuses are high order ($n > 10$) radial ($l = 0$) p-modes with cyclic frequency below the acoustic cut-off frequency (~ 5 mHz for the Sun). Here we emphasize that eigenfunctions obtained from ADIPLS are normalized by their surface value, thus their absolute value has no physical meaning. To facilitate comparison between eigenfunctions, we eliminate the dependence on the normalization condition by dividing by their kinetic energy $\sqrt{E_0}$. As an example, the squared normalized eigenfunction gradients, $(\partial_r \xi_r)^2 / E_0$, of two example radial modes are demonstrated in Fig. 2.5, together with non-adiabatic pressure fluctuations at the same frequency.

2.3.3 Results

Now that two key quantities appearing in Eq. (2.10) have been computed, we proceed with the evaluation of the excitation rates. As $\delta \bar{P}_{nad}$ is accessible in practice only through the 3D simulation, the lower integration limit in Eq. (2.10) is the corresponding radius at the bottom of simulation domain, $r_{3D\,bot}$. On the other side, the work integral is terminated at the upper-most point r_{surf} of the patched model. Therefore

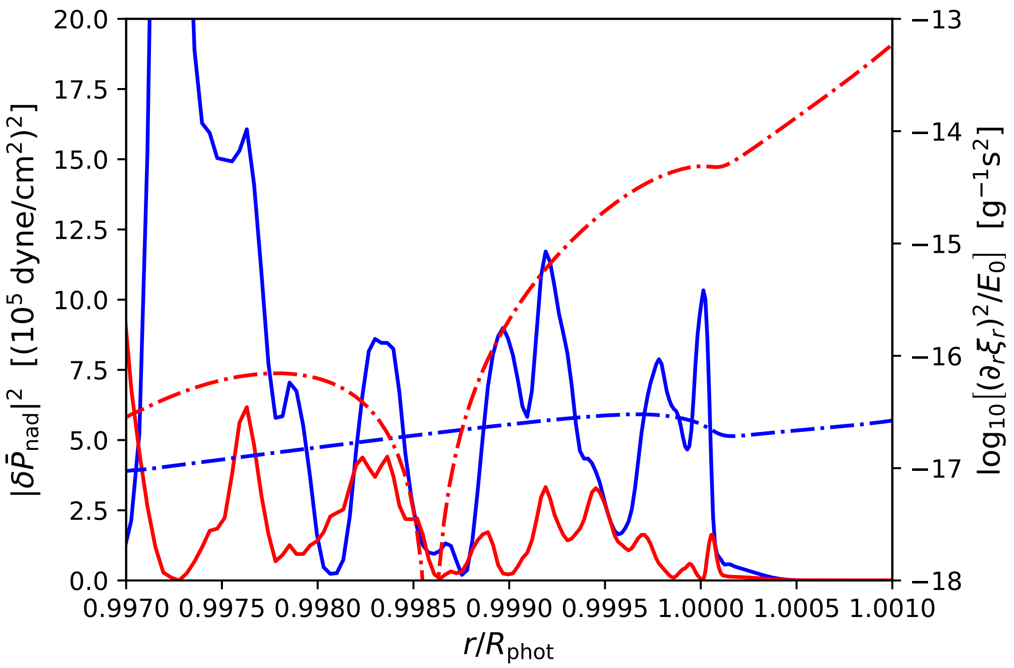

Figure 2.5: Normalized eigenfunction gradient (dash-dot lines) in the outer part of solar model, as well as non-adiabatic pressure fluctuation distribution (solid lines) at same frequency. Blue color represents $n = 11$, $\nu \approx 1.69$ mHz (lower frequency) radial mode while red corresponds to $n = 30$, $\nu \approx 4.26$ mHz (higher frequency) radial mode. Radial orders and mode frequencies are determined from ADIPLS.

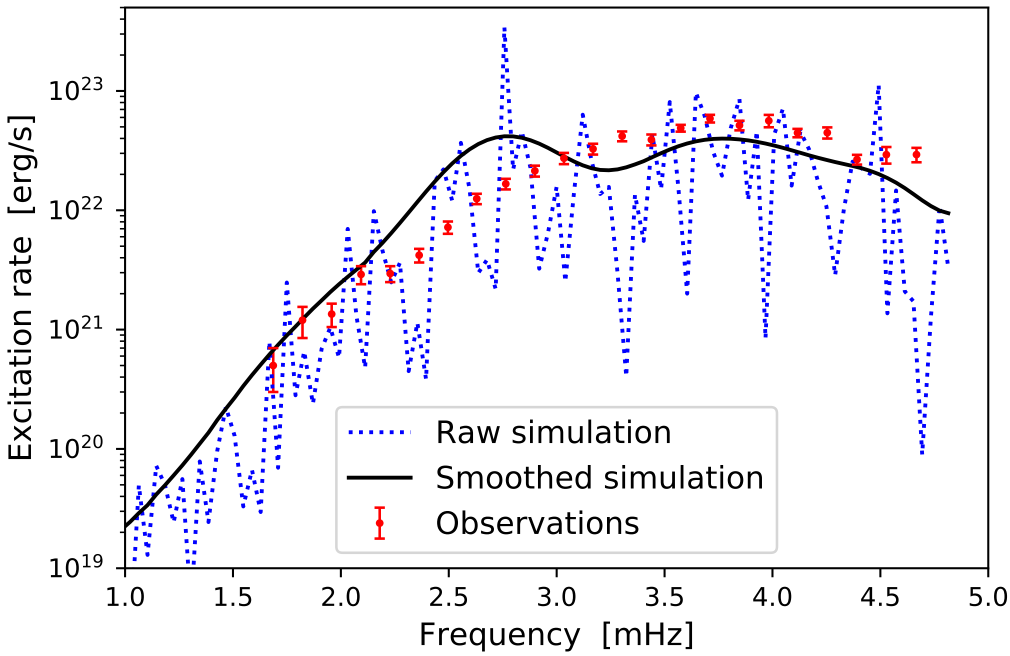

Figure 2.6: Excitation rates as a function of cyclic frequency computed from 3D solar atmosphere model and 1D patched solar model. Original data from simulation are shown in blue dotted line, and black solid curve is the result after smoothing with Gaussian kernel with full width at half maximum equals to 0.38 mHz. Excitation rates for $l = 0$ modes from Birmingham Solar-Oscillations Network (BiSON, Chaplin et al. 1998) are shown with red circles with uncertainties. The BiSON excitation rates have been divided by 2 in order to account for different definitions of mode energy (cf. Eq. (2.22) and Chaplin et al. 1998, Sect. 2.2).

Eq. (2.10) finally becomes

$$\begin{aligned}\frac{\Delta\langle E_\omega\rangle_{\text{ens}}}{\Delta t} =&\frac{\omega^2}{8\Delta t}\left[\left(\int_{r_{\text{3D bot}}}^{r_{\text{surf}}}\frac{1}{E_0^{1/2}}\frac{\partial\xi_r}{\partial r}\mathfrak{Re}\left\{\mathcal{F}[\delta\bar{P}_{\text{nad}}]\right\}\,dr\right)^2\right.\\&\left.+\left(\int_{r_{\text{3D bot}}}^{r_{\text{surf}}}\frac{1}{E_0^{1/2}}\frac{\partial\xi_r}{\partial r}\mathfrak{Im}\left\{\mathcal{F}[\delta\bar{P}_{\text{nad}}]\right\}\,dr\right)^2\right],\end{aligned} \tag{2.16}$$

with kinetic energy integrated from stellar center to surface

$$E_0 = \frac{\omega^2}{2}\int_0^{r_{\text{surf}}}\rho\xi_r^2(r)\left(\frac{r}{R_{\text{phot}}}\right)^2\,dr. \tag{2.17}$$

Eq. (2.16) is evaluated at different angular frequencies. For frequency values not equal to mode eigenfrequencies, the eigenfunction is not directly available, so we linearly interpolate $\partial_r\xi_r$ to our target frequency value (see also the Appendix in SN01). Recall that $\Delta\langle E_\omega\rangle_{\text{ens}}/\Delta t$ is the excitation rate per unit area, to get global excitation rate we multiply $\Delta\langle E_\omega\rangle_{\text{ens}}/\Delta t$ by the horizontal area[6] of the simulation, that is, 36 Mm^2.

Global excitation rates from the simulation (both original and smoothed data) are displayed in Fig. 2.6, together with excitation rates extracted from observations (Chaplin et al., 1998). Broadly speaking, excitation rates predicted from simulation agree well with observations. The simulation result demonstrates a strong fluctuation with frequency, which stems from non-adiabatic pressure fluctuation (Fig. 2.2). Its overall trend is also clear from the smoothed curve — excitation rate is small at lower frequencies, increases rapidly with increasing frequency, reaches a plateau that ranges from ~ 2.5 mHz to ~ 4 mHz, then starts to decline at higher frequencies. The trend observed in Fig. 2.6 can be explained by analysing the behaviour of two key ingredients in Eq. (2.16), namely $(\partial_r\xi_r)^2/E_0$ and $\delta\bar{P}_{\text{nad}}$.

The normalized eigenfunction gradient $(\partial_r\xi_r)^2/E_0$ quantifies the fluid's compression associated with oscillations: the larger the value of the gradient is, the stronger the compression locally. An extreme case is $\partial_r\xi_r = 0$, where the oscillation amplitude does not vary locally to first order and fluid elements move in sync and no compression occurs anywhere. As shown in Fig. 2.5, for the lower frequency mode, compression is weak throughout the simulation domain while for the higher frequency one, strong compression occurs around and above photosphere. The reason for this is, as mentioned in Sect. 2.2 and demonstrated in Fig. 2.4, lower frequency p-modes have greater amplitude in the deep interior of star where density is significantly higher. As a result, if two modes have same kinetic energy, the lower frequency mode will show smaller amplitude and smaller compression compared to the higher frequency one because of its large "mode inertia" (a mode's tendency to remain unchanged, in

[6]Not by the total surface area of the Sun $4\pi R_{\text{phot}}^2$; the underlying reason is explained in NS01 Sect. 3.3 and Stein et al. (2004) Sect. 5.

analogue to the inertia of normal matter). On the other hand, there are two obvious features for $\delta\bar{P}_{\rm nad}$. First, the magnitude of (non-adiabatic) pressure fluctuations decreases with increasing frequency, which is in line with what shown in Fig. 2.2. Second, for both frequencies in Fig. 2.5, pressure fluctuations diminish drastically in the photospheric layers, where energy balance is controlled primarily by radiative processes and convective turbulence is comparatively small.

Putting the two aspects together allows us to investigate the value of the work integral (also referred to as "PdV work", where "P" stands for the pressure fluctuation and "dV" is the compression of fluid caused by oscillations) throughout the simulation domain. For lower frequency oscillations, weak compression is coupled with strong pressure fluctuations around and below the photosphere, whereas for higher frequency oscillations, major contributions to the PdV work come from a small region around the photosphere, below which the compression of fluid is small, above which pressure fluctuations are small.

In summary, energy transfer from convective motions to oscillations is carried out by non-adiabatic effects such as convective turbulence and entropy fluctuations. The amount and rate of energy injection into the modes is governed by two main aspects, the magnitude of pressure fluctuation and the strength of local compression to fluid. The former is strong at low frequencies, and decays with increasing frequency (Fig. 2.2) while the latter exhibits an opposite trend (Fig. 2.5). As a result, excitation rates at low and high frequencies are limited by oscillations (local compression) and convection (pressure fluctuations), respectively. Finally, we note that the numerical results and main conclusions in this section are qualitatively in agreement with SN01 in general, although our solar model differs from theirs.

2.4 Damping rates

The stochastic excitation mechanism discussed in Sect. 2.3 is responsible for the driving of p-mode oscillations. However, the amplitude of excited mode cannot grow infinitely large because it is limited by another effect called mode damping, the dissipation of mode kinetic energy to surroundings. Therefore, the final equilibrium oscillation amplitude results from the balance between stochastic excitation (energy gain) and mode damping (energy loss). The energy dissipation process is quantified by the *damping rate* η which describes how fast is the e-folding (decay by a factor of e) of mode energy. In this section, we outline how damping rates at different frequencies are computed from first principles, and present our results for radial oscillations of the Sun.

The (linear) damping rate can be derived from first order perturbation theory, with non-adiabatic effects as small perturbation (cf. Aerts et al. 2010 Sect. 3.7),

$$\eta = \frac{\omega \int_{y_{\rm bot}}^{y_{\rm top}} \mathfrak{Im}\left\{(\delta\bar{\rho}^*/\bar{\rho}_0)\delta\bar{P}_{\rm nad}\right\} dy}{4m_{\rm mode}|\tilde{v}_y(R_{\rm phot})|^2}, \tag{2.18}$$

where star symbol represents complex conjugate. $m_{\rm mode}$ and $\tilde{v}_y$ are mode mass per

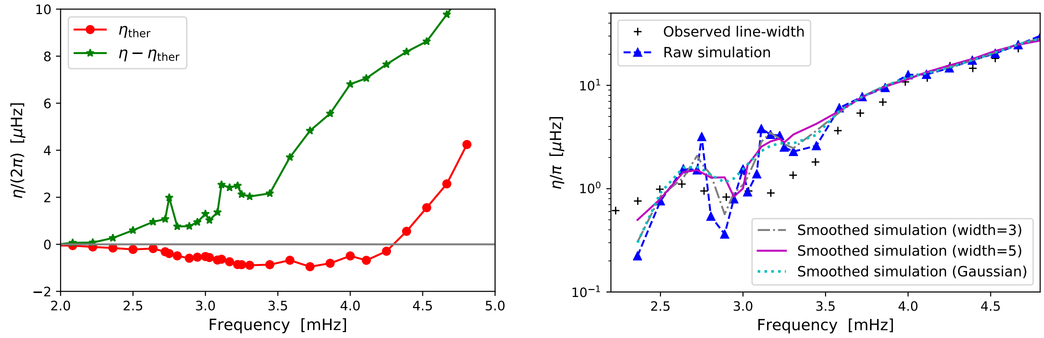

(a) (b)

Figure 2.7: Linear damping rates at different cyclic frequencies for the Sun, computed from 3D simulation as described in Sect. 2.4. Left panel: red dots are contribution to damping rate from thermal pressure fluctuation while total damping rate minus thermal pressure contribution (green asterisks) mainly reflect damping due to turbulent convection. Right panel: total damping rates from simulation (raw data in blue triangles, smoothed data in magenta, grey dash-dot and cyan dotted line) are divided by π in order to compare with observed line widths (plus mark) from BiSON $l = 0$ data (Chaplin et al., 1998). The magenta and grey curves are obtained by taking the running mean of the raw simulation data with a width of five and three data points respectively, whereas the cyan dotted line results from smoothing the raw simulation data by a Gaussian kernel with full width at half maximum equals to 0.25 mHz.

unit area and vertical velocity amplitude respectively, they are connected to mode kinetic energy (per unit surface area) by $m_{\rm mode}|\tilde{v}_y(R_{\rm phot})|^2 = E_0$ (NS01 Eq. 63). The integral at numerator is the work integral which depend on (non-adiabatic) pressure and density fluctuation as well as the phase difference between them. The density fluctuation $\delta\rho$ quantifies the extent of local compression, it is related to mode displacement vector by the perturbed fluid continuity equation:

$$\nabla \cdot \delta\vec{r} = -\frac{\delta\rho}{\rho_0}. \tag{2.19}$$

Furthermore, the sign of η is a criterion of mode stability: positive η implies stable mode whose amplitude decays exponentially with time if no energy is supply from, for instance, convection; negative η, also called growth rate in this scenario, suggests that mode with finite amplitude will continue to drain energy from surrounding until the amplification is halted by nonlinear effects. Solar radial modes studied in this work are believed to be stable (Houdek & Dupret 2015 Sect. 6.3).

It is worth noting that while the mode displacement vector (or equivalently, the eigenfunction) and density fluctuation is related through (2.19), the *adiabatic* eigenfunction ξ_r obtained from ADIPLS cannot be applied to the calculation of *non-adiabatic* pressure fluctuation. To this end, all components in Eq. (2.18), except for $m_{\rm mode}$, must be extracted directly from simulation. Nevertheless, as first proposed by Nordlund

& Stein (1998), it is challenging to separate coherent fluid motion from the turbulent convective processes in simulations. More specifically, ideally, density fluctuations should only contain the contribution from collective fluid motions (i.e. oscillations). But in reality, owing to the complexity of physical processes occurring in the simulation domain, $\delta\bar{\rho}/\bar{\rho}_0$ computed from simulation consists not only pulsation signals but also the signature of "convective noises". This effect is particularly evident for modes that do not naturally emerge in simulations (i.e. radial modes other than the three simulation modes shown in Fig. 2.1). In order to obtain a $\delta\bar{\rho}/\bar{\rho}_0$ that cleanly reflects the contribution from mode eigenfunction, in other words, a coherent density fluctuation, we conduct numerical experiments that artificially drive radial mode at a particular frequency to large amplitude. The target mode will be prominent in the simulation box and distinguishable from "convective noise".

The artificial driving is achieved by modifying the boundary condition of the simulation. Namely, we impose a small time-dependent perturbation to thermal (gas plus radiation) pressure at the bottom boundary while keep the entropy constant (in first order) at the same time to ensure no extra energy is injected to the system. The applied thermal pressure perturbation varies sinusoidally with time and remains uniform over horizontal plane, since radial modes are the focus here.

The perturbation at the bottom boundary will generate coherent fluid motion with the same frequency as the driving frequency, and amplify vertical velocity, density and pressure fluctuation to unrealistically large magnitudes. Nevertheless, we claim that such artificial driving would not compromise the reliability of our damping rate result because the rates of $\delta\bar{\rho}$, $\delta\bar{P}_{\rm nad}$ and $\tilde{v}_y$ enhancement are similar to each other, so that the artificial effect from "mode driving" largely cancels out between $(\delta\bar{\rho}^*/\bar{\rho}_0)\delta\bar{P}_{\rm nad}$ and $|\tilde{v}_y(R_{\rm phot})|^2$ when we compute damping rate at the driving frequency using Eq. (2.18).

Such numerical experiment is repeated at different driving frequencies in order to obtain theoretical damping rates as a function of cyclic frequency. In Fig. 2.7(a) we separate the contribution to η due to thermal pressure fluctuation,

$$\delta\bar{P}_{\rm ther}(t) = \bar{P}_{\rm ther,L}(t) - \bar{P}_{\rm ther,0,L}. \tag{2.20}$$

$\delta\bar{P}_{\rm ther}$ stems from the divergence of radiative and convective fluxes (Stein & Nordlund 1991 Sect. 3) which is most prominent near photosphere where the transition between radiative and convective heat transport occurs. For frequencies span from ~ 2 mHz to ~ 4 mHz, thermal pressure fluctuation is responsible for destabilizing modes, qualitatively in line with what found in Houdek et al. (1999). On the other hand, another major contribution to mode damping is convective turbulence. The positive-definite $\eta - \eta_{\rm ther}$ indicate that turbulence tends to dissipate mode energy at all frequencies. That is to say, solar radial modes excited by turbulent convection is actually damped by the same effect, in accordance with the assertion in Houdek & Dupret (2015) Sect. 6.3.

Also, in Fig. 2.7(b), our numerical results are compared with line width[7] of $l = 0$

[7]When observing time is much greater than the mode e-folding time, damping rate is related to line

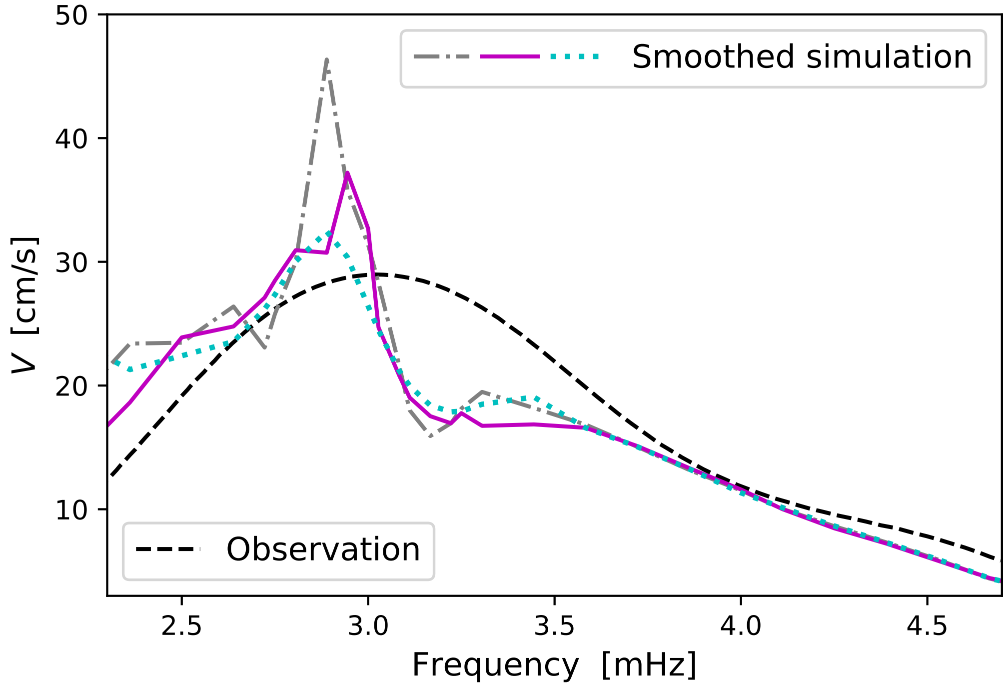

Figure 2.8: Predicted photosphere velocity amplitude as a function of cyclic frequency, as evaluated using Eq. (2.25). Magenta, grey dash-dot and cyan dotted lines denote theoretical results from different smoothing options for damping rates (see Fig. 2.7(b)). The mean radial velocity amplitude derived from BiSON data (Kjeldsen et al., 2008, black dashed line) has been smoothed and divided by the projection factor 0.724 to enable a direct comparison between simulations and observation.

modes collected by BiSON (Chaplin et al., 1998). Good agreements are found at high and intermediate frequencies. The observed damping rate plateau around 2.8 mHz is also well predicted. However, as can be seen from Fig. 2.7(b), the accuracy of our results at low-frequency ($\nu \lesssim 2.5$ mHz) is restricted by the depth of simulation domain. As shown in Fig. 2.4, low-frequency radial modes have considerable oscillation amplitude in solar interior. Because work integral is truncated at the bottom of simulation box in practice, contributions from deeper layers are omitted hence the final damping rates are systematically lower than observed values at low frequencies.

2.5 Estimate velocity amplitude and $\nu_{\rm max}$ from simulation

The observed oscillation amplitudes result from the balance between stochastic excitation and mode damping. With both of them available from the simulation, we are able to evaluate (theoretical) oscillation amplitude, then estimate the frequency of maximum oscillation power $\nu_{\rm max}$.

width Γ by $\Gamma = \eta/\pi$ (Chaplin et al., 2005).

For an observed mode in equilibrium state (in other word, constant amplitude), its energy gain and loss must be equal, that is

$$\mathcal{P}_{\rm exc} + \frac{dE_{\rm osc}}{dt} = 0. \tag{2.21}$$

Here $\mathcal{P}_{\rm exc}$ is the excitation rate of this mode, and $E_{\rm osc}$ is its kinetic energy whose canonical form is (Aerts et al. 2010 Eq. 3.141)

$$E_{\rm osc} = \frac{1}{2} M_{\rm mode} V_{\rm rms}^2, \tag{2.22}$$

where $M_{\rm mode}$ is mode mass (not to be confused with mode mass per unit area $m_{\rm mode}$) and $V_{\rm rms}$ being root-mean-square (rms) velocity at photosphere. The evolution of kinetic energy for a damped oscillator follows $E_{\rm osc} \propto \exp(-2\eta t)$, therefore

$$E_{\rm osc} = \frac{\mathcal{P}_{\rm exc}}{2\eta}. \tag{2.23}$$

Combining Eqs. (2.22) and (2.23) gives the expression of the rms velocity:

$$V_{\rm rms} = \sqrt{\frac{\mathcal{P}_{\rm exc}}{M_{\rm mode}\eta}}. \tag{2.24}$$

The mean kinematic velocity amplitude at the photosphere due to one oscillation mode is then

$$V = \sqrt{2} V_{\rm rms} = \sqrt{\frac{2\mathcal{P}_{\rm exc}}{M_{\rm mode}\eta}}. \tag{2.25}$$

Note that V is not an asteroseismic observable hence cannot be compared with observations directly. What is obtained from analysing the Doppler shift of spectral lines (spectroscopic measurement of stellar oscillation) is the radial velocity. The source of this radial velocity is indeed the kinematic velocity of the fluid, whereas the quantity one measures is affected also by limb darkening and other geometric effects (Aerts et al., 2010). These two kinds of velocities are connected by projection factor S_{nlm} (also named spatial response function) that accounts for these effects (Christensen-Dalsgaard & Gough 1982 Eq. 4.1),

$$\mathfrak{v}_{nlm} = S_{nlm} V_{nlm}, \tag{2.26}$$

where $\mathfrak{v}_{nlm}$ is the observed mean radial velocity amplitude of p-mode with quantum number (n, l, m). Christensen-Dalsgaard (1989) has shown that the projection factor for $l = 0$ modes of the Sun is 0.724. Equations (2.25) and (2.26) therefore enable comparison between the predicted velocity amplitude and the observed mean radial velocity amplitude.

The theoretical V is computed based on Eq. (2.25), with smoothed excitation and damping rates evaluated in Sect. 2.3.3 and 2.4, respectively. Smoothed instead of raw simulation data are applied to calculate V in order to avoid strong random fluctuation in the latter and to make V comparable with observations. The power spectrum of the observed radial velocity is also smoothed. Mode mass is calculated from 1D patched solar model (see Sect. 2.3.2) using ADIPLS. The thus computed velocity amplitude is shown in Fig. 2.8, together with the observed radial velocity spectrum taken from Kjeldsen et al. (2008).

Moderate agreement between simulation and observation is found: velocity amplitude predicted from simulation is in the same order of magnitude as the observationally inferred value, and the overall shape of $V-\nu$ curve also resembles observation. In the mean time, we do notice that there are mismatches between the two, especially within $3 \lesssim \nu \lesssim 3.5$ mHz. In this frequency interval we underestimated excitation rates (Fig. 2.6) and overestimated damping rates (Fig. 2.7). Errors on both aspects overlay then propagate into V results.

In spite of the discrepancy between simulation and observation in the absolute magnitude of the velocity amplitude, we are still able to provide an estimate for $\nu_{\rm max}$ from the simulation. In the context of spectroscopic measurement of stellar oscillation, the frequency of maximum power is the corresponding frequency where the mean observed radial velocity reaches its maximum. This criterion is adopted in Kjeldsen et al. (2008) where they obtain $\nu_{\rm max} = 3.1$ mHz for the Sun. As an analogy, the maximum of theoretical V then predicts a theoretical solar $\nu_{\rm max}$ which, from Fig. 2.8, is ~ 3.0 mHz. We note that the exact theoretical $\nu_{\rm max}$ value from the 3D solar simulation is somewhat ambiguous because it depends on how exactly the smoothing is performed (Fig. 2.8).

Finally, we clarify why photosphere velocity should be computed via Eq. (2.25). On the surface it seems photosphere velocities are directly available from 3D simulation (Fig. 2.1), then why calculate it semi-analytically? Here we emphasize neither photosphere velocity adopted from "normal" 3D simulation nor from artificial mode driving experiment is comparable with V. The reason for the latter is obvious – artificial driving will amplify oscillation at a particular frequency to unrealistically large amplitude, therefore the absolute value of photosphere velocity in such numerical experiment has no physical meaning. (Damping rate value, however, is reliable because of the cancellation between $(\delta\bar{\rho}^*/\bar{\rho}_0)\delta\bar{P}_{\rm nad}$ and $|\tilde{v}_y(R_{\rm phot})|^2$, as discussed in Sect. 2.4.)

Using photosphere velocity directly from a "normal" 3D simulation is also inappropriate. From Fig. 2.1 it is clear that vertical velocity of the intermediate-frequency simulation mode is on the order of 1 km/s, much larger than the observed velocity amplitude of individual p-mode which is on the order of 1 m/s (Fig. 2.8). The mismatch between simulated and observed velocity results from the limited volume of the simulation domain. As demonstrated in previous sections, 3D solar simulation is able to predict realistic mode excitation and damping rates with their absolute value similar to what deduced from helioseismic observations. Because mode kinetic energy $E_{\rm osc}$ is dictated by excitation and damping processes (Eq. (2.23)), $E_{\rm osc}$ from the simulation is comparable to the actual kinetic energy of solar radial modes. However, in simulations, oscillations are confined in the simulation domain whereas for the Sun, radial modes oscillate throughout the entire solar surface and interior. Given the similarity in kinetic energy and the difference in cavity volume, it is apparent that the finite size of simulation will lead to larger oscillation amplitude. The velocity directly from the simulation is not a realistic representation of solar mode amplitude unless proper scaling is performed, as also discussed in Belkacem et al. (2019).

2.6 Conclusions

In this paper, we investigated how radial oscillations in the Sun are excited and damped based on 3D hydrodynamical simulation of solar near-surface region. Our simulation provides a realistic model of fluid motions and heat transport around photosphere. Its *ab initio* nature also allows us to compute mode excitation and damping rates in an essentially parameter-free manner.

For the excitation rate, we adopted the theoretical framework developed by NS01 and SN01. Ingredients in the expression of excitation rate are calculated directly from simulation. Our numerical results demonstrate that mode excitation is weak at low frequencies, it increases rapidly with frequency and reaches its maximum between 2.5 mHz and 4 mHz, then start to decline at higher frequencies. It is also verified that mode excitation stems from the coupling between convection-induced pressure fluctuation and pulsation-induced fluid compression. Excitation rates computed in the current work is consistent with previous theoretical investigation (e.g., SN01) and corresponding solar observation.

A novel numerical technique is applied to extract (linear) damping rates from simulations. In order to separate the fluctuation caused by pulsation from convective effects, we artificially drive a target radial oscillation to large amplitude, then compute damping rate from such simulation using analytical formula (2.18). Broad agreement is achieved between simulation and observation, especially for higher frequency modes. The damping rate "plateau" around 2.8 mHz is also observed. What is more, by analysing different aspects that contribute to mode damping, we found thermal processes tend to destabilize radial modes with frequency between 2 mHz and 4 mHz while convective turbulence, which is responsible for mode driving, is also the main effect that dissipates them. This conclusion is in agreement with the findings by Houdek et al. (1999), although the latter calculated mode damping in a radically different way.

With both mode excitation and damping rates extracted from the model, it is possible to produce a prediction for the theoretical velocity spectrum, from which $\nu_{\max}$ can be estimated. The velocity amplitude is obtained by assuming exact balance between energy gain from stochastic excitation and energy loss by linear damping. Based on the synthetic velocity amplitude, we report, to our knowledge, the first pure theoretical $\nu_{\max}$ estimation for the Sun. Theoretical velocity amplitude and $\nu_{\max}$ are compared with observationally inferred values from Kjeldsen et al. (2008) with an encouraging agreement.

The major highlight of the current work is that all results are based on first principles. Given the 3D simulation of solar convection introduced in Sect. 2.2, the formulation we present does not depend on any free parameter that need to be calibrated from observation or other theoretical models. In addition, our method enables a detailed analysis of the interaction between convection and pulsations. From the simulation it is also possible to isolate from each other the different factors contributing to mode excitation or damping. In short, 3D numerical simulations provide full information about physical processes happened in solar near-surface region, some of them, such as the work integral, are difficult to probe by observation or traditional 1D models.

On the other side, results from observation can be used to assess how well p-mode oscillations are modelled by 3D simulations, given that these two methods are completely independent. As mentioned in earlier sections, excitation and damping rates, as well as velocity amplitude evaluated from 3D simulation agree with corresponding observation in general, which indicates solar oscillations are overall properly simulated in this work. However, we caution that discrepancies between numerical results and solar observations do exist in both excitation and damping rates. The differences then propagate into synthetic velocity amplitude and theoretical $\nu_{\rm max}$. These mismatches are indicative of shortcomings in our numerical simulations (or analytical formulation). Among them, the most notable one is the spacial size and time span of simulation. The finite depth in 3D model actually truncates the work integral, limiting it in the simulation domain. Thus additional contributions from outside the simulation box are neglected. Temporally, although 3D simulation used in this work is extremely long (compared to 3D solar model generated for other purposes such as spectra synthesis, which normally cover approximately only one hour of solar time (Magic et al., 2013a)) in time, the time sequence is still far from enough to resolve all radial modes excited in the Sun. Modelling of excitation and damping of modes would benefit from having a model that is more extended in depth and has a longer duration. Nevertheless, the main restriction in this respect remains computational time. Apart from the size of simulation, we also note that our analysis is strictly restricted to radial modes. In reality, the frequency of maximum oscillation power is determined from the full solar velocity spectrum which contains also non-radial p-modes. Hence, extracting $\nu_{\rm max}$ from radial modes only is a simplified approach. Nonetheless, we claim that this simplification might not be a significant flaw, because solar oscillation spectra are dominated by p-modes with degree $l = 0 - 3$ (Aerts et al. 2010 Sect. 7.1.3) which are all radial or near-radial oscillations. Our formulation therefore should also hold approximately for these low-degree p-modes.

Chapter 3

Convective Excitation and Damping of Solar-like Oscillations

Yixiao Zhou, Martin Asplund, Remo Collet and Meridith Joyce, *Convective Excitation and Damping of Solar-like Oscillations*, 2020, Monthly Notices of the Royal Astronomical Society, 495, 4904.

Abstract

The last decade has seen a rapid development in asteroseismology thanks to the *CoRoT* and *Kepler* missions. With more detailed asteroseismic observations available, it is becoming possible to infer exactly how oscillations are driven and dissipated in solar-type stars. We have carried out three-dimensional (3D) stellar atmosphere simulations together with one-dimensional (1D) stellar structural models of key benchmark turn-off and subgiant stars to study this problem from a theoretical perspective. Mode excitation and damping rates are extracted from 3D and 1D stellar models based on analytical expressions. Mode velocity amplitudes are determined by the balance between stochastic excitation and linear damping, which then allows the estimation of the frequency of maximum oscillation power, $\nu_{\rm max}$, for the first time based on *ab initio* and parameter-free modelling. We have made detailed comparisons between our numerical results and observational data and achieved very encouraging agreement for all of our target stars. This opens the exciting prospect of using such realistic 3D hydrodynamical stellar models to predict solar-like oscillations across the HR-diagram, thereby enabling accurate estimates of stellar properties such as mass, radius and age.

3.1 Introduction

Asteroseismology provides a unique window to revealing the physical properties of stars. For solar-like oscillations – acoustic waves (so-called p-modes) excited and damped by near surface convection, global asteroseismic observables – the large frequency separation $\Delta\nu$ and frequency of maximum oscillation power $\nu_{\rm max}$ are linked to the stellar radius and mass by the seismic scaling relations (Brown et al., 1991;

Kjeldsen & Bedding, 1995). Measured individual oscillation frequencies can further constrain the physics of stellar interiors, for instance the size of the convection zone (Basu & Antia, 1997; Deheuvels et al., 2016) or the rotation rate of the stellar core (Mosser et al., 2012b), which are difficult to probe by other means. In addition to global asteroseismic observables and individual oscillation frequencies, other observables such as mode amplitude and line width encrypt information about how oscillations are excited and damped in the star, a fundamental problem in stellar physics that is still not fully understood.

Significant progress toward this problem has been made from the observational side thanks to high-quality asteroseismic data from the *CoRoT* (Michel et al., 2008), *Kepler* (Borucki et al., 2010) and *TESS* (Ricker et al., 2015) missions, as well as ground-based telescopes such as SONG (Stellar Oscillations Network Group, Grundahl et al. 2006). With measured oscillation amplitudes and line widths available for thousands of solar-type oscillators, it is now possible to investigate the excitation and damping of p-mode oscillations across the Hertzsprung-Russell (HR) diagram. Indeed, empirical relations between oscillation amplitudes, mode line widths, and fundamental stellar parameters have been derived (Chaplin et al., 2009; Huber et al., 2011b; Appourchaux et al., 2012; Lund et al., 2017; Vrard et al., 2018) for main-sequence, subgiants and red giant stars. Oscillation amplitudes are proportional to the luminosity-mass ratio of the star, while line width, which is closely related to mode damping rate, increases with the effective temperature of the star.

On the theoretical side, realistic models of mode excitation and damping can illuminate the underlying physics of the oscillations. The first step is to model the mode excitation and damping for the Sun. Following the key insight by Goldreich & Keeley (1977b) that solar p-mode oscillations are driven by turbulent convection, Balmforth (1992a,b) analytically quantified the excitation and damping rate of solar p-mode, then evaluated the oscillation amplitude for the Sun using the non-local mixing length theory (MLT) of convection in 1D models. His pioneering work demonstrated that solar five-minute oscillations are intrinsically stable and that the calculated mode damping rates and velocity amplitude agrees reasonably well with helioseismic observations. Based on Balmforth (1992a)'s theoretical formulation, Houdek et al. (1999) studied excitation, damping rates and velocity amplitudes of solar-like oscillations for a grid of 1D models that corresponds to main-sequence stars. Their results indicate that the mode velocity amplitude is proportional to the luminosity-mass ratio for solar-type oscillators, quantitatively confirming the amplitude scaling relation proposed earlier by Kjeldsen & Bedding (1995). These and other (e.g. Samadi & Goupil 2001; Belkacem et al. 2012) studies have improved our understanding of p-mode oscillations in solar-type stars. However, due to the lack of realistic theory of convection, which is ultimately driving the oscillations, the theoretical prescriptions adopted in these works inevitably involve adjustable parameters, making independent theoretical predictions of excitation and damping difficult.

An alternative approach that has shown great promise for overcoming this difficulty is to evaluate excitation and damping rates from first principles using 3D hydrodynamical convection simulations. Nordlund & Stein (2001) and Stein & Nordlund

(2001) extracted the excitation rates of solar radial modes directly from 3D simulations of near-surface layers of the solar convective region. Zhou et al. (2019) quantified both the excitation and damping rates for solar radial modes and estimated velocity amplitude and theoretical $\nu_{\rm max}$ for the Sun based on their 3D solar atmosphere model. Without introducing any tunable free parameters, very encouraging agreement between theoretical results and corresponding helioseismic observations are achieved with this approach. In this paper, we apply the theoretical formulation and numerical technique described in Zhou et al. (2019) to four other key benchmark turn-off and subgiant stars to examine whether our method is applicable to other solar-type oscillating stars or not and to investigate how excitation and damping processes vary across the HR diagram. We also explore in detail how radial oscillations are damped in the near-surface region of stars, which has recently been studied by Belkacem et al. (2019) for the solar case.

3.2 Modelling

3.2.1 Target stars

The target stars investigated in this work are KIC 6225718, Procyon A, β Hydri and δ Eridani (δ Eri). All of them are late-type, intermediate-mass (between $1M_\odot$ and $1.5M_\odot$) stars with metallicity [Fe/H][1] near the solar value. Solar-like oscillations have been unambiguously detected for all of our targets, and well-determined $\Delta\nu$ and $\nu_{\rm max}$ are available. Their fundamental stellar parameters and global asteroseismic parameters are listed in Table 3.1 and 3.2, respectively. We introduce the basic properties of the four stars individually below.

KIC 6225718 (HD 187637) is an F-type main-sequence star observed by the *Kepler* satellite for a long timespan. Based on high-quality *Kepler* data, Silva Aguirre et al. (2012) obtained global oscillation parameters, i.e. $\Delta\nu$ and $\nu_{\rm max}$, for this star. More detailed studies on the oscillation properties of KIC 6225718 were carried out by Lund et al. (2017), who identified more than 50 oscillation modes and determined their frequencies with uncertainties of typically 1 ¯Hz. Moreover, Lund et al. (2017) provided the measured line width and mode amplitude for each radial p-mode, which enables detailed comparison between observation and theoretical stellar models. Accurate atmospheric parameters of KIC 6225718 are also available from previous work. Bruntt et al. (2012) determined the effective temperature of this star, $T_{\rm eff} = 6230 \pm 60$ K, and metallicity $[{\rm Fe/H}] = -0.17 \pm 0.06$ by fitting the stellar spectra with a fixed surface gravity ($\log g = 4.32$, cgs unit), which is determined from asteroseismology. On the modelling side, KIC 6225718 has been investigated in detail by Tian et al. (2014), Silva Aguirre et al. (2017) and Houdek et al. (2019). Tian et al. (2014) adopted the fundamental stellar parameters from Bruntt et al. (2012) as basic constraints and measured $l = 0, 1, 2$ p-mode frequencies as seismic constraints for their

[1] $[{\rm A/B}] = \log(n_{\rm A}/n_{\rm B}) - \log(n_{\rm A}/n_{\rm B})_\odot$ where $n_{\rm A}/n_{\rm B}$ and $(n_{\rm A}/n_{\rm B})_\odot$ represent number density ratio between element A and B in the star and the Sun, respectively.

Table 3.1: Fundamental stellar parameters of KIC 6225718, Procyon, β Hydri and δ Eri. Reference values are adopted from various literature, determined either from observation or detailed stellar modelling. The basic parameters of our 1D MESA models and 3D STAGGER models for these stars are also shown. In 3D models, the effective temperature fluctuates over time therefore both mean effective temperature and its standard deviation are given.

Stellar parameter		$T_{\rm eff}$ [K]	$\log g$ (cgs)	[Fe/H]	$M/M_{\odot}$	$R/R_{\odot}$
	Reference	6230 ± 60 (a)	$4.319^{+0.007}_{-0.005}$ (b)	-0.17 ± 0.06 (a)	$1.10^{+0.04}_{-0.03}$ (c)	1.22 ± 0.01 (c)
KIC 6225718	1D model	6217	4.318	-0.14	1.14	1.225
	3D model	6231 ± 14	4.319	0		
	Reference	6543 ± 84 (d)	4.00 ± 0.02 (e)	-0.03 ± 0.07 (f)	1.461 ± 0.025 (g)	2.031 ± 0.013 (d)
Procyon	1D model	6554	3.99	0.01	1.47	2.022
	3D model	6553 ± 23	4.00	0		
	Reference	5873 ± 45 (e)	3.98 ± 0.02 (e)	-0.04 ± 0.06 (e)	1.04 (h)	1.810 ± 0.015 (g)
β Hydri	1D model	5861	3.96	-0.06	1.09	1.814
	3D model	5893 ± 14	3.98	0		
	Reference	4954 ± 30 (e)	3.76 ± 0.02 (e)	0.06 ± 0.05 (e)	1.13 ± 0.05 (e)	2.327 ± 0.029 (g)
δ Eri	1D model	4948	3.76	0.06	1.17	2.352
	3D model	4958 ± 11	3.76	0		

Reference: (a): Bruntt et al. (2012); (b): Lund et al. (2017); (c): Tian et al. (2014); (d): Aufdenberg et al. (2005); (e): Heiter et al. (2015); (f): Bergemann et al. (2012); (g): Bruntt et al. (2010); (h): Brandão et al. (2011)

Table 3.2: Global asteroseismic parameters of KIC 6225718, Procyon, β Hydri and δ Eri. Theoretical $\Delta\nu$ are derived following the method of White et al. (2011). For Procyon, the value of $\nu_{\max}$ is uncertain because the observed oscillation spectrum exhibits a broad plateau between 600 and 1200 μHz (Arentoft et al., 2008).

Star	$\Delta\nu$ [μHz]		$\nu_{\max}$ [μHz]	
	Observed	Modeling	Observed	Modeling†
KIC 6225718	105.7 (a)	106.3	2364 (a)	2300
Procyon	55 (b)	56	—	—
β Hydri	57.24 (c)	58.37	1000 (c)	980
δ Eri	40.25 (d)	40.45	677 (d)	650

Reference: (a): Lund et al. (2017); (b): Bedding et al. (2010); (c): Bedding et al. (2007); (d): TESS data (E. Bellinger, in preparation)
†: Note that the numbers listed here are only estimations, as the exact value of theoretical $\nu_{\max}$ depends on how simulation data are smoothed.

model. They estimated the most probable mass and radius of KIC 6225718 to be $M = 1.10^{+0.04}_{-0.03} M_\odot$, $R = 1.22 \pm 0.01 R_\odot$. Silva Aguirre et al. (2017) modelled this star using observational constraints from Lund et al. (2017). Their modelling involved various stellar evolution codes, input physics, fitting methods (see Silva Aguirre et al. 2017 Sect. 3 for details), resulting in a stellar mass $M = 1.2133 \pm 0.035 M_\odot$ and a radius of $R = 1.2543 \pm 0.0133 R_\odot$. Houdek et al. (2019), on the other hand, focused on modelling the line width and corrections to adiabatic oscillation frequencies for KIC 6225718 using the non-local, time-dependent convection model (Balmforth, 1992a; Houdek et al., 1999).

Procyon A (HD 61421) is an F5 star with a white dwarf companion in a binary system and is one of the nearest stars to Earth. Owing to its proximity and brightness, Procyon A (hereinafter Procyon) is of particular importance to study. Therefore, much effort has been put into determining its fundamental parameters accurately. Among these efforts, Aufdenberg et al. (2005) measured the angular diameter of Procyon using interferometry. Together with the bolometric flux obtained from various instruments and the *Hipparcos* parallax, they derived the radius and effective temperature to be $R = 2.031 \pm 0.013 R_\odot$ and $T_{\rm eff} = 6543 \pm 84$ K. The mass of Procyon is comparably well-constrained because it resides in a binary system. We adopt the orbital mass provided by Bruntt et al. (2010): $M = 1.461 \pm 0.025 M_\odot$. The metallicity of Procyon has likewise been scrutinized in depth. Allende Prieto et al. (2002) analysed the spectrum of Procyon with a focus on the iron abundance determination from a 3D model atmosphere. Their 3D model was able to reproduce the observed Fe line profiles, yielding an iron abundance for Procyon of $\log \varepsilon_{\rm Fe} = 7.36 \pm 0.03$ dex, slightly lower than the solar value ($\log \varepsilon_{\rm Fe,\odot} = 7.41 \pm 0.02$ dex derived in the same paper). More recently, Bergemann et al. (2012) performed 3D, non-local thermodynamic equilibrium (non-LTE) Fe line formation calculations for several late-type stars including Procyon based on up-to-date atomic data. With basic stellar parameters adopted from Aufdenberg et al. (2005), they obtained the metallicity of Procyon to be [Fe/H] $= -0.03 \pm 0.07$. Both works confirmed that Procyon is a solar-metallicity star.

Procyon is also a favourable target for asteroseismology. Solar-like p-mode oscillations in Procyon were first announced by Brown et al. (1991). More than a decade later, Arentoft et al. (2008) conducted intensive radial velocity measurements for Procyon using 11 spectrographs at eight observatories. They found clear oscillation signatures from radial velocity variation and obtained velocity amplitude which demonstrated a plateau between 0.6 mHz and 1.2 mHz. Bedding et al. (2010) subsequently extracted individual oscillation frequencies ranging from 0.3 mHz to 1.4 mHz, indicating a broad spectrum of stochastically excited p-modes in Procyon. Using individual mode frequencies as constraints, Doğan et al. (2010) and Guenther et al. (2014) performed asteroseismic modelling for Procyon. Both works predicted a stellar mass close to $1.5 M_\odot$. The latter also concluded that the star is still in the core-hydrogen burning phase.

β **Hydri (HD 2151)** is the closest subgiant to Earth, making it an excellent object for investigation. In this work we choose stellar parameters provided in Heiter et al. (2015) as reference values: $T_{\rm eff} = 5873$ K, $\log g = 3.98$ dex, [Fe/H] $= -0.04$ dex; The effective temperature is deduced from bolometric flux and angular diameter measured by North et al. (2007). β Hydri is a benchmark star in asteroseismology as well – it is one of the first subgiants confirmed as a solar-type oscillator. Bedding et al. (2001) reported clear p-mode oscillation signatures in β Hydri and estimated the frequency of maximum power around 1 mHz. The follow-up study by Bedding et al. (2007) further extracted individual mode frequencies and revealed the existence of mixed modes[2] in the star. Brandão et al. (2011) subsequently reanalysed the observational data. With updated mode frequencies as constraints, they presented interior models for β Hydri. Additionally, we note that β Hydri has recently been observed by TESS, which may supply more information about the oscillation properties of this star.

δ **Eri (HD 23249)** is a solar-metallicity K-subgiant included among the *Gaia* benchmark stars (Heiter et al., 2015). This star is ascending the red giant branch and its age is estimated to be $6-9$ Gyr (Sahlholdt et al., 2019), which makes it both the most evolved and the oldest star in our sample. Solar-like oscillations of δ Eri were first reported by Bouchy & Carrier (2003) who found a clear oscillation signature around 0.7 mHz. It is worth noting that δ Eri has recently been observed simultaneously by SONG and TESS (E. Bellinger, in preparation) so that both spectroscopic (radial velocity) and photometric (intensity) measurements of oscillation are available for this star, which allows detailed comparison between theoretical and measured oscillation

[2] In evolved stars such as subgiants and red giants, the evanescent layer between p-mode and g-mode cavity can be very thin, especially for $l = 1$ modes. The coupling of oscillation cavities will result in a mixed character of some modes, which are excellent tools to probe the stellar core. See Hekker & Christensen-Dalsgaard (2017) for a thorough review.

properties. However, currently no measured mode line width data are available for δ Eri. Therefore, theoretical damping rates of this star are compared with measured line widths of KIC 5689820 (cf. Sect. 3.3 and 3.4.1), a subgiant observed by *Kepler*. The basic stellar parameters of KIC 5689820 are $T_{\rm eff} = 5037 \pm 76$ K, $\log g = 3.76 \pm 0.06$ dex, $[\mathrm{Fe/H}] = 0.21 \pm 0.15$ dex (Li et al., 2020), suggesting it is analogous to δ Eri. As such, its oscillation properties are likely to be comparable to our simulation results.

3.2.2 Three-dimensional stellar atmosphere models

In this section, we briefly describe the 3D hydrodynamical model atmospheres constructed for the target stars. All 3D models are computed with a customized version of the Stagger code (Nordlund & Galsgaard, 1995; Collet et al., 2018), a radiative-magnetohydrodynamics code that solves the equations of mass, momentum, and energy conservation, as well as the magnetic-field induction equation on 3D Eulerian meshes. All scalars are evaluated at cell centres while vectors are staggered at the cell faces. The radiative heating rate in the equation of energy conservation is obtained by solving the 3D equation of radiative transfer along a set of inclined rays in space, assuming LTE. In total, nine directions – one vertical direction and eight inclined directions representing combinations of two polar and four azimuthal angles – are included for all models presented in this work. The code is equipped with realistic microphysics: it uses a modified version of the Mihalas et al. (1988) equation of state (Trampedach et al., 2013) that accounts for all ionization stages of the 17 most abundant elements in the Sun as well as the Hydrogen molecule. A comprehensive collection of relevant continuous absorption and scattering is included (Hayek et al., 2010). Line opacities are taken from the MARCS model atmosphere package (Gustafsson et al., 2008) and treated with the opacity binning method (Nordlund, 1982; Magic et al., 2013a), with 12 opacity bins divided based on both wavelength and strength of opacity.

Our Stagger model stellar atmosphere simulates a small part of the star near the photosphere, assuming a constant gravitational acceleration and ignoring magnetic field. Geometrically, the simulation domain is discretized on a cuboid box. The horizontal size of the box is required to be large enough to enclose at least ten granules at any time in the simulation (Magic et al., 2013a). Vertically, the 3D simulation covers roughly the outer 1% of the star by radius, where hydrodynamical and 3D effects are most prominent. Because the vertical (radial) scale of the simulation is very small compared to the total stellar radius, the spherical effect in simulation domain is negligible. Boundaries are periodic in the horizontal direction while open in the vertical (Collet et al., 2018). The default bottom boundary condition is that outgoing flows (vertical velocities towards stellar centre) are free to carry their entropy fluctuations out of the simulation domain, whereas incoming flows (vertical velocities towards stellar surface) must have invariant entropy and thermal (gas plus radiation) pressure. The 3D model[3] for each star is constructed based on the reference

[3]When stating "3D simulations/models" or "normal simulations/models", we always mean the simulation carried out with the default boundary condition in the Stagger code.

Table 3.3: Basic information about the set-up of 3D simulations for KIC 6225718, Procyon, β Hydri and δ Eri. "Sampling interval" refers to the time interval between two consecutive simulation snapshots. As mesh points are not uniformly distributed vertically, both minimum and maximum vertical grid spacing are provided.

Model configuration	KIC 6225718		Procyon		β Hydri		δ Eri	
	Normal	Artificial driving	Normal	Artificial driving	Normal	Artificial driving	Normal	Artificial driving
Resolution	240^3	$120^2 \times 125$	240^3	$120^2 \times 125$	240^3	$120^2 \times 125$	240^3	240^3
Time duration $\mathcal{T}_{\rm tot}$ [hour]	30.0	9.0	43.5	29.0	58.3	17.5	77.5	31.0
$\mathcal{T}_{\rm tot}/t_{\rm gran,eff}$ †	261	78	207	138	255	77	206	82
Sampling interval [s]	36	36	87	87	70	70	93	93
Vertical size [Mm]	5.9	5.9	17.5	17.5	11.6	11.6	14.4	14.4
Vertical grid spacing [km]	15–51	31–103	31–244	63–489	29–93	57–185	43–109	43–109
Horizontal grid spacing [km]	53	106	126	251	110	221	142	142

†: The granulation timescale $t_{\rm gran,eff}$ is the e-folding time of a granule. It is estimated from the empirical relation $t_{\rm gran,eff} = 2 \times 10^6 g^{-0.85}(T_{\rm eff}/5777)^{-0.4}$ ($T_{\rm eff}$ and g in cgs unit) which is calibrated from a wide variety of stars observed by *Kepler*. See Kallinger et al. (2014) for more detail.

$T_{\rm eff}$ and $\log g$ values given in Table 3.1, and their basic properties are summarised in Table 3.3. All models adopt the Asplund et al. (2009) solar abundance, as all our targets are solar-metallicity stars. The spatial resolution of our models is 240^3, with 240×240 mesh points evenly distributed in the horizontal plane. In the vertical direction, mesh points are not uniformly distributed. The highest numerical resolution is applied around the photosphere (Magic et al. 2013a Fig. 2) in order to resolve the transition from the optically thick to the optically thin regions adequately, with at least 15 mesh points per pressure scale height around the photosphere in all 3D models. The adopted spatial resolution should be sufficient to study the mode excitation problem, as differences between excitation rates computed from $253 \times 253 \times 163$ and $125 \times 125 \times 82$ solar simulations are small, according to Samadi et al. (2007). The duration of the simulation is long enough to cover at least 200 times the granulation timescale. The mean effective temperature over the entire simulation timespan for each 3D model is close to the reference value.

In addition, as mentioned in Nordlund & Stein (1998) and Zhou et al. (2019), it is non-trivial to extract reliable damping rates from 3D simulations. To overcome this difficulty, we conduct numerical experiments that artificially drive radial oscillation at a particular frequency to large amplitude by modifying the bottom boundary condition. The artificial driving simulation enables reliable calculation of damping rate at the driving frequency. For each star, we carried out such experiments at various driving frequencies in order to obtain damping rates as a function of frequency. For the purpose of controlling variables, all artificial driving experiments for a given star share the same input options with driving frequency being the only difference, and their numerical resolution and time sequence are also identical. Note that in the case of δ Eri, we adopt the standard 240^3 resolution, whereas for the three other stars, we reduce the numerical resolution to $120^2 \times 125$ (120 by 120 cells in the horizontal plane with 125 points along vertical direction). The underlying reasons and validation for lowering the resolution are discussed in Appendix 3.6.2, where we also detail numerical techniques about the artificial mode driving simulation, including tests and validation of our method.

3.2.3 One-dimensional stellar interior models

The 1D interior models for the target stars are computed using the Modules for Experiments in Stellar Astrophysics (MESA version 10000, Paxton et al. 2011, 2013, 2015). For all calculations, we adopt the Asplund et al. (2009) metal mixture. Equation of state tables are generated from the FreeEOS[4] code (Irwin, 2012), which takes into account 20 elements (Hydrogen, Helium and 18 metals) and all of their ionization stages in its calculations. At low temperatures ($\log T < 4.5$), continuous and line opacities at each wavelength are calculated from BLUE, an opacity package that adopts up-to-date atomic data (developed primarily for detailed non-LTE radiative transfer calculations, see Amarsi et al. 2016b for description of the code). These are then reduced to Rosseland mean opacities for use in MESA. Opacities at high temper-

[4] http://freeeos.sourceforge.net/

Table 3.4: Summary of fitting targets and free parameters in stellar interior models.

Input free parameters	Targets to fit
Stellar mass M	Effective temperature $T_{\rm eff}$
Initial Metallicity $[\mathrm{Fe/H}]_{\rm init}$	Surface gravity $\log g$
Initial Helium mass fraction $Y_{\rm init}$	Metallicity [Fe/H]
Mixing length parameter multiplier f_α	Averaged 3D temperature at matching point $\langle \bar{T}_{\rm 3D}(r_{\rm am}) \rangle_t$
Convective turbulence multiplier β	Averaged 3D turbulent pressure at matching point $\langle \bar{P}_{\rm turb,3D}(r_{\rm am}) \rangle_t$
Convective overshoot parameter $f_{\rm ov}$	

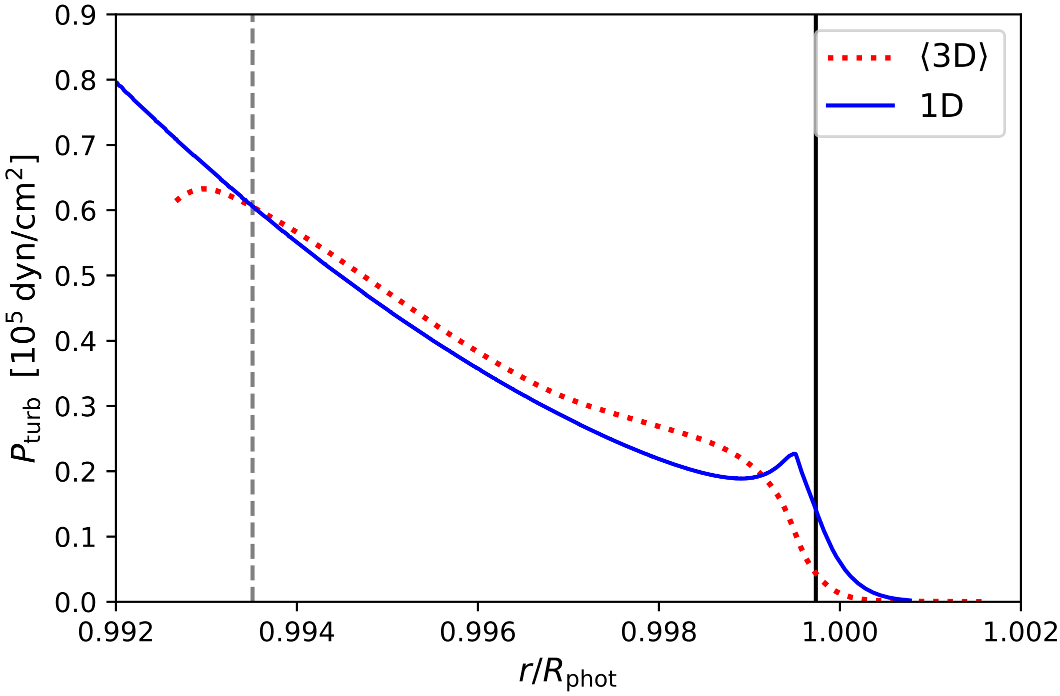

Figure 3.1: Predicted distribution of turbulent pressure in the near-surface region of δ Eri models. The blue solid line represents 1D "turbulent pressure" calculated from MESA with modifications introduced in Sect. 3.2.3 while the red dotted line is horizontal- and time-averaged turbulent pressure from 3D atmosphere model of δ Eri. Grey dashed vertical line indicates the location of the matching point, and black solid vertical line marks the upper convection boundary $r_{\rm edge}$ in the MESA model. $R_{\rm phot}$ is the stellar radius.

atures ($\log T > 4.4$) are taken from the OPAL tables (Iglesias & Rogers, 1996). The two sets of opacities are blended in the temperature interval $4.4 < \log T < 4.5$. Nuclear reaction rates are from JINA REACLIB (Cyburt et al., 2010) plus additional tabulated weak reaction rates (Fuller et al., 1985; Oda et al., 1994; Langanke & Martínez-Pinedo, 2000), which is the default setting in MESA. Element diffusion and gravitational settling are treated following the default method in MESA (see Paxton et al. 2011 Sect. 5.4). However, for stars more massive than $\approx 1.4 M_{\odot}$, considering element diffusion and gravitational settling alone will result in near or complete depletion of helium and heavy elements at the stellar surface in some stages of their evolution (see e.g., Fig. 1 of Verma & Silva Aguirre 2019), which contradicts measured abundances of F-type stars in open clusters (Varenne & Monier, 1999). To counter the effects of element diffusion and gravitational settling below the surface convection zone, we include turbulent diffusion in our calculations. The turbulent diffusion coefficient is computed according to Dotter et al. (2017) for every time-step during the evolution calculations.

In MESA, thermal (gas plus radiation) pressure P_{ther} and temperature T at the outermost cell (surface) are required for the outer boundary conditions (Paxton et al. 2011 Sect. 5.3). Here, we place the outer boundary of the MESA models above the photosphere (the Rosseland mean optical depth at surface $\tau_{\text{surf}} \approx 5 \times 10^{-3}$). Instead of integrating the Eddington grey atmosphere and using the Eddington $T - \tau$ relation to obtain pressure and temperature at the outer boundary, we opt for P_{ther} and T derived from 3D simulations. Specifically, the $P_{\text{ther}} - \tau$ and $T - \tau$ relations are computed from the STAGGER-grid (Magic et al., 2013a) that spans a wide range of stellar parameters. For each STAGGER-grid model, we extract $P_{\text{ther}} - \tau$ relation by horizontally and temporally averaging the 3D thermal pressure and (Rosseland mean) optical depth. Temperature stratifications are calculated following the method developed in Trampedach et al. (2014a), which gives the predicted $T - \tau$ relation when all heat is transported by radiation. Following the aforementioned procedure, we obtain $P_{\text{ther}} - \tau$ and $T - \tau$ relations at various $\{T_{\text{eff}}, \log g, \text{[Fe/H]}\}$ combinations. The results are then tabulated and applied in the evolutionary simulation: At every iteration during the model's evolution, the $P_{\text{ther}} - \tau$ and $T - \tau$ relations corresponding to the current stellar parameters are computed by interpolation. Surface pressure and temperature are subsequently evaluated at the given τ_{surf}.

MESA adopts the diffusion approximation for radiative transfer, which is valid in the stellar interior but is not a satisfactory approximation when $\tau \lesssim 10$ (Trampedach et al., 2014a). As the outer boundary of our stellar model is located above the photosphere, we correct the radiative temperature gradient (down to $\tau = 10$) to obtain a more realistic temperature structure in the atmosphere portion of the MESA model. The corrected radiative temperature gradient reads (Trampedach et al., 2014a; Mosumgaard et al., 2018):

$$\nabla_{\text{rad}} = \nabla_{\text{rad,MESA}} \left[\frac{dq(\tau)}{d\tau} + 1 \right], \tag{3.1}$$

with q as the Hopf function:

$$q(\tau) = \frac{4}{3}\left[\frac{T(\tau)}{T_{\rm eff}}\right]^4 - \tau. \tag{3.2}$$

The term $\nabla_{\rm rad,MESA}$ is the original MESA radiative temperature gradient computed based on the diffusion approximation, and $T(\tau)$ represents the $T-\tau$ relation when all heat is transported by radiation.

Convection is treated using the Henyey et al. (1965) formulation of the MLT. We do not treat the mixing length parameter $\alpha_{\rm MLT}$ as a constant throughout the star's evolution, but rather as a varying quantity which depends on effective temperature, surface gravity and metallicity (see also Mosumgaard et al. 2018 Eq. 2):

$$\alpha_{\rm MLT}\left(T_{\rm eff}, \log g, [{\rm Fe/H}]\right) = f_\alpha \alpha_{\rm MLT,3D}\left(T_{\rm eff}, \log g, [{\rm Fe/H}]\right). \tag{3.3}$$

Here $\alpha_{\rm MLT,3D}$ is the mixing length parameter calibrated from the STAGGER-grid (value taken from Magic et al. 2015), interpolated to current $T_{\rm eff}$, $\log g$ and [Fe/H]. By including the free parameter f_α, the mixing length parameter multiplier, we ensure that the relative value of $\alpha_{\rm MLT}$ in MESA is consistent with the results calibrated from the STAGGER-grid, but allow its absolute value to differ in order to account for the different equations of state and opacities between the STAGGER-code and MESA. In other words, we retain the variation of $\alpha_{\rm MLT}$ across the HR diagram as indicated by 3D surface convection simulations but with an absolute value consistent with the solar calibration using the aforementioned equations of state and opacities.

Further, we include the "turbulent pressure" term, which is typically ignored in 1D hydrostatic models in stellar evolution calculations (see Trampedach et al. 2014b and Jørgensen & Weiss 2019 for efforts in this direction). The 1D "turbulent pressure" is constructed based on the convective velocity $v_{\rm conv}$ from MLT:

$$P_{\rm turb,1D}(r) = \beta\rho(r)v_{\rm conv}^2(r), \tag{3.4}$$

where r denotes radius, ρ is mass density. The convective turbulence multiplier β is a free parameter to be specified before the evolutionary calculations. The value of β is determined by requiring that the "turbulent pressure" in MESA and the horizontal- and time-averaged 3D turbulent pressure are identical at the matching point (detailed below). However, $v_{\rm conv}$ predicted from MLT will rapidly decrease to zero when approaching the convection boundary, which causes a sudden drop of $P_{\rm turb,1D}$ (see e.g., Fig. 3 of Trampedach et al. 2014b) and therefore an unrealistically large turbulent pressure gradient. In order to overcome this problem, we consider the influence of convective overshoot on $v_{\rm conv}$. Overshoot becomes relevant at a location near the convection boundary in the convection zone and extends the convective velocity beyond the top convection boundary (the overshoot region) where an exponential decay of v_{conv} is assumed (Paxton et al. 2011 Eq. 2),

$$v_{\mathrm{conv}}(r) = v_{\mathrm{conv}}(r_0) \exp\left[-\frac{2|r-r_0|}{f_{\mathrm{ov}} H_P(r_{\mathrm{edge}})}\right]. \tag{3.5}$$

Here, r_0 is the location where overshoot starts to take effect, and r_{edge} is the corresponding radius of upper convection boundary. $H_P(r_{\mathrm{edge}})$ is the pressure scale height at upper convection boundary, and f_{ov} is called overshoot parameter. We calibrate f_{ov} at the upper boundary of the surface convection zone using the horizontal- and time-averaged 3D turbulent pressure from the Stagger-grid[5]. As demonstrated in Fig. 3.1, the inclusion of convective overshoot and a suitable value of the overshoot parameter (at the top of surface convection zone) ensure a gradual change of $P_{\mathrm{turb,1D}}$ near the convection boundary, thus bringing the 1D "turbulent pressure" profile into better agreement with the averaged turbulent pressure predicted from 3D simulations.

We carried out evolutionary calculations from the pre-main-sequence to the age at which target stellar parameters are satisfied assuming the aforementioned input physics. To obtain a reliable stellar interior model, we minimize the difference between model parameters and corresponding constraints by iteratively adjusting the free parameters in mesa. Basic stellar parameters of our best-fitting models are presented in Table 3.1 for the four target stars. Input free parameters and constraints are listed in Table 3.4. The parameters $\langle \bar{T}_{\mathrm{3D}}(r_{\mathrm{am}})\rangle_t$ and $\langle \bar{P}_{\mathrm{turb,3D}}(r_{\mathrm{am}})\rangle_t$ (the bar symbol and $\langle ... \rangle_t$ represent the horizontal average and temporal average, respectively) are two extra constraints from the 3D models, where r_{am} symbolizes the location of matching point in the 3D model. The matching point in mesa, r_{im}, is determined by requiring identical thermal pressures between the 1D and averaged 3D models,

$$P_{\mathrm{ther,1D}}(r_{\mathrm{im}}) = \langle \bar{P}_{\mathrm{ther,3D}}(r_{\mathrm{am}})\rangle_t. \tag{3.6}$$

Fitting the averaged 3D temperature and turbulent pressure not only tightly restricts f_α and β, but it is also necessary for smooth transitions (for temperature and total pressure) from the interior model to the atmosphere model. This is essential for the patching procedure described in the subsequent section.

3.2.4 Oscillation frequencies from patched models

We combine the horizontally and temporally averaged 3D models and 1D interior models to patched 1D models for a more precise calculation of the oscillation properties (i.e. eigenfrequencies, eigenfunctions, mode masses etc.). The fitting method introduced in Sect. 3.2.3 ensures continuous transitions in temperature and total pressure between r_{am} and r_{im}, hence make patching straightforward in practice: The averaged 3D model and best 1D model for the same star are trimmed by discarding all layers below the atmosphere matching point in the averaged 3D model, and all layers above the interior matching point in the 1D model. They are then conjoined to

[5] At all other convection boundaries, such as the bottom boundary of surface convection zone, f_{ov} is still a free parameter.

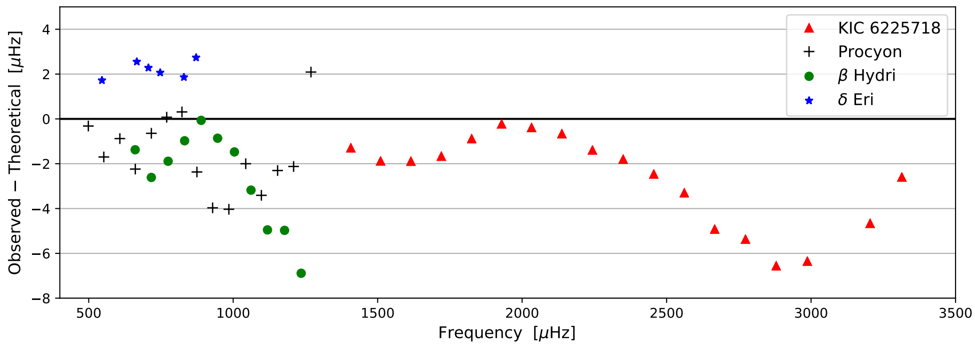

Figure 3.2: Frequency differences between observations and theoretical results computed with patched 3D + 1D models. Only radial ($l = 0$) modes are compared here. Observational data for KIC 6225718, Procyon, β Hydri and δ Eri are from Lund et al. (2017), Bedding et al. (2010, table 4), Bedding et al. (2007) and E. Bellinger (private communication), respectively.

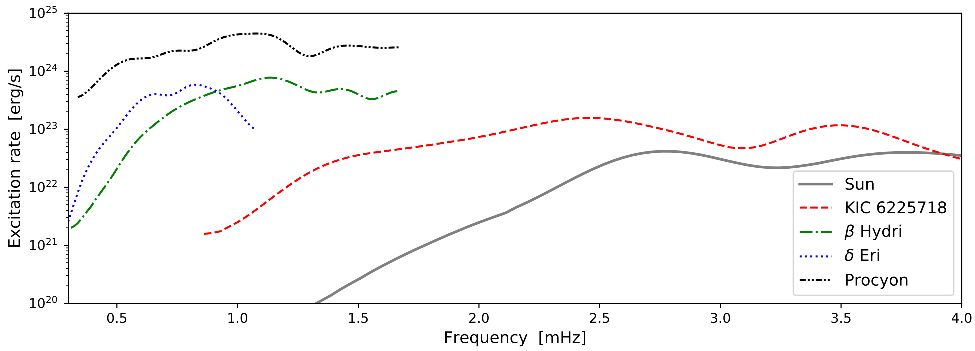

Figure 3.3: Excitation rates as a function of cyclic frequency for our target stars computed via Eq. (3.7). Theoretical excitation rate of the Sun (see Fig. 6 of Zhou et al. 2019) is also shown for comparison. The curves are smoothed from the original simulation data with Gaussian kernels whose FWHM are 0.47, 0.39, 0.16, 0.16, 0.11 mHz for the Sun, KIC 6225718, Procyon, β Hydri, δ Eri, respectively.

obtain the patched 1D model that ranges from the stellar centre to the upper atmosphere ($\tau \sim 10^{-6}$). Pulsation calculations are performed with the Aarhus adiabatic oscillation package (ADIPLS, Christensen-Dalsgaard 2008) using the patched model as input. Theoretical radial mode frequencies are compared with measured values for all stars investigated, and reasonable agreement is found between the two in each case as demonstrated in Fig. 3.2. The agreement in individual (radial) mode frequencies, in conjunction with the fact that $T_{\rm eff}$, $\log g$ and [Fe/H] of 1D model are close to the observationally inferred values, indicates that our patched models realistically describes the structure of target stars.

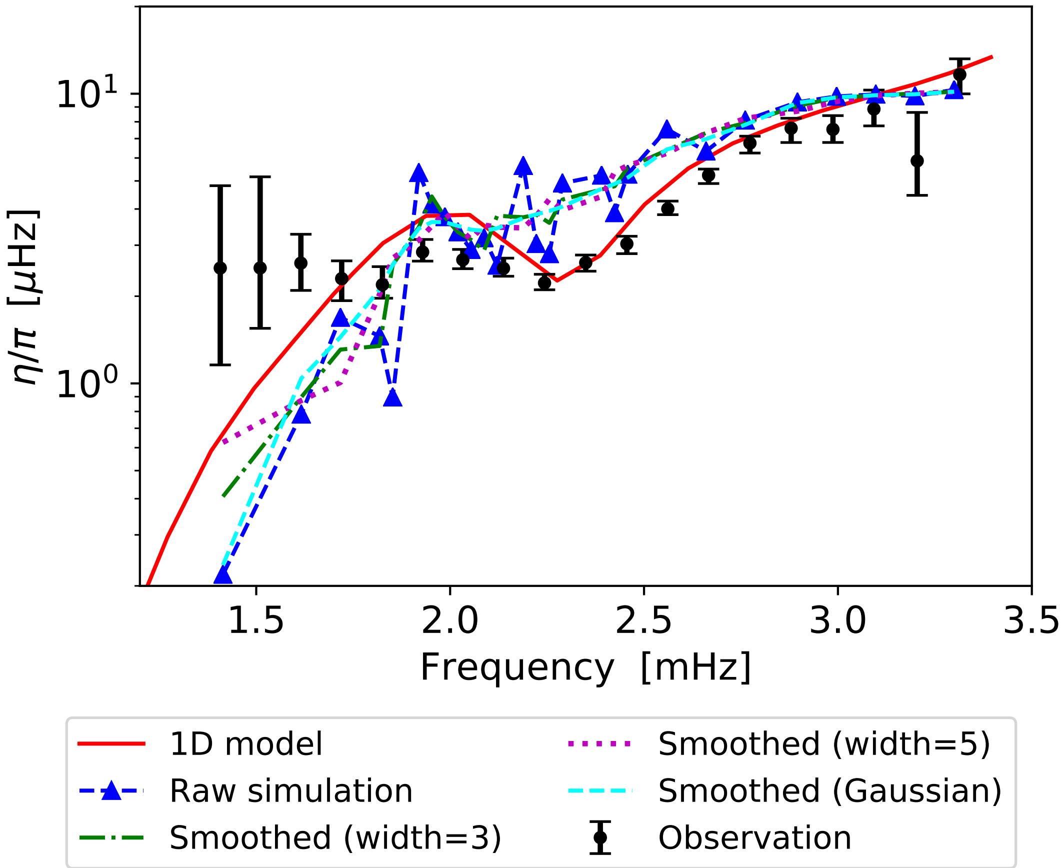

Figure 3.4: Theoretical damping rates for KIC 6225718 computed based on Eq. (3.9). Simulation results (raw data are blue triangles, smoothed data are green dashed-dotted, magenta dotted, and cyan dashed lines) are divided by π to compare with observed $l = 0$ mode line width (black dots with errorbars representing uncertainty) from Lund et al. (2017). The green and magenta curves are obtained by taking the running mean of the raw simulation data with a width of three and five data points, respectively, whereas the cyan dashed line results from smoothing the raw simulation data by a Gaussian kernel with an FWHM equal to 0.18 mHz. The red solid line represents η/π for this star computed from 1D non-local, time-dependent convection model (Houdek et al., 2019).

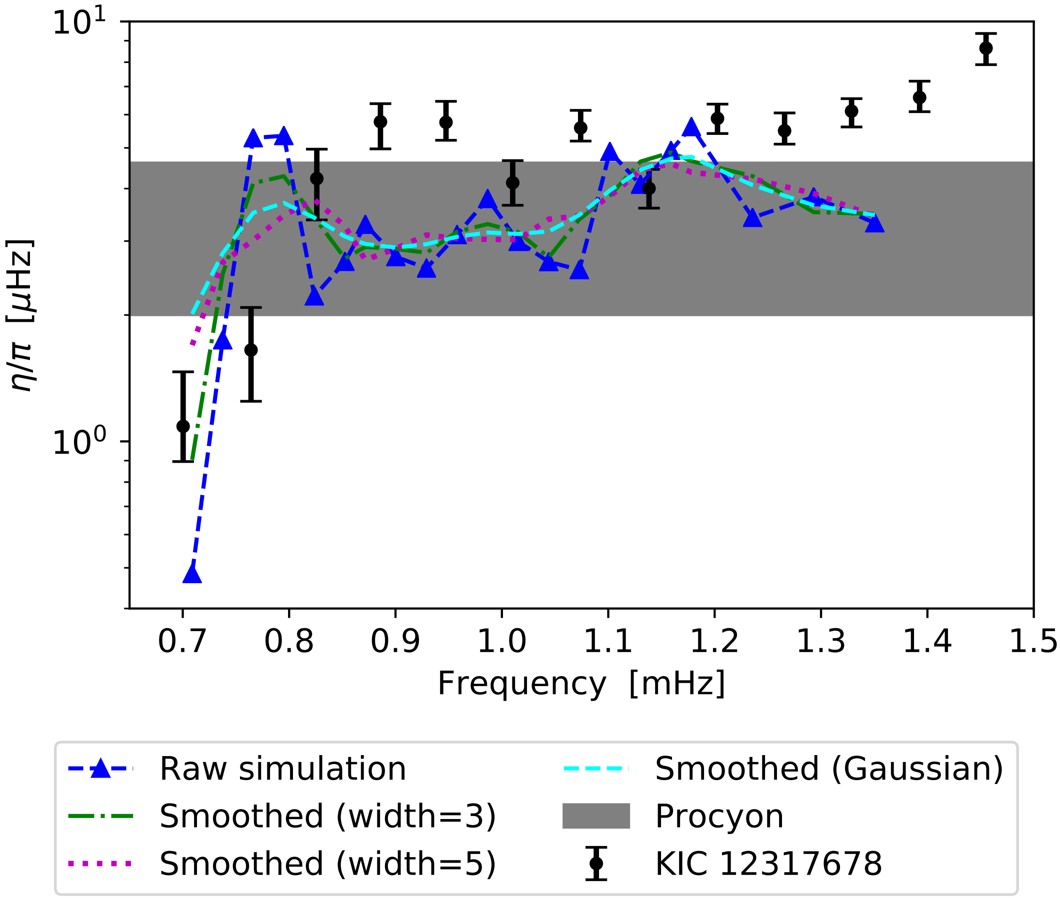

Figure 3.5: Theoretical damping rates for Procyon. The cyan dashed line is smoothed from raw simulation data by a Gaussian kernel with an FWHM equal to 0.1 mHz. The grey-shaded band is the measured mean line width (with uncertainty) converted from the mean mode lifetime provided in Bedding et al. (2010). Black dots and errorbars are radial mode line width of star KIC 12317678 measured by Lund et al. (2017). The fundamental parameters of KIC 12317678 are close to Procyon therefore it is shown for comparison as well.

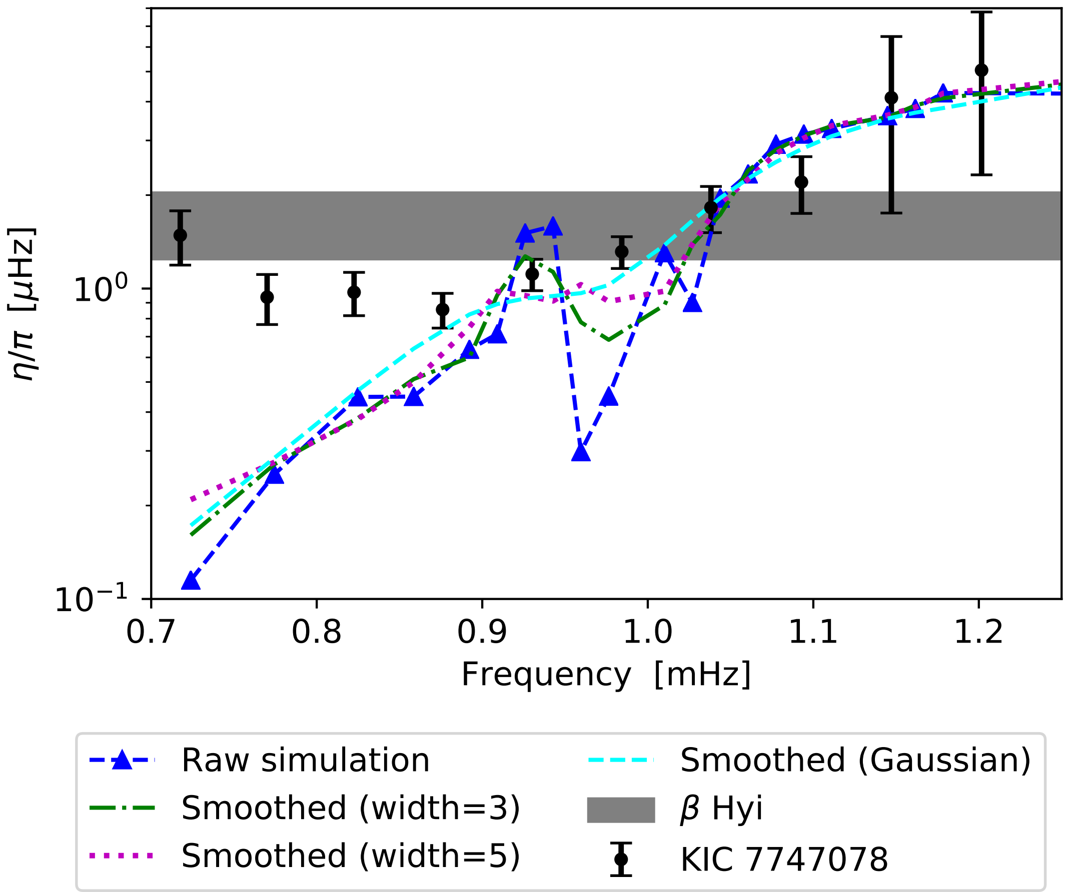

Figure 3.6: Theoretical damping rates for β Hydri. The cyan dashed line is smoothed from raw simulation data using a Gaussian kernel with an FWHM equal to 0.1 mHz. Mean line width for β Hydri is from Bedding et al. (2007), and KIC 7747078 is a subgiant whose basic parameters are close to β Hydri (line width from Li et al. 2020).

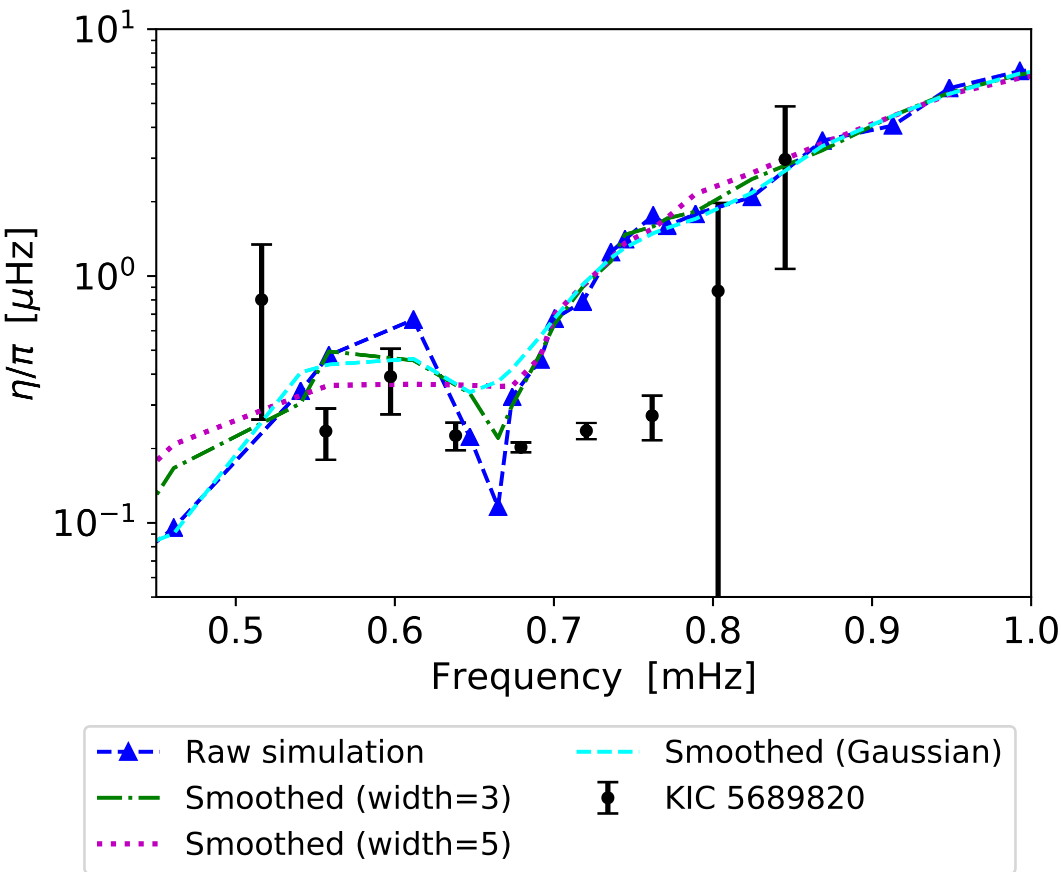

Figure 3.7: Predicted damping rates for δ Eri are compared with measured line width of KIC 5689820 (Li et al., 2020), a star that has similar stellar parameters as δ Eri. The cyan dashed line is smoothed from raw simulation data using a Gaussian kernel with an FWHM equal to 0.07 mHz.

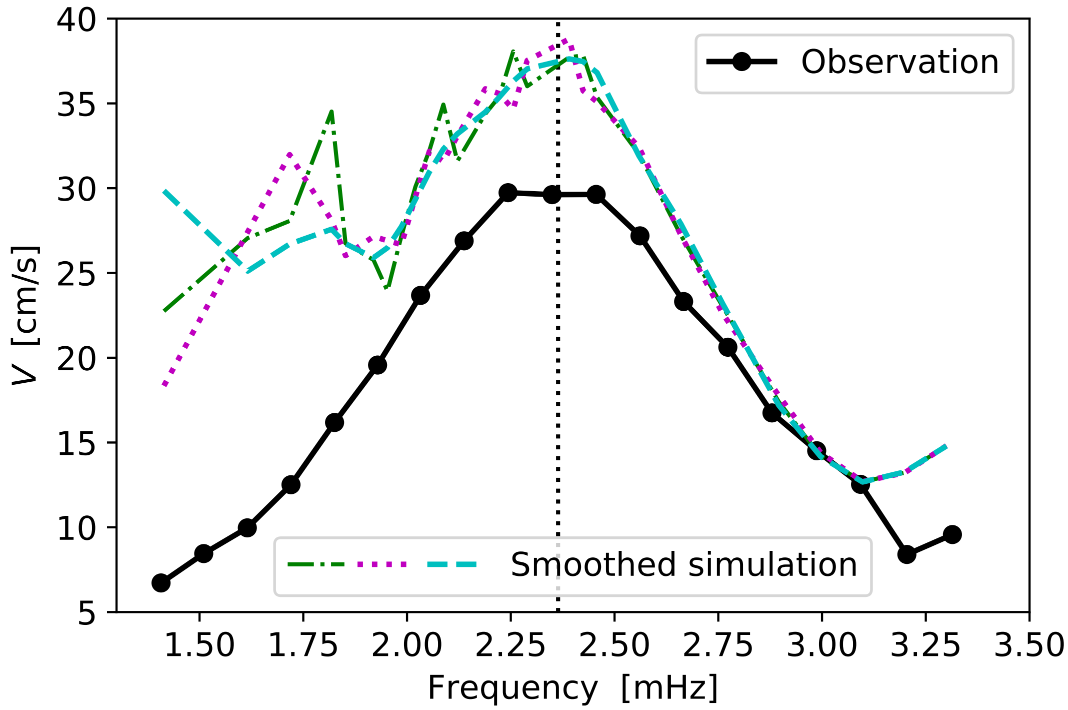

Figure 3.8: Predicted photosphere velocity amplitude for KIC 6225718, as evaluated using Eq. (3.10). The green dashed-dotted, magenta dotted, and cyan dashed lines represent theoretical results from different smoothing options for damping rates (see Fig. 3.4). Black dots represent the estimated velocity amplitude for the same star converted from the observed flux variations (Lund et al., 2017) using the empirical relation in Kjeldsen & Bedding (1995). The black vertical dotted line marks the observed $\nu_{\max}$.

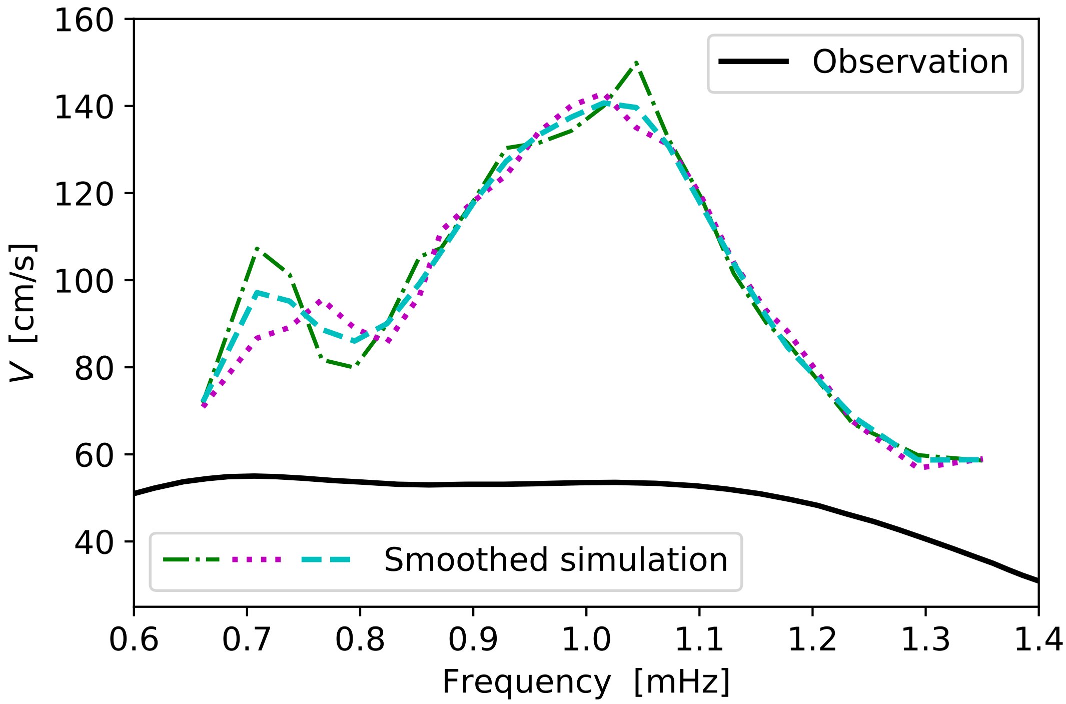

Figure 3.9: Similar to Fig. 3.8, but photosphere velocity amplitude for Procyon. The smoothed mean radial velocity, measured by Arentoft et al. (2008, black solid line), has been divided by the projection factor 0.712 in order to convert to kinematic velocity amplitude.

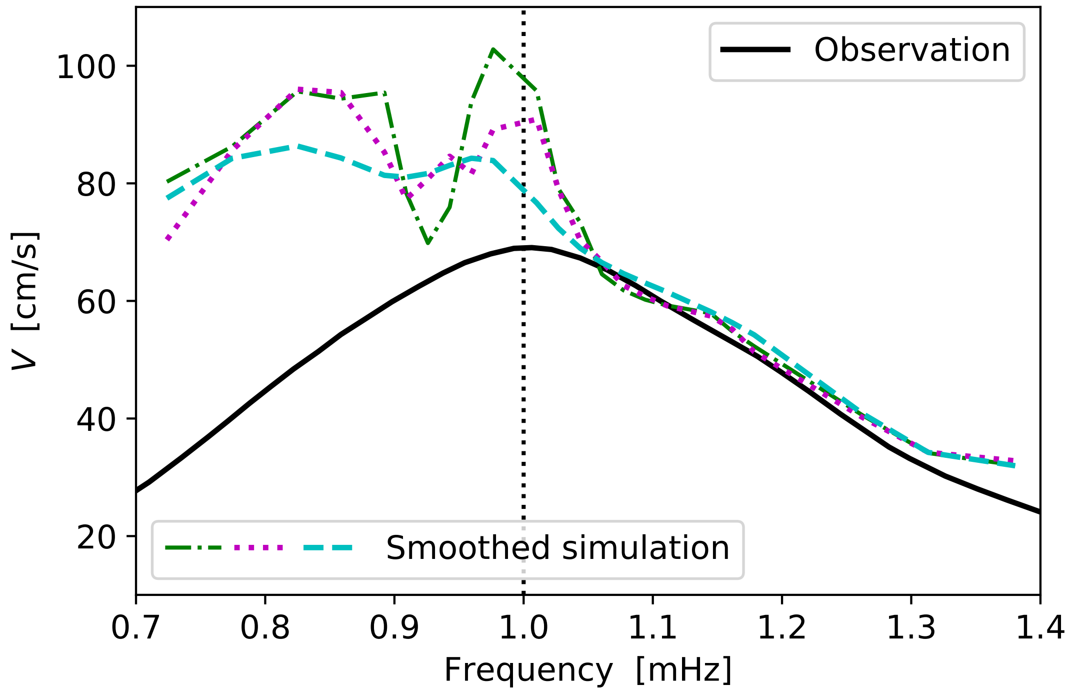

Figure 3.10: Predicted photosphere velocity amplitude for β Hydri is compared with measured mean radial velocity by Bedding et al. (2007).

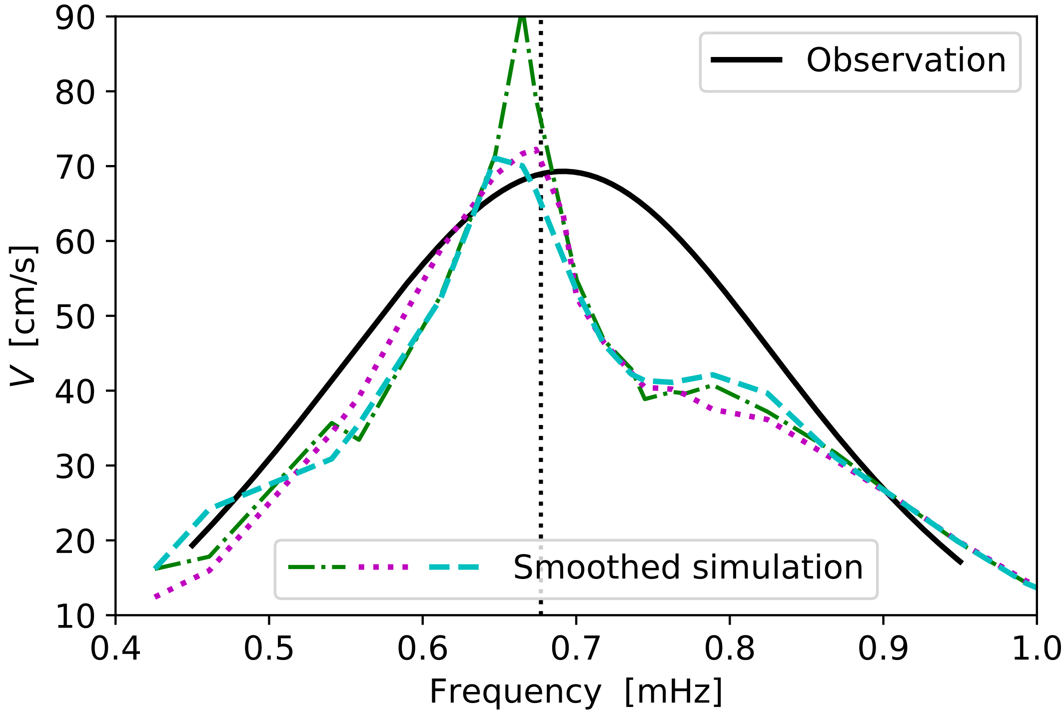

Figure 3.11: Similar to Fig. 3.10 but for δ Eri. Mean radial velocity (black solid line) is measured by SONG and data provided by E. Bellinger and T. Arentoft.

3.3 Mode excitation, damping and amplitude

Solar-like oscillations are p-modes driven by near-surface convection: fluctuations of thermodynamic quantities and turbulence caused by convection stochastically excite normal modes of the star to finite amplitude. Meanwhile, solar-like oscillations are dissipated by the same mechanisms that excite them (Houdek & Dupret, 2015). The final mean oscillation amplitude results from the balance between energy injection (excitation) rate and energy dissipation (damping) rate. In this section, we quantify both the excitation and damping rate of radial oscillations for our target stars from the theoretical angle. Mode excitation and damping rates are computed from 3D atmosphere and 1D patched models, which then allows an estimation of mode amplitude and $\nu_{\max}$.

Excitation rates are calculated based on Eq. 16 of Zhou et al. (2019)[6],

$$\begin{aligned}\mathcal{P}_{\rm exc}(\omega) = &\frac{\omega^2 A_{\rm box}}{8\mathcal{T}_{\rm tot}E_0}\left[\left(\int_{r_{\rm 3D\,bot}}^{r_{\rm surf}} \frac{\partial \xi_r}{\partial r}\mathfrak{Re}\left\{\mathcal{F}[\delta \bar{P}_{\rm nad}]\right\}\,dr\right)^2\right.\\ &\left.+\left(\int_{r_{\rm 3D\,bot}}^{r_{\rm surf}} \frac{\partial \xi_r}{\partial r}\mathfrak{Im}\left\{\mathcal{F}[\delta \bar{P}_{\rm nad}]\right\}\,dr\right)^2\right],\end{aligned} \tag{3.7}$$

where $\mathcal{F}$ represents the Fourier transform from time to frequency domain. The terms ω, $A_{\rm box}$ and $\mathcal{T}_{\rm tot}$ stand for angular frequency, horizontal area of 3D simulation, and total time duration of 3D simulation, respectively. The term E_0 represents mode kinetic energy per unit surface area (Nordlund & Stein 2001 Eq. 63; Zhou et al. 2019 Eq. 17):

$$E_0 = \frac{\omega^2}{2}\int_0^{r_{\rm surf}} \rho\xi_r^2(r)\left(\frac{r}{R_{\rm phot}}\right)^2 dr, \tag{3.8}$$

which is constant at given frequency. Here ξ_r is the radial amplitude function (also called mode eigenfunction). It is calculated from 1D patched model using ADIPLS. Its gradient, $\partial_r\xi_r$, represents the local compression of the fluid due to oscillations. $\delta\bar{P}_{\rm nad}$ is the horizontally averaged non-adiabatic pressure fluctuation, which includes all non-adiabatic effects such as entropy fluctuation and turbulence (Reynolds stress) caused by convection (Nordlund & Stein, 2001). The time-dependent non-adiabatic pressure fluctuation is computed from the 3D simulation, then transferred to frequency space for the evaluation of excitation rate $\mathcal{P}_{\rm exc}$. Eq. (3.7) is integrated from the bottom of simulation domain $r_{\rm 3D\,bot}$ to the uppermost point of the patched model $r_{\rm surf}$, as $\delta\bar{P}_{\rm nad}$ is accessible in practice only through the 3D simulation. Eq. (3.7) implies that mode excitation results from the coupling between oscillations and convection. Excitation rates as a function of frequency are shown in Fig. 3.3 for the four target stars. We refer the reader to Nordlund & Stein (2001), Stein & Nordlund (2001) and Zhou et al. (2019) for detailed derivation of Eq. (3.7) and explanations about how components of this equation are computed numerically.

The dissipation of oscillation energy is quantified by the damping rate η, which

[6] $\mathfrak{Re}\{f\}$ ($\mathfrak{Im}\{f\}$) means the real (imaginary) part of complex function f.

describes how fast an oscillation mode looses its kinetic energy by a factor of e if there is no external energy supply. Damping processes broaden the power spectrum of the mode, shaping it to a Lorentzian profile centred at the eigenfrequency of the mode. The width of the Lorentzian envelope (line width Γ), an observable in asteroseismology, is connected to the damping rate by $\Gamma = \eta/\pi$ if the observational time series is much longer than the mode lifetime (Chaplin et al., 2005). Throughout the paper, we confine our discussions to linear damping rates, which are derived assuming non-adiabatic effects can be treated as first-order perturbation to adiabatic oscillations. Nonlinear interactions are not likely to contribute significantly to the damping of radial modes for stars investigated in this work, according to the results from Kumar et al. (1994). The expression of (linear) damping rate for radial oscillations is:

$$\eta = \frac{\omega \int_{y_{\rm bot}}^{y_{\rm top}} \mathfrak{Im}\left\{(\delta\bar{\rho}^*/\bar{\rho}_0)\delta\bar{P}_{\rm nad}\right\} dy}{4m_{\rm mode}|\mathcal{V}(R_{\rm phot})|^2} \tag{3.9}$$

(see Appendix 3.6.1 for derivation). Here, the asterisk represents the complex conjugate, and $m_{\rm mode}$ and $\mathcal{V}$ are mode mass per unit surface area and vertical velocity amplitude, respectively. The denominator is proportional to the kinetic energy of the mode. The integral in the numerator is the work integral, which is proportional to the energy loss rate of the mode. In practice, this is evaluated from the bottom ($y_{\rm bot}$) to the top ($y_{\rm top}$) of the simulation domain along the vertical (y) direction, because outside the 3D simulation domain $\delta P_{\rm nad}$ is unobtainable. The value of the work integral is determined by the magnitude of density fluctuation $\delta\rho$ and the non-adiabatic pressure fluctuation, as well as the phase difference between them; further detail about how components of Eq. (3.9) are computed can be found in Appendix 3.6.2. Theoretical damping rates, both raw simulation data and smoothed results, are divided by π in order to compare directly with measured radial mode line widths, as depicted in Figs. 3.4-3.7 for the four target stars. In all cases, the Gaussian kernel used to smooth the raw simulation data has an FWHM $\approx 1.75\Delta\nu$. We note that only mean line width (converted from the mean mode lifetime $t_{\rm mode} = \eta^{-1}$ derived in Bedding et al. 2010) is available for Procyon. In order to facilitate more detailed comparison, we also include frequency-dependent line width data of KIC 12317678 from the *Kepler* LEGACY sample (Lund et al., 2017) in Fig. 3.5. The basic parameters of KIC 12317678 are $T_{\rm eff} = 6580 \pm 77$ K, $\log g = 4.048^{+0.009}_{-0.008}$ dex, [Fe/H] $= -0.28 \pm 0.1$ dex (Lund et al., 2017), suggesting that this star is similar to Procyon so it is likely to be comparable to our simulation results. The situation for β Hydri is similar: individual mode line widths are currently not available. Therefore, we also show the observed frequency-dependent line widths of a *Kepler* subgiant with similar fundamental stellar parameters (KIC 7747078, $T_{\rm eff} = 5903 \pm 74$ K, $\log g = 3.90 \pm 0.01$ dex, [Fe/H] $= -0.22 \pm 0.15$ dex; stellar parameters, mode frequencies and line width data provided by Yaguang Li, private communication) for comparison. For δ Eri, currently no line width information is available and therefore we compare our theoretical results with radial mode line widths of the similar star KIC 5689820.

The balance between stochastic excitation and mode damping dictates the final mean amplitude of the mode. With the excitation and damping rate both quantified, the mean kinematic velocity amplitude at the photosphere due to one oscillation mode can be evaluated via

$$V = \sqrt{\frac{2\mathcal{P}_{\text{exc}}}{M_{\text{mode}}\eta}} \tag{3.10}$$

(Zhou et al. 2019 Eq. 25), where M_{mode} is mode mass defined in Aerts et al. (2010) Eq. 3.140 (not to be confused with mode mass per unit area m_{mode}). The excitation and damping rates used in Eq. (3.10) come from smoothed, rather than raw, simulation data in order to mitigate the effects of random fluctuations found in the latter and make the theoretical V more comparable with observations (note that the published observed radial velocity power spectra have already been smoothed to ensure the extracted oscillation amplitudes are independent of the stochastic effects of the mode excitation and damping). The thus computed kinematic velocity amplitudes for KIC 6225718, Procyon, β Hydri and δ Eri are shown in Figs. 3.8-3.11, respectively.

However, what is obtained from the spectroscopic measurements of stellar oscillations is not V directly, but the mean radial velocity $\mathfrak{v}$, whose physical source is kinematic velocity but which is also impacted by limb darkening and other geometric effects. The relation between radial and kinematic velocity is quantified by the projection factor, which depends on the mode quantum number and the wavelength at which the spectral line is measured. Bedding et al. (1996) and Kjeldsen et al. (2008) have calculated the projection factor for radial oscillations, measured at 550 nm wavelength, to be 0.712. We adopt this value for all stars included in this work, i.e. $\mathfrak{v} = 0.712V$, to make comparison between simulation and observation possible. Meanwhile, we note that for KIC 6225718, stellar oscillations are identified by measuring brightness changes using photometry. In this scenario, the asteroseismic observable is the flux variation representing the change in surface temperature induced by oscillations. In view of this, we convert the observed flux variation to radial velocity using the empirical relationship proposed by Kjeldsen & Bedding (1995, their Eq. 5), then divide the estimated radial velocity by 0.712 to compare directly with our simulation results.

3.4 Discussion

Our results presented in Sect. 3.3 not only provide insights into the physical processes responsible for the driving and damping of radial oscillations for individual stars, but also allow comparison among different types of stars. In Sect. 3.4.1, we compare the theoretical damping rates and velocity amplitudes with observation and estimate theoretical $\nu_{\max}$ for our sample stars. We then discuss the connection between mode excitation/damping and global properties of stars (Sect. 3.4.2), and explore how radial oscillations are damped in the near-surface region of the star based on simulation results (Sect. 3.4.3).

3.4.1 Does 3D surface convection simulations agree with observation?

The theoretical damping rates for KIC 6225718 agree with observational data in general, as shown in Fig. 3.4. The observed damping rates demonstrate a dip around 2.2 mHz, which is also predicted in the simulation results, albeit at slightly lower frequencies. However, below 1.9 mHz, we systematically underestimate the damping rates, with the discrepancy becoming larger toward lower frequencies. This misalignment is associated with the limited vertical size of the 3D simulation. As also pointed out in Zhou et al. (2019), because the work integral is truncated at the bottom of the simulation box, contributions from deeper layers are omitted. This has greater influence on the low-frequency radial modes, as they have more substantial oscillation amplitudes in the deep stellar interior than high-frequency ones. We demonstrate this effect explicitly in Sect. 3.6.2.2. According to Eq. (3.10), the magnitude of the damping rates has a direct impact on the velocity amplitudes. For KIC 6225718, good agreement between theoretical and observationally inferred velocity amplitudes is achieved above 2 mHz, as seen from Fig. 3.8. However, below 2 mHz, we over-predict the velocity amplitude, which is a consequence of underestimating the damping rates in this frequency range. The errors below 2 mHz prevent us from obtaining a clear bell-shape $V - \nu$ curve that resembles observation. Nevertheless, the synthesized velocity amplitudes clearly show a local peak located between 2.25 and 2.45 mHz, which enables an estimate for theoretical $\nu_{\rm max}$. We are aware that the exact value of theoretical $\nu_{\rm max}$ is somewhat ambiguous because it depends on how the raw simulation data is smoothed. To this end, only an estimated theoretical $\nu_{\rm max}$ value is provided. In the case of KIC 6225718, $\nu_{\rm max}$ obtained from 3D simulations is in the vicinity of 2.3 mHz which is consistent with the measured value $\nu_{\rm max,obs} = 2.364$ mHz.

For Procyon, theoretical damping rates are compared with observation in Fig. 3.5. Between 0.75 mHz and 1.4 mHz, our results fall nicely in the uncertainty range of observationally inferred mean damping rate, indicating a general consistency between modelling and observation. Meanwhile, damping rates predicted from the 3D simulations demonstrate two noticeable features that differ from the other three stars investigated in this work. First, above 0.8 mHz, η is nearly constant with frequency. Second, the depression of η in a certain frequency range, which is a common characteristic of solar-like oscillations, is not recognizable for Procyon. These features are likely to be physically real rather than caused by numerical errors because a similar trend is also seen for the measured damping rates of KIC 12317678, whose basic stellar parameters are close to those of Procyon. The underlying reason for the absence of the depression in η will be investigated in Sect. 3.4.3. The predicted velocity amplitudes, however, are systematically higher than the observed values, especially between 0.9 mHz and 1.1 mHz, where V is overestimated by a factor of 2 (Fig. 3.9). Since the damping rates are consistent with observation overall, this disagreement stems from the excitation rate which is likely to be over-predicted. The reason for this will be investigated further in future work.

In the case of β Hydri, encouraging agreement between the modelled and measured mean damping rate are attained, as shown in Fig. 3.6. The simulations predict a dip in η located between 0.95 mHz and 1 mHz, which is reasonable as the depression of the damping rate commonly appears near $\nu_{\max}$ of the star. Comparing with the frequency-dependent damping rates of the similar subgiant KIC 7747078, we find that our predictions resemble observations at high frequencies ($\nu \gtrsim 1$ mHz) but are underestimated in the low-frequency regime ($\nu \lesssim 0.9$ mHz). The underlying reason is the same as in the case of KIC 6225718: limited vertical coverage of 3D simulation truncates the work integral. The errors on η at low frequencies then propagate into the theoretical velocity amplitude, resulting in higher values than what are measured from observation (Fig. 3.10). Nevertheless, it is still possible to make an estimation of theoretical $\nu_{\max}$ from the local peak of V near 1 mHz. We conclude that $\nu_{\max}$ of β Hydri predicted from numerical simulations resides in the neighbourhood of 0.98 mHz, which conform with observation.

For δ Eri, the calculated damping rates agree reasonably well with observations (note that here theoretical η are compared with observations from a similar star, rather than δ Eri itself). The predicted dip is located at 0.65 mHz, which is consistent with the observed dip. The main discrepancy between simulation and observation takes place between 0.7 mHz and 0.8 mHz, where theoretical results are larger than measured values for reasons that are not entirely clear. In this case, the discrepancy is likely not due to the time duration or limited vertical scale of the artificial driving simulations, because we have verified that (1) doubling the simulation timespan does not affect the damping rate result noticeably, and (2) the contribution from the deep layers of the simulation to the work integral is small (especially for $\nu \gtrsim 0.7$ mHz artificial driving simulations), implying that the vertical size of simulation is sufficient for modelling mode damping in this frequency range. Turning to velocity amplitude, our theoretical results generally agree with observations both in magnitude and in the shape of the $V - \nu$ curve. The predicted $\nu_{\max}$, which is estimated to be around 0.65 mHz, also matches the observed $\nu_{\max}$ (0.677 mHz) for δ Eri.

When comparing simulation results with observations, one should keep in mind that magnetic fields, which are ubiquitous in stars but not included in our simulations, do interact with acoustic oscillations. Helioseismic analysis of low degree p-modes over the solar cycle (Chaplin et al., 2000) has demonstrated that mode excitation is not sensitive to magnetic fields. Damping rates (line widths) however, increase with increasing magnetic activity[7]. The net effect is that with increasing solar activity, the amplitude of solar p-modes decreases. The suppression of oscillation amplitude due to magnetic activity has also been confirmed in other solar-like oscillating stars (Bonanno et al., 2019). With this in mind, and noting that the signature of stellar activity was found in Procyon (Huber et al., 2011a), it is worth discussing the potential influence of magnetic fields on our results. For the Sun, Chaplin et al. (2000) measured a $\approx 25\%$ increase in damping rates from solar activity minimum to maximum. Assuming the influence of stellar activity on damping rates and mode

[7] A crude explanation is that granules become smaller as magnetic field strength increases (see Nordlund et al. 2009 and references therein). The decreased granule size gives rise to larger damping rates near $\nu_{\max}$, according to the calculation by Houdek et al. (2001).

amplitudes in Procyon is qualitatively the same as the solar case, the presence of magnetic fields will results in slightly larger damping rates, and thus slightly smaller V compared to predictions from our simulations.

Although disagreements and uncertainties exist, the comparison between oscillation properties obtained from simulations against observations shows great promise. In all cases, encouraging agreement between the two is achieved. Without introducing any tunable parameter in our calculations, the computed damping rates and velocity amplitudes are of the same order of magnitude as the corresponding measured values, and in most cases, the $\eta - \nu$ and $V - \nu$ relations also resemble observation. Theoretical $\nu_{\rm max}$ values estimated from our simulations are consistent overall with the corresponding measurements. These indicate that our numerical approach for modelling the excitation, damping and amplitude of radial oscillations is applicable not only to the Sun (demonstrated in Zhou et al. 2019) but also to other solar-type oscillators.

3.4.2 What is the relationship between excitation/damping rate and fundamental stellar parameters?

We are now in a position to study the relationship between mode excitation/damping and fundamental parameters of these stars. We emphasize that our sample size is too small to establish a quantitative relation, but we can discuss the qualitative behaviour.

The trend in excitation rate is similar for all stars investigated: mode excitation is weak at low frequencies, then increases with frequency to a plateau that contains $\nu_{\rm max}$ before slightly declining at higher frequencies. The underlying reason is explained in, for example, Stein & Nordlund (2001) and Zhou et al. (2019). In brief, at low frequencies, relatively weak local compression caused by the low-frequency mode limits the excitation rate (i.e. small $\partial_r \xi_r$ in Eq. (3.7)). At high frequencies, on the contrary, mode excitation is limited by convection because non-adiabatic pressure fluctuation decreases with increasing frequency (i.e. small $\delta P_{\rm nad}$ in Eq. (3.7)).

We note that excitation rate is overall greater in hotter (higher $T_{\rm eff}$) stars, which is clearly observed by comparing the Sun and KIC 6225718, or β Hydri and Procyon, as their surface gravities are similar. The correlation between $\mathcal{P}_{\rm exc}$ and $T_{\rm eff}$ can be understood by considering the heat transport near the photosphere: Stronger radiative cooling and larger convective flux near photosphere are required to transport more energy in hotter stars (Stein et al., 2004). Larger radiative and convective fluxes then give rise to greater entropy fluctuation and stronger velocity field, which directly results in more energy supply from convection to oscillations via the stochastic excitation mechanism. The relation between $\mathcal{P}_{\rm exc}$ and global stellar parameters has been empirically quantified by Samadi et al. (2007), who suggested that excitation rate should scale with the luminosity-mass ratio (essentially the same as $T_{\rm eff}^4/g$),

$$\mathcal{P}_{\rm exc,max} \propto (L/M)^s, \tag{3.11}$$

where $\mathcal{P}_{\rm exc,max}$ is the maximum excitation rate of the star and s is a slope to be fixed

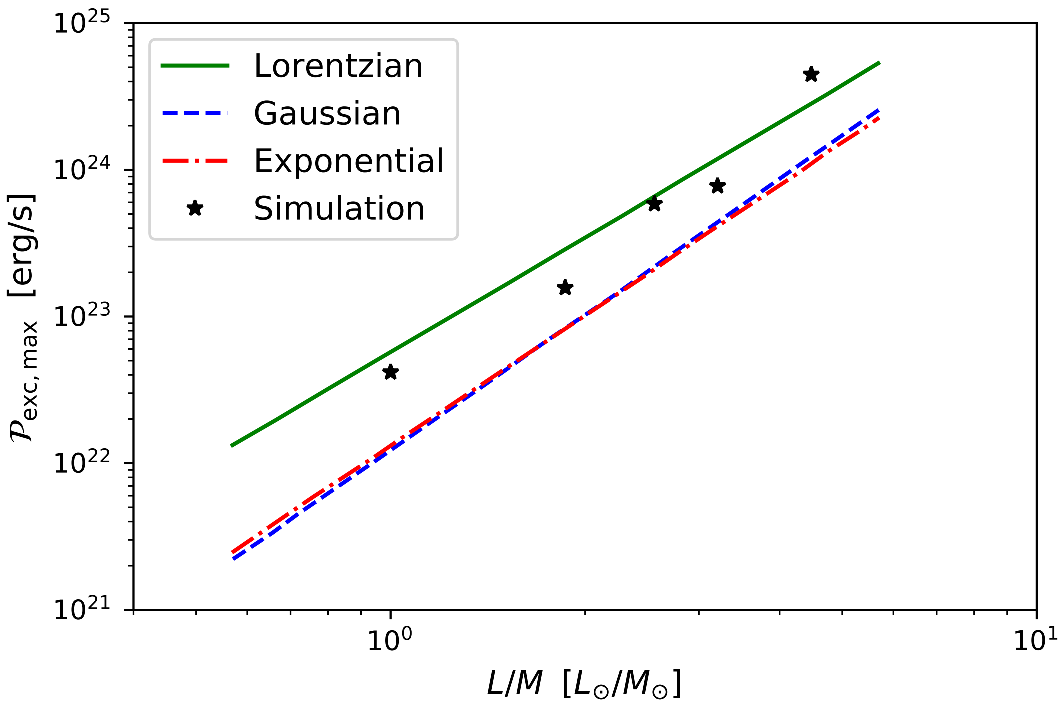

Figure 3.12: The relationship between maximum excitation rate and luminosity-mass ratio of the star is shown. Solid, dashed and dashed-dotted lines are relations derived in Samadi et al. (2007, their Fig. 6), with label "Lorentzian", "Gaussian" and "Exponential" represent different analytical models for turbulence in their calculations (detailed in Samadi et al. 2007 and references therein). Black star symbols are results from our simulations, where $\mathcal{P}_{\rm exc,max}$ are evaluated by taking the maximum value of the smoothed excitation rates (not the raw simulation data in order to avoid strong fluctuations) and L/M are obtained from MESA models.

by fitting to numerical results. The linear relation between $\log \mathcal{P}_{\rm exc,max}$ and $\log(L/M)$ obtained in Samadi et al. (2007) from their semi-analytical calculations of excitation rates for difference stars, together with results from our 3D simulations, are demonstrated in Fig. 3.12. Our numerical results obey this scaling law, indicating excitation rates evaluated in this work are consistent with Samadi et al. (2007), although our method is radically different from theirs.

Damping rates are believed to depend on global stellar parameters as well. The scaling relation for damping rates was first proposed by Chaplin et al. (2009). Based on observational data and their pulsation calculations, they suggested damping rates near $\nu_{\rm max}$ should be proportional to the fourth power of the effective temperature. The positive correlation between η near $\nu_{\rm max}$ and $T_{\rm eff}$ was subsequently confirmed by Appourchaux et al. (2012) and Vrard et al. (2018) for main-sequence, subgiant and red giants observed by *Kepler*. Owing to the limited sample size and errors on theoretical damping rates near $\nu_{\rm max}$, we do not attempt to present a quantitative relation between η and $T_{\rm eff}$. Nonetheless, by comparing two cooler stars (δ Eri and β Hydri, Figs. 3.7 and 3.6) with the two hotter stars (KIC 6225718 and Procyon, Figs. 3.4 and 3.5), it is obvious that damping rates (near $\nu_{\rm max}$) predicted from simulations increase with effective temperature of the star, which qualitatively agrees with observations.

The magnitude of the damping rate is determined in part by the work integral, and thus the density and non-adiabatic pressure fluctuations (Eq. (3.9)). As demonstrated in Magic et al. (2013b, their Figs. 2 and 3), fluctuations in thermodynamic quantities are stronger in hotter stars because of the relatively larger convective velocity field. Their findings offers insights into the positive correlation between η and $T_{\rm eff}$: in hotter stars, stronger fluctuations in density and pressure result in larger damping rates[8]. It is worth noting that both excitation and damping rates are positively correlated with effective temperature, which is not surprising because solar-like oscillations are excited and damped by the same physical process: turbulent convection (Houdek & Dupret, 2015; Zhou et al., 2019). Therefore, their relationship with global stellar parameters should be similar.

We now proceed to the relation between $\nu_{\rm max}$ and fundamental stellar parameters, one of the most important scaling relations in asteroseismology. As first suggested by Brown et al. (1991) and Kjeldsen & Bedding (1995), $\nu_{\rm max}$ of a solar-like oscillating star should scale with its surface gravity and effective temperature, $\nu_{\rm max} \propto g/\sqrt{T_{\rm eff}}$. By scaling from the solar values, the thus evaluated $\nu_{\rm max}$ are 2.26 mHz for KIC 6225718, 1.07 mHz for β Hydri and 0.70 mHz for δ Eri, which broadly agree with our theoretical results. Given that theoretical $\nu_{\rm max}$ are estimated from *ab initio* hydrodynamical simulations – an approach completely independent of the $\nu_{\rm max}$ scaling relation – we claim the overall validity of the $\nu_{\rm max}$ scaling relation is supported at solar-metallicity from a theoretical angle.

In this work, we have successfully derived the relationship between excitation

[8]We are aware that the explanation provided here might not cover the whole picture of the $\eta - T_{\rm eff}$ relation, because damping rate is not only affected by the strength of fluctuations in density and pressure but also by the phase difference between them, and the mode kinetic energy also plays a role (see Eq. (3.9)).

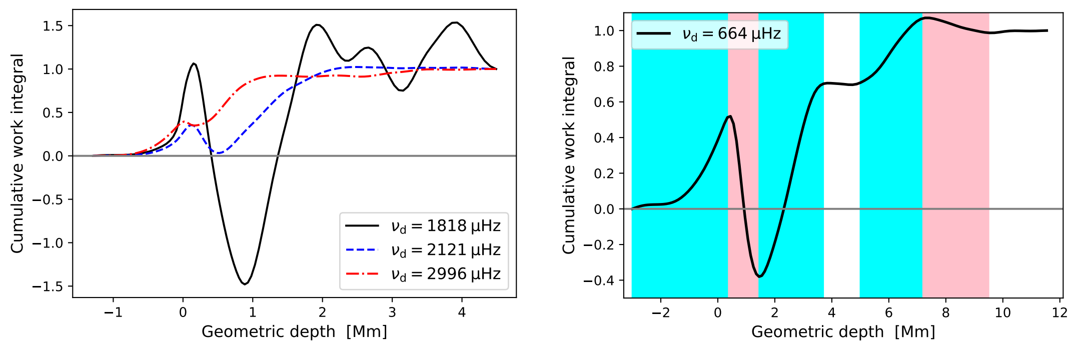

(a)

(b)

Figure 3.13: 3.13(a): Normalized cumulative work integral distributions within the simulation domain for three example simulation modes, computed from artificial driving experiments for KIC 6225718 with driving frequency ν_d equals to 1818 μHz (low-frequency), 2121 μHz (intermediate-frequency) and 2996 μHz (high-frequency), respectively. Here, the work integral is integrated from the top (left side of the figure) to the bottom of the simulation domain and normalized by its total value, therefore at the top the cumulative work integral is 0 while at bottom it is always 1. Zero geometric depth corresponds approximately to the photosphere. 3.13(b): Similar to 3.13(a), but illustrating the damping and growth region of a simulation mode computed from an artificial driving experiment for δ Eri. Noticeable damping and growth areas are shaded in cyan and pink, respectively.

and damping rates and fundamental stellar parameters from a purely theoretical perspective: Excitation and damping rates near $\nu_{\max}$ of the star are both positively correlated with the effective temperature, consistent with previous theoretical investigations and empirical findings for solar-type oscillating stars. In addition, theoretical $\nu_{\max}$ estimated from simulations scales with $g/\sqrt{T_{\rm eff}}$, confirming qualitatively the $\nu_{\max}$ scaling relation at solar-metallicity. These findings suggest that our numerical approach for modelling the excitation and damping of radial modes is valid across a wide range of effective temperatures and surface gravities. With more detailed numerical simulations that cover additional $\{T_{\rm eff}, \log g, [{\rm Fe/H}]\}$ combinations, especially including red giant branch stars, which are important in Galactic archaeology (e.g. Casagrande et al. 2016) but have not yet been studied with 3D models, it should be possible to quantify the relationship between $\mathcal{P}_{\rm exc}$, η and fundamental stellar parameters and even to quantify the departure (if any) from the widely-used $\nu_{\max}$ scaling relation from 3D surface convection simulations.

3.4.3 What is the underlying physics of mode damping?

Apart from quantifying the value of the damping rates at different frequencies, it is also worthwhile to understand the physics behind mode damping, an important topic that is difficult to probe by observation. In this section, we will explore two relevant questions based on the simulation results: (1) Which part of the star con-

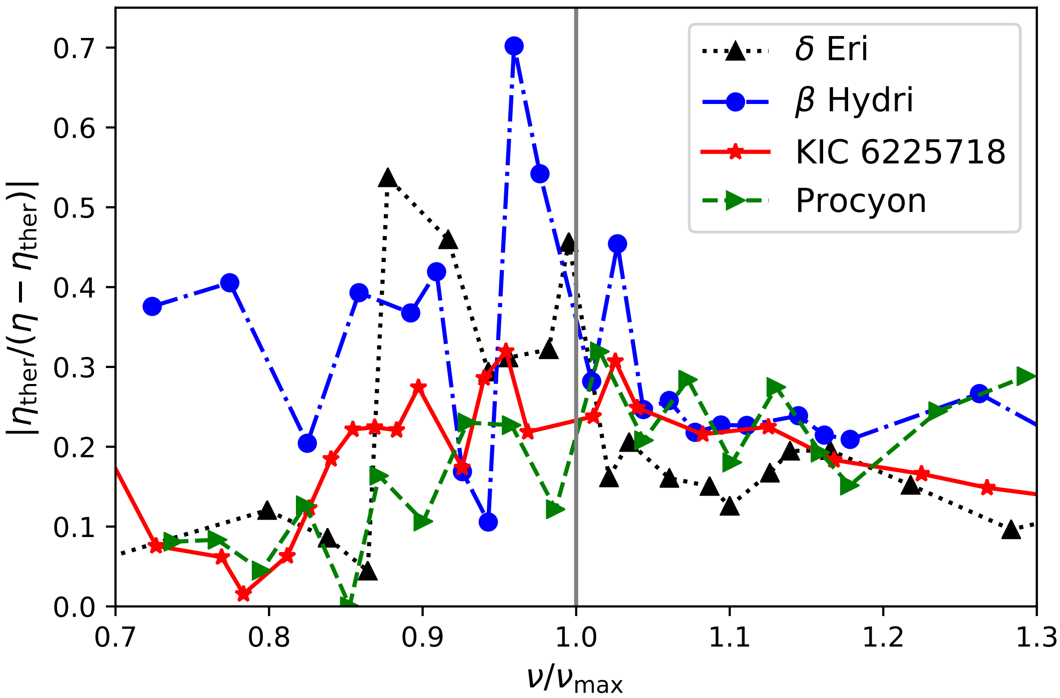

Figure 3.14: The ratio between $\eta_{\rm ther}$ and $\eta - \eta_{\rm ther}$ at different frequencies for all four target stars. Frequencies are normalized by the measured $\nu_{\rm max}$ of the corresponding star (see table 3.2, note that for Procyon frequencies are normalized by 1 mHz because the value of $\nu_{\rm max}$ is uncertain for this star). All data presented here are computed from artificial driving simulations without any smoothing.

tributes most to mode damping, and hence dictates the final value of η? (2) The dip in damping rate near $\nu_{\max}$ is a common feature in the $\eta - \nu$ curve, but why is it less pronounced in warm turn-off stars like Procyon?

To answer question (1), we show in Fig. 3.13 the cumulative work integral distribution in the entire simulation domain, which reflects contributions to damping from different locations in the atmosphere and upper convection zone. Increasing work integral (with geometric depth) means positive work is done by the mode at the corresponding location, suggesting the mode is damped there. Conversely, decreasing work integral means negative work, indicating that the mode is growing locally. Fig. 3.13(b) clearly demonstrates several damping and growth regions for an example simulation mode, and the relative strength between damping and growth determines the stability of this mode. Although modes (in the same star) with different frequencies are damped and driven in different regions, they have some features in common. As observed from Fig. 3.13(a), all three modes shown are damped in the stellar atmosphere (negative geometric depth). Moving inward, there is a growth region just below the photosphere where temperature stratification is highly superadiabatic (see e.g. Fig. 25 in Magic et al. 2013a), implying tight connection between mode energy gain/loss and over-adiabaticity. Intermediate- and high-frequency modes are mostly damped in deeper layers, and their cumulative work integral becomes nearly flat when approaching the bottom of simulation domain. The latter indicates that the vertical size of the simulation box is sufficient for modelling damping processes for these two modes. The low-frequency mode, however, demonstrates broader regions of damping and growth, in agreement with Balmforth (1992a) for low-frequency p-modes in the Sun. The fact that discernable regions of damping and growth are present down to the bottom of the simulation domain also suggests that extra contributions to the damping of the low-frequency modes from the deep interior are omitted because of the limited vertical size of simulation, as discussed in Sect. 3.4.1.

Regarding question (2), Procyon is not an anomalous case showing an "odd" $\eta - \nu$ relation, but rather a typical representation of warm stars. Both observation (Appourchaux et al., 2014) and theoretical investigation (Houdek et al., 2019) have confirmed that the dip in η near $\nu_{\max}$ becomes less obvious with increasing T_{eff}, and above ~ 6300 K it is hardly seen (demonstrated in Fig. 3 of Appourchaux et al. 2014 and Figs. A1-A3 of Houdek et al. 2019). Therefore, a more appropriate question may be: why does the dip in η disappear in warm ($T_{\mathrm{eff}} \gtrsim 6300$ K) stars? To answer this, one should first understand the physical origin of the damping rate dip, which is explained in Balmforth (1992a) for the solar case. In short, at frequencies where the damping rate dip occurs, destabilizing effects from the thermal pressure fluctuations largely cancel the stabilizing effects from convective turbulence, leaving a relatively small η compared to lower or higher frequencies, where the cancellation is relatively less severe. Here, we show the relative importance of thermal processes (radiative and convective heat transport) and turbulence to mode damping by displaying $|\eta_{\mathrm{ther}}/(\eta - \eta_{\mathrm{ther}})|$ in Fig. 3.14 for four stars investigated in this work, where η_{ther} represents contributions to damping rates from thermal pressure fluctuations while $\eta - \eta_{\mathrm{ther}}$ mainly reflects damping due to turbulent pressure. Larger $|\eta_{\mathrm{ther}}/(\eta - \eta_{\mathrm{ther}})|$

thus signifies that thermal processes have a greater impact on the total damping rate. As illustrated in Fig. 3.14 for Procyon and KIC 6225718, $|\eta_{\rm ther}/(\eta - \eta_{\rm ther})|$ near $\nu_{\rm max}$ is typically less than 0.3, whereas in the other two cooler stars, it is ~ 0.5 near $\nu_{\rm max}$. Although our sample is not large enough to draw a definite conclusion, it is very likely that thermal processes are less influential in mode damping for warm stars. As thermal processes are responsible for destabilizing modes with frequency near $\nu_{\rm max}$, relatively large (relative to the contribution from turbulence) negative $\eta_{\rm ther}$ will hence depress η near $\nu_{\rm max}$, which is the situation of δ Eri and β Hydri. In warm stars, however, thermal processes are not significant enough to leave noticeable fingerprints on the $\eta - \nu$ curve, which is dominated by contributions from the convective motion.

In addition, we clarify the connection between the mixing length parameter $\alpha_{\rm MLT}$ and the damping rate dip, which is discussed in Balmforth (1992a) and Appourchaux et al. (2014). Balmforth (1992a) has shown that the damping rate dip predicted for the Sun becomes less pronounced with increasing $\alpha_{\rm MLT}$. On the other hand, $\alpha_{\rm MLT}$ calibrated from 3D convection simulations decreases with increasing $T_{\rm eff}$ (Ludwig et al., 1999; Trampedach et al., 2014b; Magic et al., 2015). Given that the damping rate dip becomes less obvious with increasing $T_{\rm eff}$, both observationally and from our simulations, at first glance it seems these two conclusions contradict each other. However, both conclusions can in fact be valid. In the Sun, for example, increasing $\alpha_{\rm MLT}$ results in more efficient convective heat transfer. That is, an equal amount of heat can be carried in a region with less over-adiabaticity, causing the superadiabatic temperature gradient to become smaller near the surface (Joyce & Chaboyer, 2018). Consequently, the destabilizing effects from thermal processes decrease. The larger velocity field with increasing $\alpha_{\rm MLT}$ strengthens the contribution from convective turbulence to mode damping. These two factors together make thermal processes less significant, thus translating to a less pronounced damping rate dip when assuming larger $\alpha_{\rm MLT}$. Comparing stars with different $T_{\rm eff}$, we see that in warmer stars, the superadiabatic temperature gradient is larger near the photosphere, as predicted from 3D simulations (Magic et al., 2013a). Therefore, the calibrated $\alpha_{\rm MLT}$ is smaller and thermal processes are stronger. Nevertheless, the velocity field and convective turbulence are also much stronger in warmer stars and the contribution from convective turbulence to mode damping increases with $T_{\rm eff}$ as well. As discussed above, it is the relative importance between thermal processes and convective turbulence that determines the shape of the $\eta - \nu$ curve. Since thermal processes are relatively less influential in hot stars, the dip in η is less recognizable, which does not conflict with a comparatively small $\alpha_{\rm MLT}$.

3.5 Conclusions

In this work, we quantified the excitation and damping rates of radial p-modes based on detailed modelling of both the atmospheres and interiors of four key benchmark stars exhibiting solar-like oscillations. We adopted the theoretical framework of Nordlund & Stein (2001), Stein & Nordlund (2001) and Zhou et al. (2019) for the evaluation of mode excitation rates. For all target stars, components of the expression of excitation rate are computed directly from the corresponding 3D model atmosphere and patched 1D stellar structural model. The expression of linear damping rate was derived from the first-order perturbation theory where non-adiabatic effects are treated as small perturbations to adiabatic oscillations. In order to extract reliable damping rates from 3D simulations using analytical formula (3.9), it is necessary to separate the density fluctuation $\delta\rho$ caused by pulsation from "convective noise." To this end, we carried out artificial mode driving simulations where a target radial oscillation is artificially driven to large amplitude so that $\delta\rho$ at the driving frequency results predominantly from pulsation. Theoretical damping rates at each frequency are computed from such numerical experiments and compared in detail with observed frequency-dependent line widths. Encouraging agreement is achieved between simulations and observation: For all four stars investigated, our numerical damping rates are of the same order of magnitude as the corresponding measured values, and in most cases the $\eta - \nu$ relation matches observation. This validates our numerical approach for calculating the damping rate for radial modes.

Based on the excitation and damping rates, we calculated the velocity amplitudes from which theoretical $\nu_{\max}$ values are estimated. Our results are compared against the corresponding observations. In particular, the estimated $\nu_{\max}$ is consistent overall with measured values. This finding foreshadows exciting opportunities for predicting this important asteroseismic observable for solar-type oscillators from first principles using 3D hydrodynamical simulations.

Studying several stars also allows for comparison between excitation/damping rates and fundamental stellar parameters. Qualitative relationships between $\mathcal{P}_{\rm exc}$, η, $\nu_{\max}$ and $T_{\rm eff}$, g were found from our simulations. Namely, both excitation and damping rates are positively correlated with the effective temperature, which accords with empirical relations derived from other theoretical investigations (Samadi et al., 2007) and those summarised from observations (Chaplin et al., 2009). Meanwhile, theoretical $\nu_{\max}$ values estimated from our simulations broadly obey the $\nu_{\max}$ scaling relation, reaffirming it at solar-metallicity.

These facts, in combination with the results for the Sun (Zhou et al., 2019), suggest that our method of modelling the excitation and damping of solar-like radial mode oscillations is valid across a wide range of effective temperatures and surface gravities, especially given that there are no tunable free parameters in our formulations used to "fit" the theoretical results to observational data. In addition, our method enables deeper understanding of the underlying physics behind mode excitation and damping. The former was discussed in detail in Zhou et al. (2019). In this work, we explored where exactly radial oscillations are damped in the near-surface region based on the artificial mode driving simulations and concluded that intermediate- and high-frequency modes are mostly damped just below the photosphere, whereas low-frequency modes demonstrate broader regions of growth and damping. The physics of the damping rate dip near $\nu_{\max}$ was also discussed, and we have addressed the question of why the damping rate dip becomes less pronounced in warmer stars – thermal processes, which tend to destabilize modes and cause the dip near $\nu_{\rm max}$, have relatively lesser impact on the total damping rate in warmer stars.

We caution however, that disagreements do exist between simulations and observations. For example, for Procyon, it seems that 3D simulations overestimate excitation rates. At lower frequencies, we tend to underestimate damping rates because of the limited simulation domain. All these indicators suggest room for improvement to our numerical methods or indicate the necessity of more detailed numerical simulations. More detailed 3D surface (magneto-)convection simulations with higher numerical resolution and deeper vertical coverage may be helpful towards improving the agreement between theory and observation. Meanwhile, a larger number of such simulations that covers adequate $\{T_{\rm eff}, \log g, [{\rm Fe/H}]\}$ combinations could be used to quantify the relationship between mode excitation/damping and fundamental stellar parameters. It may even be possible to quantify the departure, if any, from the widely-used $\nu_{\rm max}$ scaling relation from an entirely theoretical angle.

3.6 Appendix: Linear damping rates

In this appendix, we derive the expression for the linear damping rate used in the main text from basic fluid equations, and elaborate on the numerical technique we developed to extract the damping rates from 3D simulations.

3.6.1 Theoretical formulation

It is necessary to investigate how non-adiabatic processes will affect stellar oscillation for the calculation of the damping rate. In this section, we employ a simplified approach to include non-adiabatic effects on radial p-mode by regarding them as small perturbations. The perturbation will shift the p-mode frequency and introduce an exponential attenuation term in the mode amplitude. The latter is relevant to the damping rate. Similar discussions and derivations can be found also in, e.g., Shapiro & Teukolsky (1983) and Aerts et al. (2010).

We begin with the fluid momentum equation, and, assuming that the system is subjected to no external force other than gravity,

$$\frac{dv^j}{dt} = -\frac{1}{\rho}\nabla_j P - \nabla_j \Phi, \tag{3.12}$$

where v, ρ, P and Φ are fluid velocity, density, pressure and gravitational potential, respectively. The index j denotes the three components in Cartesian coordinates. The perturbed momentum equation then writes

$$\delta\left(\frac{dv^j}{dt} + \frac{1}{\rho}\nabla_j P + \nabla_j \Phi\right) = 0, \tag{3.13}$$

with the symbol δ representing Lagrangian perturbation (Eulerian perturbation is denoted by superscript $'$). Expanding Eq. (3.13) gives

$$\begin{aligned}
&\frac{d^2\xi^j}{dt^2} - \frac{\delta\rho}{\rho_0^2}\nabla_j P_0 + \frac{1}{\rho_0}\nabla_j(\delta P) - \frac{1}{\rho_0}(\nabla_j\xi^k)(\nabla_k P_0) \\
&+ \nabla_j\Phi' + \nabla_j\xi^k\nabla_k\Phi_0 - (\nabla_j\xi^k)(\nabla_k\Phi_0) = 0.
\end{aligned} \tag{3.14}$$

Here $\vec{\xi}$ is the fluid displacement vector, and subscript "0" stands for quantities in equilibrium state. The relation between Eulerian and Lagrangian perturbation is used to obtain Eq. (3.14). Also, the Einstein summation convention is applied throughout this section unless otherwise specified. Eq. (3.14) can be simplified using the hydrostatic equilibrium equation to

$$\nabla_j P_0 + \rho_0\nabla_j\Phi_0 = 0. \tag{3.15}$$

The perturbation to density is related to the fluid displacement vector $\vec{\xi}$ by the perturbed fluid continuity equation

$$\delta\rho = -\rho_0\nabla_k\xi^k. \tag{3.16}$$

And for radial perturbations of a spherical star, the relation between perturbed gravitational potential and fluid displacement is (Shapiro & Teukolsky 1983 chapter 6.3)

$$\nabla_j\Phi' = -4\pi G\rho_0\xi^j, \tag{3.17}$$

where G is the gravitational constant. Plugging Eqs. (3.15), (3.16) and (3.17) into Eq. (3.14), we have

$$\begin{aligned}
&\frac{d^2\xi^j}{dt^2} + \frac{1}{\rho_0}(\nabla_k\xi^k)\nabla_j P_0 + \frac{1}{\rho_0}\nabla_j(\delta P) \\
&- 4\pi G\rho_0\xi^j + \nabla_j\xi^k\nabla_k\Phi_0 = 0.
\end{aligned} \tag{3.18}$$

In the case of adiabatic oscillation, the pressure fluctuation δP is connected with fluid displacement via

$$\frac{\delta P_{\mathrm{ad}}}{P_0} = \Gamma_{1,0}\frac{\delta\rho}{\rho_0} = -\Gamma_{1,0}\nabla_k\xi^k, \tag{3.19}$$

where $\Gamma_1 = (\partial\ln P/\partial\ln\rho)_{\mathrm{ad}}$ is the (first) adiabatic index with subscript "ad" representing fixed entropy. From the relation (3.19) one can recognise that Eq. (3.18) is the characteristic equation of the eigenvalue problem in the scenario of adiabatic oscillation. However, when considering non-adiabatic oscillations, the expression of δP, based on the perturbed energy equation (Aerts et al. 2010 Eq. 3.47), becomes

$$\begin{aligned}
\partial_t\delta P &= \frac{\Gamma_{1,0}P_0}{\rho_0}\partial_t\delta\rho + \rho_0(\Gamma_{3,0}-1)\partial_t\delta q \\
&= \partial_t\delta P_{\mathrm{ad}} + \rho_0(\Gamma_{3,0}-1)\partial_t\delta q,
\end{aligned} \tag{3.20}$$

with q being heating or cooling and $\Gamma_{3,0} - 1 = (\partial\ln T/\partial\ln\rho)_{\mathrm{ad}}$. The second term on the right-hand side of Eq. (3.20) represents the time derivative of the pressure fluctuation associated with non-adiabatic effects, that is,

$$\partial_t \delta P = \partial_t \delta P_{\mathrm{ad}} + \partial_t \delta P_{\mathrm{nad}}. \tag{3.21}$$

If we regard non-adiabatic effects as small perturbation, it is reasonable to assume that the time dependence of ξ, δP and δP_{ad} have the form $\exp(i\omega t)$ (ω and t are angular frequency and time, respectively), and Eqs. (3.18) and (3.21) simplify into[9]

$$\begin{aligned}\omega^2 \xi^j = {} & \frac{1}{\rho_0}(\nabla_k \xi^k)\nabla_j P_0 + \frac{1}{\rho_0}\nabla_j(\delta P) \\ & - 4\pi G \rho_0 \xi^j + \nabla_j \xi^k \nabla_k \Phi_0,\end{aligned} \tag{3.22}$$

$$\delta P = \delta P_{\mathrm{ad}} + \frac{1}{i\omega}\partial_t \delta P_{\mathrm{nad}}. \tag{3.23}$$

Further assume that non-adiabatic pressure fluctuation responds linearly to fluid displacement; then Eqs. (3.22) and (3.23) can be written in the form

$$\mathcal{H}|\xi\rangle = \left[\mathcal{H}^{(0)} + \mathcal{H}^{(1)}\right]|\xi\rangle = \omega^2|\xi\rangle, \tag{3.24}$$

with

$$\begin{aligned}\mathcal{H}^{(0)}_{jk}\xi^k = {} & \frac{1}{\rho_0}(\nabla_k \xi^k)\nabla_j P_0 - \frac{1}{\rho_0}\nabla_j(\Gamma_{1,0} P_0 \nabla_k \xi^k) \\ & - 4\pi G \rho_0 \xi^j + \nabla_j \xi^k \nabla_k \Phi_0,\end{aligned} \tag{3.25}$$

$$\mathcal{H}^{(1)}_{jk}\xi^k = \frac{1}{\rho_0}\nabla_j\left(\frac{1}{i\omega}\partial_t \delta P_{\mathrm{nad}}\right). \tag{3.26}$$

Here we followed the notation from quantum mechanics: $|\xi\rangle$ denotes eigenfunction, $\mathcal{H}^{(0)}$ is the operator (acting on ξ) in the case of adiabatic oscillation, whereas $\mathcal{H}^{(1)}$ accounts for non-adiabatic effects. The eigenfunctions form an orthogonal basis in Hilbert space (Schutz, 1979), with the inner product defined as (Aerts et al. 2010 Eq. 3.246)

$$\langle \xi_a | \xi_b \rangle \equiv \int_V \rho_0 \xi^*_{a,k} \xi^k_b \, dV, \tag{3.27}$$

where "a" and "b" label a specific normal mode and ξ^*_a is the complex conjugate of ξ_a, and V is the volume of star.

Now we solve Eq. (3.24) with the perturbation theory (Aerts et al. 2010 chapter 3.6), and focus on a specific radial p-mode:

$$\mathcal{H}^{(0)}|\xi_p\rangle = \omega_p^2|\xi_p\rangle, \tag{3.28}$$

[9] Assuming time dependence $\exp(i\omega t)$ or $\exp(-i\omega t)$ has no physical significance, it will not affect the final damping rate expression. Also worth noting is that δP_{nad} stems from non-adiabatic effects including entropy fluctuation and convective turbulence, which are stochastic rather than coherent (Stein & Nordlund, 2001; Zhou et al., 2019). Therefore the temporal dependence of δP_{nad} is not $\exp(i\omega t)$.

where ω_p and $|\xi_p\rangle$ are the corresponding mode adiabatic eigenfrequency and adiabatic eigenfunction of this p-mode. The non-adiabatic term at this frequency writes

$$\mathcal{H}^{(1)}|\xi_p\rangle = \frac{1}{\rho_0}\frac{1}{i\omega_p}\,\mathcal{F}\left(\nabla_j\partial_t\delta P_{\rm nad}\right)\big|_{\omega=\omega_p} = \frac{1}{\rho_0}\nabla_j\delta P_{\rm nad}(\omega_p). \tag{3.29}$$

The first-order frequency shift due to non-adiabatic effect, as given by the perturbation analysis, is then

$$\omega^2-\omega_p^2 = \frac{\langle\xi_p|\mathcal{H}^{(1)}|\xi_p\rangle}{\langle\xi_p|\xi_p\rangle}. \tag{3.30}$$

Substituting Eq. (3.29) and the inner product (3.27) into the equation above, we get

$$\omega^2-\omega_p^2 = \frac{\int_V\ \xi_p^{*k}\nabla_k(\delta P_{\rm nad})\,dV}{\int_V\ \rho_0\xi_p^{*k}\xi_{p,k}\,dV}. \tag{3.31}$$

On the left-hand side, the perturbed frequency ω contains a real part and an imaginary part, that is, $\omega=\omega_{\rm Re}+i\omega_{\rm Im}$. Therefore, the perturbed radial p-mode eigenfunction has the form $\xi=\tilde{\xi}\exp(i\omega t)=\tilde{\xi}\exp(i\omega_{\rm Re}t)\exp(-\omega_{\rm Im}t)$, where the exponential part governs the change of mode amplitude. In the circumstance of mode damping, a positive damping rate should correspond to the decay of mode amplitude, hence $\eta=\omega_{\rm Im}$. Because $\omega_{\rm Re}$ is very close to unperturbed (adiabatic) frequency and $\eta\ll\omega_p$, Eq. (3.31) turns out to be

$$\eta\approx\mathfrak{Im}\left\{\frac{\int_V\ \xi_p^{*k}\nabla_k(\delta P_{\rm nad})\,dV}{2\omega_p\int_V\ \rho_0\xi_p^{*k}\xi_{p,k}\,dV}\right\}. \tag{3.32}$$

Integrating the right-hand side of Eq. (3.32) by parts gives

$$\eta\approx\mathfrak{Im}\left\{\frac{\int_V\ \nabla_k(\xi_p^{*k}\delta P_{\rm nad})\,dV}{2\omega_p\int_V\ \rho_0\xi_p^{*k}\xi_{p,k}\,dV}-\frac{\int_V\ (\nabla_k\xi_p^{*k})\delta P_{\rm nad}\,dV}{2\omega_p\int_V\ \rho_0\xi_p^{*k}\xi_{p,k}\,dV}\right\}. \tag{3.33}$$

Applying the divergence theorem to the first term and the perturbed fluid continuity equation (3.16) to the second term, we get

$$\eta\approx\mathfrak{Im}\left\{\frac{\oint_{\rm surf}\ \vec{\xi}_p^{*}\delta P_{\rm nad}\,d\vec{S}}{2\omega_p\int_V\ \rho_0\xi_p^{*k}\xi_{p,k}\,dV}+\frac{\int_V\ (\delta\rho^*/\rho_0)\delta P_{\rm nad}\,dV}{2\omega_p\int_V\ \rho_0\xi_p^{*k}\xi_{p,k}\,dV}\right\}, \tag{3.34}$$

where the integration over the stellar surface is often neglected (cf. Aerts et al. 2010 chapter 3.7 and Nordlund & Stein 2001 Sect. 3), therefore

$$\eta\approx\frac{\int_V\ \mathfrak{Im}\left\{(\delta\rho^*/\rho_0)\delta P_{\rm nad}\right\}\,dV}{2\omega_p\int_V\ \rho_0\xi_p^{*k}\xi_{p,k}\,dV}, \tag{3.35}$$

which is the full expression of the (linear) damping rate from first-order perturbation analysis. We note that Eq. (3.35) is essentially equivalent to η derived in previous investigations such as Belkacem et al. (2012) and Houdek & Dupret (2015).

Next we rearrange and simplify Eq. (3.35) into a different form that is more suitable for numerical evaluation. The denominator of (3.35) is proportional to the mode kinetic energy. For radial modes, it is related with mode mass per unit surface area m_{mode} and mode velocity amplitude at the photosphere $\mathcal{V}(R_{\mathrm{phot}})$ by Nordlund & Stein (2001) Eq. 63:

$$\begin{aligned}\int_V \rho_0 \xi_p^{*k} \xi_{p,k}\, dV &= 4\pi R_{\mathrm{phot}}^2 \int_r \rho_0 |\xi_p|^2 \frac{r^2}{R_{\mathrm{phot}}^2}\, dr \\ &= 4\pi R_{\mathrm{phot}}^2 \frac{2 m_{\mathrm{mode}} |\mathcal{V}(R_{\mathrm{phot}})|^2}{\omega_p^2},\end{aligned} \tag{3.36}$$

where R_{phot} is the photosphere radius. On the other hand, the integral in the numerator of (3.35) is the so-called "work integral", representing energy transfer between convection and oscillations. Ideally, the work integral is finite throughout the entire star. In practice, however, the integral is confined within the simulation domain, outside which δP_{nad} and $\delta\rho$ are not available. Because the 3D simulation covers only a small part of the star near the photosphere, and in subsequent calculations we consider horizontally averaged non-adiabatic fluctuations and density fluctuations, the work integral reduces to

$$4\pi R_{\mathrm{phot}}^2 \int_{y_{\mathrm{bot}}}^{y_{\mathrm{top}}} \mathfrak{Im} \left\{ (\delta\bar{\rho}^* / \bar{\rho}_0) \delta\bar{P}_{\mathrm{nad}} \right\} dy, \tag{3.37}$$

where the bar symbol denotes horizontal averaging, y is the vertical direction in the Cartesian coordinate in which the 3D simulations are set, and y_{top} (y_{bot}) is the geometric depth at the top (bottom) of the simulation domain. Meanwhile, it is worth noting that the near-surface region covered by 3D simulation is where non-adiabatic effects and local compression due to oscillation are the strongest. In the deep stellar interior that is outside the simulation domain, physical processes are very close to adiabatic, and local compression is weaker compared with the near-surface region. Consequently, omitting the work integral in the deep interior might not be a significant simplification. Substituting (3.36) and (3.37) into Eq. (3.35) gives

$$\eta \approx \frac{\omega_p \int_{y_{\mathrm{bot}}}^{y_{\mathrm{top}}} \mathfrak{Im} \left\{ (\delta\bar{\rho}^* / \bar{\rho}_0) \delta\bar{P}_{\mathrm{nad}} \right\} dy}{4 m_{\mathrm{mode}} |\mathcal{V}(R_{\mathrm{phot}})|^2}, \tag{3.38}$$

which is the equation we adopted for numerical computation.

3.6.2 Numerical evaluation

In this section we describe the numerical methods applied to compute the linear damping rates from 3D simulations. Based on Eq. (3.38), four components – density fluctuation $\delta\bar{\rho}$, non-adiabatic pressure fluctuation $\delta\bar{P}_{\mathrm{nad}}$, mode mass per unit surface area m_{mode} and velocity amplitude at photosphere $\mathcal{V}(R_{\mathrm{phot}})$ – are essential in order

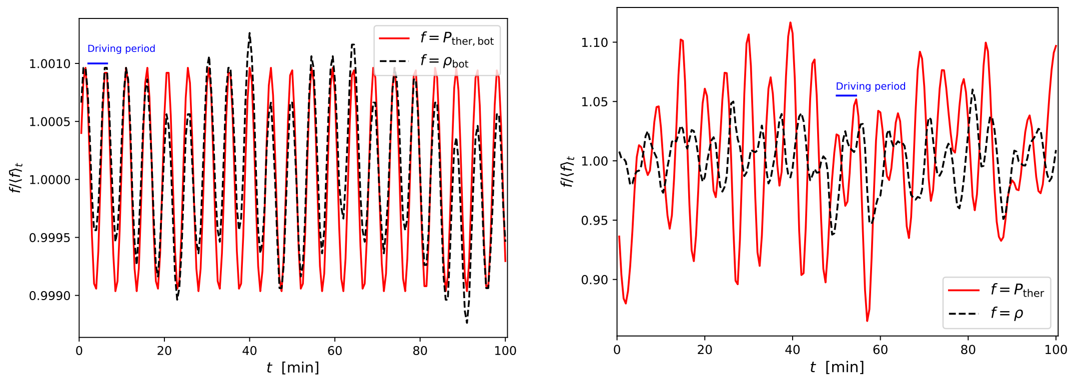

(a) (b)

Figure 3.15: 3.15(a): Time variation of thermal pressure (red solid line) and density (black dashed line) at the bottom boundary of a solar 3D simulation with artificial mode driving. The input perturbation amplitude of this simulation is set to $\epsilon = 0.001$, while the period of artificial driving, which corresponds to a cyclic frequency $\nu_{\rm d} = 3.44$ mHz, is marked in the figure with blue ruler. Both the magnitude and the period of fluctuations are consistent with input values. $\langle ... \rangle_t$ stands for time averaging. 3.15(b): Similar to 3.15(a), but showing time variation of thermal pressure and density near the photosphere.

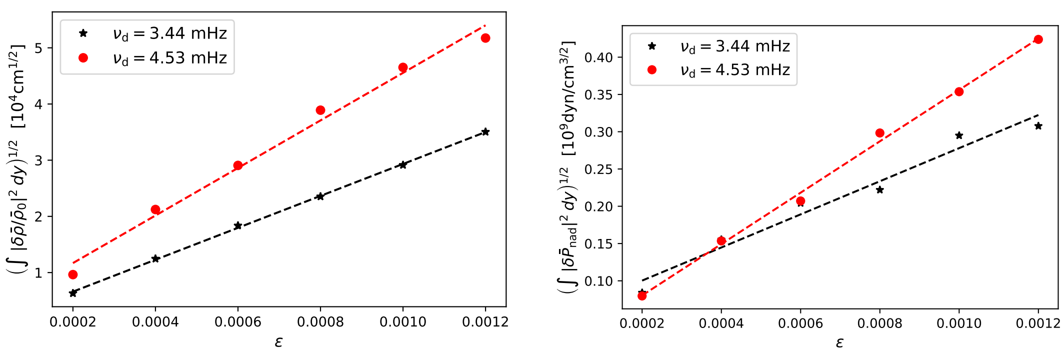

(a) (b)

Figure 3.16: 3.16(a): Integrated density fluctuations at driving frequency for different perturbation amplitudes ϵ. The power spectrum of $\delta\bar{\rho}/\bar{\rho}_0$ is integrated over vertical direction of the entire simulation domain then we take the square root. Black asterisks and red dots are calculated from solar 3D simulations with different driving cyclic frequencies $\nu_{\rm d}$. Linear fits to these data points are presented in dashed lines. 3.16(b): Similar to 3.16(a), but showing integrated non-adiabatic pressure fluctuations at driving frequency for different perturbation amplitudes.

to calculate η. Among them, the coupling between density and non-adiabatic pressure fluctuation represents the interaction between oscillation and convection, with the former reflecting fluid compression results from mode displacement (Eq. (3.16)) while the latter mainly stems from convective turbulence. Although both $\delta\bar{\rho}$ and $\delta\bar{P}_{\rm nad}$ are available from the 3D model, owing to the complexity of physical processes occurring in the simulation domain, $\delta\bar{\rho}$ computed from the simulation comprises not only pulsation signals, but also the signature of "convective noise." To obtain an $\delta\bar{\rho}$ that cleanly reflects the contribution from the mode eigenfunction – in other words, a coherent density fluctuation – we conduct numerical experiments that artificially drive radial mode at a particular frequency to large amplitude. The target mode will thus be prominent in the simulation box and distinguishable from "convective noise."

The artificial driving is achieved by modifying the bottom boundary condition of the simulation. We adopt open bottom boundary conditions in our simulation, where the outgoing flow is free to carry entropy fluctuations out of the simulation domain. In "normal" simulations, incoming flows are forced to have fixed entropy and thermal pressure, which are constant over the horizontal plane. However, in the artificial driving experiment, we impose a small time-dependent perturbation to the thermal pressure at the bottom boundary so that the pressure of incoming flows fluctuates with time. Meanwhile, we enforce constant entropy (to first order) of the incoming flows at the bottom boundary to ensure no extra energy is injected into the system. Namely,

$$\begin{aligned} P_{\rm bot} &= P_{\rm bot,0}\left[1 + \epsilon\sin(\omega_{\rm d}t + \phi)\right], \\ s_{\rm bot} &= s_{\rm bot,0} + \mathcal{O}(\epsilon^2), \end{aligned} \tag{3.39}$$

where $P_{\rm bot,0}$ and $s_{\rm bot,0}$ are constant thermal pressure and constant entropy (per mass) at the bottom boundary of "normal" simulations. The term ϵ is a small, dimensionless number that governs the amplitude of perturbation, $\omega_{\rm d}$ is the angular frequency of artificial driving, and ϕ is the phase. The applied perturbation varies sinusoidally with time and remains uniform over the horizontal plane, since radial oscillations are the focus here.

According to (3.39), other thermochemical quantities, such as mass density and energy density, will also fluctuate coherently with thermal pressure at the bottom boundary (displayed in Fig. 3.15(a)). As a result, the perturbation will generate coherent fluid motion with the same frequency as the driving frequency $\omega_{\rm d}$, and amplify vertical velocity, density and pressure fluctuation to large magnitudes in the entire simulation domain (Fig. 3.15(b)). Given that none of $\delta\bar{\rho}$, $\delta\bar{P}_{\rm nad}$ and $\mathcal{V}(R_{\rm phot})$ are realistic from artificial driving, it is natural to question whether one could obtain reliable damping rates from such a numerical experiment. The answer to this question is affirmative if $\delta\bar{\rho}$, $\delta\bar{P}_{\rm nad}$ and $\mathcal{V}(R_{\rm phot})$ all respond linearly to mode displacement. In this scenario, the unrealistically large oscillation amplitude resulting from artificial driving cancels out if we calculate η via Eq. (3.38). Because velocity is the time derivative of mode displacement, it is linearly proportional to the mode amplitude that is controlled by ϵ. The density fluctuation is related to mode displacement by (3.16), which is a linear relation as well. However, the linearity between $\delta\bar{P}_{\mathrm{nad}}$ and mode displacement – upon which we also rely when deriving the linear damping rate from perturbation theory (see Sect. 3.6.1) – is not apparent. To this end, we compute $\delta\bar{P}_{\mathrm{nad}}$ for different perturbation amplitudes ϵ (all other input parameters are exactly the same except for ϵ in order to control variables), and depict $\delta\bar{P}_{\mathrm{nad}}$ at the driving frequency as a function of ϵ in Fig. 3.16(b). As observed from Fig. 3.16(b), $\delta\bar{P}_{\mathrm{nad}}$ responds nearly linear to ϵ between $\epsilon = 0.0002$ and 0.0012, suggesting an approximately linear relationship between non-adiabatic pressure fluctuation and mode displacement. Thus, we can claim that such artificial driving simulations are able to give reliable damping rate results because the rates of $\delta\bar{\rho}$, $\delta\bar{P}_{\mathrm{nad}}$ and $\mathcal{V}(R_{\mathrm{phot}})$ enhancement are similar to each other, so that the artificial effect from "mode driving" largely cancels out between $(\delta\bar{\rho}^*/\bar{\rho}_0)\delta\bar{P}_{\mathrm{nad}}$ and $|\mathcal{V}(R_{\mathrm{phot}})|^2$ when we compute damping rate at the driving frequency using Eq. (3.38).

Such numerical experiments are repeated at different driving frequencies to obtain theoretical damping rates as a function of frequency. For the purpose of controlling variables, for a given star, all artificial driving experiments are carried out with the same time duration (roughly 40-50 period of the longest driving period, that is, the lowest driving frequency) and perturbation amplitude. Other input parameters are also identical except for the driving frequency. The exact values of driving frequencies are determined based on three constraints. First, because in this work we are interested in modes with frequencies close to the observed ν_{max}, the selected driving frequencies range from approximately $2\nu_{\mathrm{max}} - \nu_{\mathrm{ac}}$ to ν_{ac}, where ν_{ac} is the acoustic cut-off frequency of our target star which can be estimated from the seismic scaling relation (e.g., Eq. 1 of Belkacem et al. 2011). Second, driving frequencies are chosen to be close to the measured $l = 0$ mode frequencies of the target star. Additionally, we require that the whole simulation period be an integer multiple of the driving period so that the damping rate does not depend on the phase of the driving, and no interpolation is needed when processing the Fourier transformed simulation data. All artificial mode driving simulations are initiated from the same snapshot that was generated in a "normal simulation." The exact configurations (numerical resolutions, timespan, sampling interval etc.) of artificial mode driving simulations for our target stars are presented in Sect. 3.2.2.

We evaluate η in the frequency domain using numerical data produced by the artificial driving simulation. Density and non-adiabatic pressure fluctuation are computed in a pseudo-Lagrangian frame that filters out the main effects of p-mode oscillations in the simulation box (Zhou et al. 2019 Sect. 3.2). In pseudo-Lagrangian frame, density fluctuation

$$\frac{\delta\bar{\rho}(t)}{\bar{\rho}_0} = \frac{\bar{\rho}_{\mathrm{L}}(t) - \bar{\rho}_{0,\mathrm{L}}}{\bar{\rho}_{0,\mathrm{L}}}, \tag{3.40}$$

and the non-adiabatic pressure fluctuation read (Zhou et al. 2019 Eq. 13)

$$\begin{aligned}\delta\bar{P}_{\mathrm{nad}}(t) = [(&\ln\bar{P}_{\mathrm{L}}(t) - \ln\bar{P}_{0,\mathrm{L}}) \\ &- \bar{\Gamma}_{1,\mathrm{L}}\,(\ln\bar{\rho}_{\mathrm{L}}(t) - \ln\bar{\rho}_{0,\mathrm{L}})]\,\bar{P}_{\mathrm{L}}.\end{aligned} \tag{3.41}$$

Table 3.5: Damping rates computed at representative driving frequencies with low and normal resolution simulations. All quantities are in μHz, and no smoothing is performed here.

		Low	Intermediate	High
	$\nu_{\rm d}$	1852	2391	2996
KIC 6225718	η ($120^2 \times 125$)	2.8	16.4	30.7
	η (240^3)	5.6	16.1	30.8
	$\nu_{\rm d}$	774	1044	1380
β Hydri	η ($120^2 \times 125$)	0.8	6.1	18.4
	η (240^3)	1.2	6.3	16.1
	$\nu_{\rm d}$	541	691	869
δ Eri	η ($120^2 \times 125$)	1.2	3.3	11.8
	η (240^3)	1.1	1.4	11.1

Here, quantities defined in the pseudo-Lagrangian frame are marked with subscript "L." We then transfer density and non-adiabatic pressure fluctuation from time to frequency domain and take the complex conjugate of $\delta\bar{\rho}$. The imaginary part of $(\delta\bar{\rho}^*/\bar{\rho}_0)\delta\bar{P}_{\rm nad}$ at the driving frequency is integrated from the bottom boundary, along vertical direction, to the top boundary of the simulation domain. The result is multiplied by (angular) driving frequency to finally obtain the numerator of Eq. (3.38). On the other side, the photospheric velocity amplitude is also evaluated from the 3D simulation. First, we average vertical velocity over the horizontal plane and compute its power spectrum. The power spectrum is then multiplied by 2 in order to convert to velocity amplitude power $|\mathcal{V}|^2$. Next, the value of $|\mathcal{V}|^2$ near optical depth unity at driving frequency is exacted to represent $|\mathcal{V}(R_{\rm phot})|^2$ in Eq. (3.38). Mode mass per unit surface area $m_{\rm mode}$, however, is calculated from the 1D patched model using ADIPLS.

3.6.2.1 Effects of numerical resolution

As discussed above, the artificial driving simulation is repeated at different driving frequencies to obtain η as a function of frequency. In other words, 20–30 such simulations are needed for each target star, which is very costly in terms of computation time and power. A promising solution to this practical issue is to carry out artificial driving simulations in lower resolution ($120^2 \times 125$). However, reducing numerical resolution, or equivalently, increasing grid spacing, will impact the small scale structure of convection and the dissipation of short wavelength fluctuations through artificial diffusion (which depends on grid spacing, see Nordlund & Galsgaard 1995 Sect. 3 and Stein & Nordlund 1998 Sect. 2) etc. The accuracy of the work integral is likely to be affected as well because of fewer grids points in the vertical direction. Therefore, the effect of numerical resolution on damping rate results should be investigated before opting for low resolution simulations.

Here, we study this problem in detail for KIC 6225718, β Hydri and δ Eri. For each star, we carried out artificial driving simulations at three representative driving frequencies (one far below $\nu_{\max}$ of the corresponding star, one near $\nu_{\max}$ and one far greater than $\nu_{\max}$) with both low and normal resolution (240^3). In order to isolate the effect of resolution, all simulations are initiated from the same snapshot, and share the same time duration, sampling interval, and physical extent of the simulation box (see table 3.3), with numerical resolution being the only difference. Note that Procyon is not investigated, as it is currently not feasible to carry out multiple artificial driving simulations for this star at 240^3 resolution with available computational resources[10]. Nevertheless, we are aware that numerical resolution may have an impact on the theoretical damping rate of Procyon, therefore results presented in Fig. 3.5 should be interpreted with recognition of this caveat.

The results of our resolution studies are shown in Table 3.5. At high frequencies, damping rates demonstrate little dependence on numerical resolution for all stars investigated. A possible explanation is that high-frequency oscillations are mostly damped in a small region near the photosphere (Fig. 3.13(a)) where our simulations have the highest vertical resolution so that even $120^2 \times 125$ resolution simulations are able to resolve the damping of high-frequency oscillations. In the case of KIC 6225718 and β Hydri, damping rates evaluated at intermediate driving frequencies are not sensitive to resolution. However, for δ Eri, an obvious resolution effect is observed, which suggests that artificial driving simulation with $120^2 \times 125$ resolution is not sufficient for this star. Damping rates at low frequencies also show clear dependence on numerical resolution. Nevertheless, the resolution effect here is not of great concern because the accuracy of low-frequency theoretical damping rates are primarily limited by the vertical size of simulation domain, as already stated in the main text and demonstrated further in Sect. 3.6.2.2.

In short, for KIC 6225718 and β Hydri, it is adequate to perform the artificial driving simulation with low resolution in order to reduce computation cost. In the case of δ Eri however, artificial driving simulations with at least 240^3 resolution are required. Given that δ Eri is quite distinguishable from the other two stars both in terms of basic stellar parameters and evolutionary stage (Sect. 3.2.1), our resolution study might imply that at least normal numerical resolution is necessary to obtain reliable damping rates for low surface gravity subgiants and red giants.

3.6.2.2 Effects of vertical extent of the simulation

It was stated in Sect. 3.4 that damping rates at low frequencies are underestimated because of the limited size of 3D simulation. Had the 3D model been extended to deeper stellar interior, the expectation is that this discrepancy would be reduced. In this subsection, we provide substantial evidence of these assertions by comparing

[10]Convection simulation of F-type stars are much more computationally expensive than cooler stars, as they have high radiative cooling rate and strong velocity field near photosphere. Both factors lead to smaller simulation timestep (relative to the typical timescale of convection) compared to G- and K-type stars.

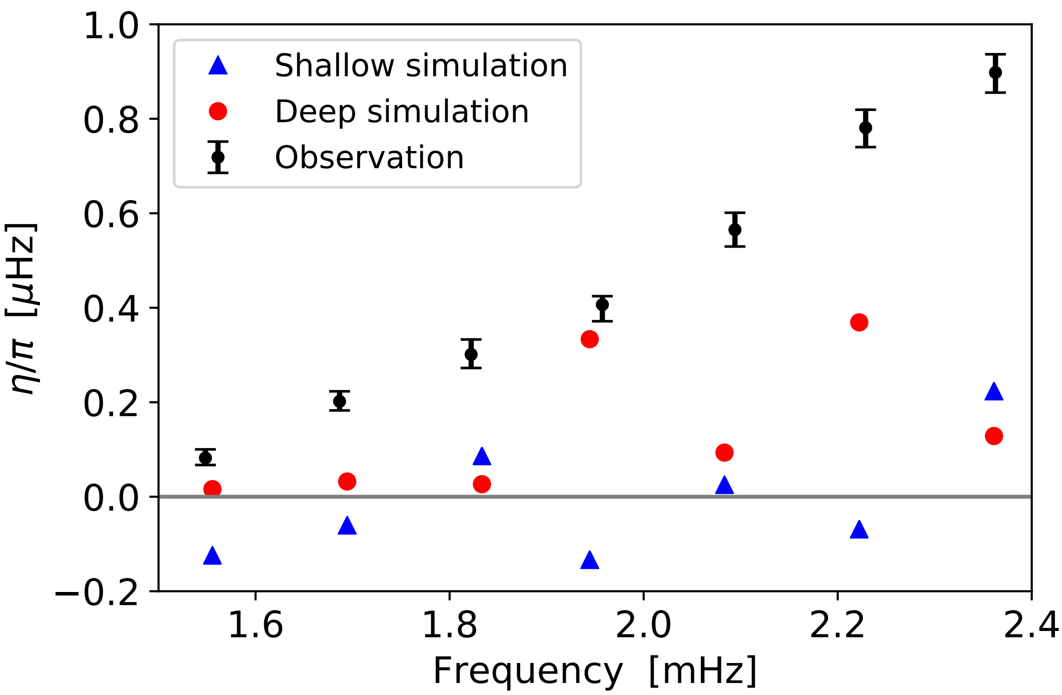

Figure 3.17: Low-frequency damping rates computed from shallow (blue triangles) and deep (red dots) solar simulations without any smoothing. Theoretical results are divided by π to compare with measured $l = 0$ line widths from BiSON (Birmingham Solar Oscillations Network, Chaplin et al. 2005; Davies et al. 2014).

low-frequency theoretical damping rates computed from two sets of solar simulations with different vertical extent. The first group has the same simulation set-up as simulations used in Zhou et al. (2019), which covers 3.8 Mm in the vertical direction: approximately 1 Mm above the base of the photosphere and 2.8 Mm below it. We will refer to this as the "shallow simulation" hereinafter. The second group, i.e. the "deep simulation," extends from approximately 0.9 Mm above the base of the photosphere to 7 Mm below. For both sets of simulations, we calculate η at identical driving frequencies between 1.5 mHz and 2.5 mHz following the method described above. The shallow and deep simulations also share the same sampling interval (30 seconds) and total timespan (10 hours) in order to make them comparable. Low-frequency damping rates computed from two groups of simulation, together with measured solar radial mode line widths in this frequency range (Chaplin et al., 2005; Davies et al., 2014), are presented in Fig. 3.17. It is obvious that damping rates computed from deep simulations are overall larger than results from shallow ones, confirming our assertions in the main text. Still, at two driving frequencies, the shallow simulations predict higher η than the deep ones, which might be the consequence of the stochastic nature of mode damping. Also apparent is that the shallow simulation gives negative damping rates at four selected frequencies; this is in conflict with the consensus that solar radial modes are stable (Houdek & Dupret, 2015). This contradiction suggests low-frequency damping rates computed based on shallow simulations are not reliable, even qualitatively. This problem, however, is never seen in deep simulations.

By extending the simulation domain deeper into stellar interior, the discrepancy in η between simulation and observation is indeed reduced. Nevertheless, some uncertainty remains: damping rates predicted by deep simulations are still systematically lower than observed values for reasons that are currently unclear. The remaining uncertainty in the low frequency range will be investigated further in future work.

Chapter 4

The relationship between photometric and spectroscopic oscillation amplitudes from 3D stellar atmosphere simulations

Yixiao Zhou, Thomas Nordlander, Luca Casagrande, Meridith Joyce, Yaguang Li, Anish M. Amarsi, Henrique Reggiani and Martin Asplund, *The relationship between photometric and spectroscopic oscillation amplitudes from 3D stellar atmosphere simulations*, 2021, Monthly Notices of the Royal Astronomical Society, 503, 13.

Abstract

We establish a quantitative relationship between photometric and spectroscopic detections of solar-like oscillations using *ab initio*, three-dimensional (3D), hydrodynamical numerical simulations of stellar atmospheres. We present a theoretical derivation as proof of concept for our method. We perform realistic spectral line formation calculations to quantify the ratio between luminosity and radial velocity amplitude for two case studies: the Sun and the red giant ϵ Tau. Luminosity amplitudes are computed based on the bolometric flux predicted by 3D simulations with granulation background modelled the same way as asteroseismic observations. Radial velocity amplitudes are determined from the wavelength shift of synthesized spectral lines with methods closely resembling those used in BiSON and SONG observations. Consequently, the theoretical luminosity to radial velocity amplitude ratios are directly comparable with corresponding observations. For the Sun, we predict theoretical ratios of 21.0 and 23.7 ppm/[m s^{-1}] from BiSON and SONG respectively, in good agreement with observations 19.1 and 21.6 ppm/[m s^{-1}]. For ϵ Tau, we predict *K2* and SONG ratios of 48.4 ppm/[m s^{-1}], again in good agreement with observations 42.2 ppm/[m s^{-1}], and much improved over the result from conventional empirical scaling relations which gives 23.2 ppm/[m s^{-1}]. This study thus opens the path towards a quantitative understanding of solar-like oscillations, via detailed modelling

of 3D stellar atmospheres.

4.1 Introduction

Solar-like oscillations can be observed via photometry and spectroscopy. The photometric method allows us to detect stellar oscillations by measuring variations in the brightness of stars, whereas the spectroscopic method exploits the Doppler shifts of spectral lines to detect stellar oscillations. The spectroscopic method (also called the radial velocity method) is employed by ground-based telescopes such as Birmingham Solar Oscillations Network (BiSON, Chaplin et al. 1996) and Stellar Oscillations Network Group (SONG, Grundahl et al. 2006). These instrumments have laid the groundwork for helioseismoloy and asteroseismology through their detailed observations of solar oscillations and their detection of the first solar-like oscillating stars (Claverie et al., 1979; Brown et al., 1991; Bedding et al., 2001; Kjeldsen et al., 2003).

Built upon these pioneering works, the field of asteroseismology has thrived in the last decade thanks to the CoRoT (Michel et al., 2008), *Kepler* (Borucki et al., 2010) and TESS (Ricker et al., 2015) missions that detect stellar oscillations by measuring variations in stellar luminosity. The high-quality, long time-series, extensive photometric data provided by these space-based telescopes enable accurate determination of oscillation frequencies and amplitudes for thousands of solar-like stars, thus ushering in the era of ensemble asteroseismology. However, in the low-frequency regime the photometric method is complicated by signals due to stellar atmospheric convection (stellar granulation), which impedes the characterisation of low-frequency oscillations. This difficulty can be avoided by observing the star using the radial velocity method, as stellar granulation noise is significantly less pronounced in velocity signals. Moreover, the radial velocity method has demonstrated great potential for measuring oscillations in cool dwarf stars (e.g. Kjeldsen et al. 2005), which are important in exoplanet science but difficult to detect with space-photometry due to their low intrinsic luminosity and small oscillation amplitude (Huber et al., 2019). Nonetheless, ground-based spectroscopy is limited by target brightness and the Earth's atmosphere.

It follows that the photometric and spectroscopic methods of measuring stellar oscillations are highly complementary and that combining the two methods will yield extra information that can further constrain the properties of stars. Recently, solar-like oscillations in several stars, such as Procyon A and ϵ Tauri (hereafter ϵ Tau), have been observed in both photometry and spectroscopy (Huber et al., 2011a; Arentoft et al., 2019). With the commencement of the TESS mission and SONG observations, many stars will soon have both luminosity and radial velocity data available. Therefore, investigating the relationship between luminosity and radial velocity amplitude is of increasing importance.

This topic was first explored in the pioneering study of solar-like oscillations by Kjeldsen & Bedding (1995), who proposed a quantitative relationship between luminosity and radial velocity oscillation amplitudes for solar-like stars by scaling from the Sun. The Kjeldsen & Bedding (1995) amplitude ratio scaling relation has been the industry standard in asteroseismology until now, providing valuable guidance for many years. However, their relationship is based on empirical arguments, and it is unable to reproduce the observed amplitude ratio for some stars (Huber et al., 2011a; Arentoft et al., 2019). It is therefore prudent and timely to refine the relationship between luminosity and radial velocity based on detailed stellar modelling. As a first attempt to solve this problem from a modelling perspective, Houdek et al. (1999) and Houdek (2010) computed the theoretical ratio between luminosity and velocity amplitudes. The calculations are based on their one-dimensional, non-local, time dependent convection model for the Sun (Houdek et al., 1999) and the scaled VAL-C atmosphere for Procyon A (Vernazza et al., 1981; Houdek, 2010). Their amplitude ratio results are in reasonable agreement with observations. Nevertheless, it is worth noting that the predicted amplitude ratio depends on at which atmospheric height the velocity amplitude is evaluated (see Fig. 1 and 2 of Houdek 2010).

In this paper, we investigate the relationship between photometric and spectroscopic measurements of stellar oscillations. We quantify the amplitude ratio in an essentially parameter-free manner, by carrying out detailed *ab initio* three-dimensional (3D) hydrodynamical simulations of stellar surface convection. We base our analysis on realistic synthetic spectra, calculated using 3D radiative transfer and taking into account departures from local thermodynamic equilibrium (LTE) where necessary.

4.2 Observational Data

In this pilot study, we focus on the Sun and on the G-type red giant star ϵ Tau (HD 28305). As a bright star residing in the nearest open Cluster, Hyades, and known exoplanet host, ϵ Tau is of great interest to stellar physics for a variety of reasons (Sato et al., 2007).

We adopt the stellar parameters provided in Arentoft et al. (2019): $T_{\rm eff} = 4976$ K, $\log g = 2.67$ dex, $[{\rm Fe/H}] = 0.15$ dex, as reference values. This effective temperature was determined via the bolometric flux measured by Baines et al. (2018) and the angular diameter measured interferometrically from the CHARA array (Arentoft et al., 2019). The surface gravity was determined from the observed frequency of maximum power, $\nu_{\rm max}$, for this star (Stello et al., 2017; Arentoft et al., 2019) through the $\nu_{\rm max}$ scaling relation (Brown et al., 1991; Kjeldsen & Bedding, 1995). Moreover, detailed asteroseismic observations for ϵ Tau using both *K2* (the successor of *Kepler*; Howell et al. 2014) and SONG yield individual oscillation frequencies for more than 20 modes as well as the amplitude ratio between *K2* and SONG, which makes ϵ Tau an ideal target to investigate in this work. Analogous parameters for the Sun are, of course, known to the highest degrees of precision and accuracy of any star. Observational parameters are included in Table 4.1.

Table 4.1: Fundamental parameters and basic information about the simulation of the Sun and ϵ Tau. Reference values are adopted from Prša et al. (2016) and Arentoft et al. (2019), respectively. We note that the effective temperature fluctuates over time in 3D models, therefore both mean effective temperature and its standard deviation are given. Also, both minimum and maximum vertical grid spacing are provided, as mesh points are not uniformly distributed vertically.

		Sun	ϵ Tau
T_{eff} (K)	Reference	5772.0 ± 0.8	4976 ± 63
	Modelling	5773 ± 16	4979 ± 18
$\log g$ (cgs)	Reference	4.438	2.67
	Modelling	4.438	2.67
[Fe/H] (dex)	Reference	0.00	0.15 ± 0.02
	Modelling	0.00	0.00
Numerical resolution		240^3	240^3
Time duration (hour)		24	1205.8
Sampling interval (s)		30	1447
Vertical size (Mm)		3.6	250
Vertical grid spacing (km)		7–33	562–2650
Horizontal grid spacing (km)		25	2165

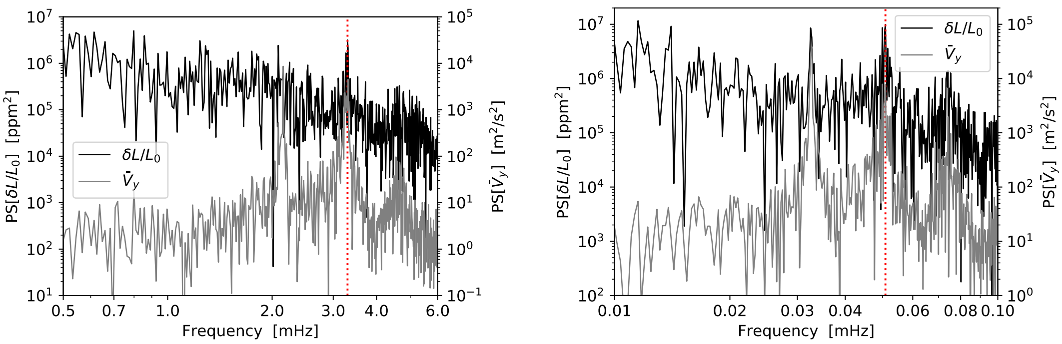

(a) (b)

Figure 4.1: 4.1(a): The power spectrum of luminosity amplitude (black line) calculated from the 3D solar atmosphere model is plotted together with the power spectrum of the horizontally averaged vertical velocity amplitude around the photosphere (grey line). Three simulation modes are clearly seen in the velocity spectrum, whereas only the simulation mode with frequency slightly greater than 3 mHz is recognizable in the luminosity spectrum. Red dotted vertical line indicates the frequency of the dominant simulation mode. 4.1(b): Power spectra calculated from the 3D atmosphere model for ϵ Tau. Three simulation modes are visible in both the velocity and luminosity spectra.

4.3 Three-dimensional stellar atmosphere models

In this section, we introduce the 3D hydrodynamic stellar atmosphere models that are the basis of our analysis. All 3D models are computed with a customized version of the Stagger code (Nordlund & Galsgaard, 1995; Collet et al., 2018), a radiative-magnetohydrodynamic code that solves the time-dependent equations of mass, momentum and energy conservation, as well as the magnetic-field induction equation and the radiative transfer equation on a 3D staggered Eulerian mesh. The stellar models in the present study have been constructed without magnetic fields. All scalars are evaluated at cell centres, whereas vectors, such as velocity, are staggered at the centres of cell faces in order to improve numerical accuracy. The code incorporates realistic microphysics and a detailed radiative transfer scheme. An updated version of the Mihalas et al. (1988) equation of state (Trampedach et al., 2013) is adopted, which accounts for all ionization stages of the 17 most abundant elements in the Sun plus the H_2 molecule. A comprehensive collection of relevant continuous absorption and scattering sources is included as described in Hayek et al. (2010). The pre-computed, sampled line opacities are taken from the MARCS model atmosphere package (Gustafsson et al., 2008). Radiative energy transport is modelled by solving the equation of radiative transfer at every time step of the simulation for all mesh points above a certain Rosseland mean optical depth ($\tau_{\mathrm{Ross}} \leq 500$ throughout this work) under the assumption of LTE. The frequency dependence of the radiative transfer equation is approximated via the opacity binning method (Nordlund, 1982; Collet et al., 2018), in which 12 opacity bins are divided based on wavelength and strength of opacities. Consequently, the integration over wavelength reduces to the summation over 12 selected bins. The spatial dependence of the radiative transfer equation is represented by solving along a set of inclined rays in space. Nine directions – one vertical and eight inclined directions representing combinations of two polar and four azimuthal angles – are considered for all models presented in this work. The integration over polar angle is carried out using the Gauss-Radau quadrature scheme. The thus evaluated radiative heating rates can be used to calculate the surface flux (i.e., the emergent radiative flux at the top boundary of simulation domain) and subsequently the effective temperature via the Stefan-Boltzmann law.

The basic configurations of our 3D models are summarised in Table 4.1. For both the Sun and the red giant ϵ Tau, the Stagger model atmospheres are constructed based on the reference effective temperatures and surface gravities (Table 4.1). The Asplund et al. (2009) solar chemical composition is adopted in both cases. Though we do not expect stellar metallicity to introduce any significant differences for the purposes of this study, we intend to consider the effects of stellar metallicity in detail in a later investigation.

Spatially, the simulation domain is discretized in a box located around the stellar photosphere. Horizontally, the simulation domain is a square with 240×240 evenly distributed mesh points. The horizontal size of the box is large enough to enclose at least ten granules at any time of the simulation (Magic et al., 2013a). There are 240 mesh points in the vertical direction covering roughly the outer 1% of the stellar radius, extending from the upper part of the surface convection zone, including the entire optical surface, and reaching the lower part of the chromosphere; we note that the outer-most layers are likely the least realistic given our neglect of magnetic fields in these simulations. Because the vertical scale of the simulation is very small compared to the total stellar radius, the spherical effects are negligible and gravitational acceleration can be regarded as a constant (i.e. the surface gravity). Mesh points are not evenly distributed vertically: the highest numerical resolution is applied around the optical surface to resolve the transition between the optically thick and thin regimes. Furthermore, in the case of ϵ Tau, a separate vertical mesh structure is employed for the radiative transfer calculation in order to resolve the extremely steep temperature and opacity gradients near the optical surface of red giants adequately (see e.g., Fig. 3 of Collet et al. 2018). Adaptive mesh refinement was used when constructing the vertical radiative mesh; the radiative mesh of each vertical sub-domain within the simulation domain is arranged based on the distribution of Rosseland optical depth in this sub-domain, resulting in highest numerical resolution near the photosphere (see Fig. 6 in Collet et al. 2018 for an illustration). At each simulation time step, radiative transfer calculations are performed on the radiative mesh and then interpolated back to the aforementioned hydrodynamical mesh. We refer the reader to Section 2.7 in Collet et al. (2018) for a detailed introduction to this technique.

Boundaries are periodic in the horizontal direction while open in the vertical (Collet et al., 2018). At the bottom boundary, outgoing flows (vertical velocities towards stellar centre) are free to carry their entropy fluctuations out of the simulation domain, whereas incoming flows have invariant entropy and thermal (gas plus radiation) pressure. Temporally, the duration of the simulation is one day for the Sun, and about 50 days for ϵ Tau. Simulation data is stored every 30 seconds in the solar simulation while every 1447 seconds for the red giant case. A long stellar time coverage like this is necessary for an accurate analysis of stellar oscillations.

Sound waves and the resulting p-modes are natural phenomena in surface convection simulations, which can be directly identified by looking at the power spectrum of the vertical velocity of the simulations. Because p-mode oscillations in the simulation domain periodically shift the optical surface up and down, causing coherent changes in surface temperature, simulation modes can also be identified indirectly from the power spectrum of the bolometric flux variation. The relative variation of the bolometric flux, in parts per million (ppm), is defined as

$$\frac{\delta F_{\mathrm{bol}}}{F_{\mathrm{bol},0}} = \frac{F_{\mathrm{bol}} - F_{\mathrm{bol},0}}{F_{\mathrm{bol},0}} \times 10^6 = \frac{\delta L}{L_0}. \tag{4.1}$$

This is essentially equivalent to the relative variation in luminosity $\delta L/L_0$ (in ppm) because oscillations hardly change the total stellar radius. The subscript "0" indicates time-averaged quantities, i.e. the equilibrium state.

The power spectra (PS) of the vertical velocity variation and the relative luminosity variation (luminosity spectrum for short hereinafter) are computed via

$$\begin{aligned} \mathrm{PS}[f](\omega) &= \frac{4}{N^2}\left|\sum_{s=0}^{N-1} f(t_s)e^{i\omega s\Delta t}\right|^2 \\ \omega &= \frac{2\pi}{N\Delta t}\left(1, 2, ..., \frac{N}{2}-1\right) \\ f &= \bar{V}_y \quad \text{or} \quad \frac{\delta L}{L_0}. \end{aligned} \tag{4.2}$$

Here, $\bar{V}_y$ is the horizontally averaged vertical velocity, and the terms t, Δt and ω are time, time interval between two consecutive snapshots and angular frequency, respectively. The symbol s denotes individual simulation snapshots, and N is the total number of snapshots.

Fig. 4.1 shows the results for the solar and the red giant simulations. Three radial simulation modes with frequencies of approximately 2.1, 3.3, and 4.7 mHz are seen in the vertical velocity spectrum of the solar simulation. These are the fundamental, first overtone, and second overtone radial modes in the simulation box, respectively. Among the three, only the intermediate-frequency, first overtone simulation mode is clearly recognizable from the luminosity spectrum. The reason is that at low frequencies, the granulation signal is relatively strong, causing the signature of the low-frequency simulation mode to be overwhelmed by "convective noise." On the other hand, the amplitude of the high-frequency simulation mode is too small to be clearly identified in the luminosity spectrum (black line in Fig. 4.1(a)). We therefore refer to the first overtone radial mode as the dominant simulation mode, as it is the only one that is identifiable in both the vertical velocity and luminosity spectra in the solar case. The situation for the ϵ Tau simulation is different. The three simulation modes are visible in both the velocity and luminosity spectra owing to their large amplitude. We note that for both the Sun and ϵ Tau, the duration of the simulation is long enough to cover at least 200 periods of the dominant simulation mode. Likewise, the sampling interval is short enough in both cases such that at least 10 snapshots are stored within one pulsation cycle of the dominant simulation mode. These two factors together ensure that the dominant simulation mode is well resolved in the frequency domain. The exact frequency of the dominant simulation mode is important for the analysis below (Sect. 4.5 and 4.6). It is determined by looking for the local maximum $\bar{V}_y$ for all vertical layers in the simulation domain, which is similar to the method used in Belkacem et al. (2019). The exact frequency values are 3.299 mHz and 0.051 mHz for the solar and ϵ Tau simulation respectively, which are also highlighted in red dotted lines in Fig. 4.1.

It is worth noting that the amplitude of simulation mode is on the order of $100\,\mathrm{m\,s^{-1}}$. This is much greater than the observed amplitude of radial p-modes as measured in the solar flux spectrum, which is around $0.2\,\mathrm{m\,s^{-1}}$. This difference in amplitude between the simulation mode and the observed stellar p-mode was explained in detail in Belkacem et al. (2019) and Zhou et al. (2019). In short, the discrepancy emerges from the difference between the volume of the simulation box and the volume of the real star. Stellar p-modes propagate throughout the entire stellar surface and interior, whereas the simulation modes are confined to the simulation box whose horizontal and vertical extents are significantly smaller than the dimensions of a star. Therefore, the luminosity or velocity amplitudes from 3D atmosphere simulations are not directly comparable to the corresponding asteroseismic observations. A natural question is then whether realistic ratio between luminosity and velocity amplitude can be predicted from our simulations? We address this question in detail in the subsequent section.

4.4 Proof of concept

We demonstrate in this section that, in principle, 3D surface convection simulations are able to reliably predict the relationship between the luminosity and velocity amplitudes (the amplitude ratio) despite their individual values not being comparable with observations. We begin with the relative luminosity variation defined in Eq. (4.1). Assuming the source function in the radiative transfer equation S_ν (ν is the radiation frequency) is a linear function of optical depth τ_ν (i.e. equivalent to the Eddington-Barbier approximation), the surface flux at a given frequency is given by:

$$F_\nu(\tau_\nu = 0) = \pi S_\nu(\tau_\nu = 2/3). \tag{4.3}$$

Further assuming LTE gives

$$F_\nu(\tau_\nu = 0) = \pi B_\nu(\tau_\nu = 2/3) = \pi \frac{2h\nu^3}{c^2} \frac{1}{\exp\left[\frac{h\nu}{k_B T(\tau_\nu = 2/3)}\right] - 1}. \tag{4.4}$$

Here, B_ν is the Planck function, c, h and k_B are speed of light, Planck constant and Boltzmann constant, respectively. The term $T(\tau_\nu = 2/3)$ is the temperature at optical depth $\tau_\nu = 2/3$. Because at different frequencies, the $\tau_\nu = 2/3$ layer corresponds to different locations in the stellar atmosphere due to opacity variations, $T(\tau_\nu = 2/3)$ depends on frequency in general. In the case of a grey atmosphere where optical depth has no frequency dependence, the integration of F_ν over frequency gives the Stefan-Boltzmann law. The bolometric flux is hence

$$F_{\rm bol} = \pi \int_0^\infty B_\nu(\tau = 2/3)\, d\nu = \sigma T^4(\tau = 2/3), \tag{4.5}$$

where σ is the Stefan-Boltzmann constant. Combining Eqs. (4.1) and (4.5) yields

$$\frac{\delta L}{L_0} = \frac{4\delta T(\tau = 2/3)}{T_0(\tau = 2/3)} \times 10^6, \tag{4.6}$$

where δT denotes temperature fluctuation at constant optical depth. From Eq. (4.6) we can then recognise that the luminosity variation essentially captures the fluctuation in temperature at the optical surface. For solar-type stars without strong stellar activity, such fluctuation is due primarily to surface convection and secondarily due to acoustic oscillations. The contribution due to surface convection will be separated from the acoustic oscillations in Sect. 4.5.1.

Next we connect fluid velocity V with the fluctuations of thermodynamical quantities. Following the discussion in Aerts et al. (2010) (see Chapter 3.1.4), we assume V is caused solely by sound waves and is small compared to the sound speed. It is worth noting that convective velocities are non-negligible in stellar convection zones; their magnitude can even be comparable to the local sound speed in the near-surface region. Nevertheless, convective velocities are effectively regarded as "equilibrium state," since oscillation is the focus here. Under this assumption, density ρ, pressure P and temperature T can be written as $f = f_0 + f'$, where f' is the small Eulerian perturbation[1] (second and higher order terms are ignored). After further assuming that the medium is spatially homogeneous, all derivatives of equilibrium quantities vanish. The fluid continuity equation

$$\frac{\partial \rho}{\partial t} + \nabla \cdot (\rho \vec{V}) = 0 \tag{4.7}$$

then becomes

$$\frac{\partial \rho'}{\partial t} + \rho_0 \nabla \cdot \vec{V} = 0, \tag{4.8}$$

while the equation of motion

$$\rho \frac{\partial \vec{V}}{\partial t} + \rho \vec{V} \cdot \nabla \vec{V} = -\nabla P + \rho \vec{g} \tag{4.9}$$

becomes

$$\rho_0 \frac{\partial \vec{V}}{\partial t} = -\nabla P' + \rho_0 \vec{g}', \tag{4.10}$$

where g is gravitational acceleration. If we ignore the perturbation to gravitational acceleration $\vec{g}'$ (i.e. Cowling approximation), this simplifies to

$$\rho_0 \frac{\partial \vec{V}}{\partial t} + \nabla P' = 0. \tag{4.11}$$

Now taking the time derivative of Eq. (4.8) and making use of Eq. (4.11), we have

$$\frac{\partial^2 \rho'}{\partial t^2} - \nabla^2 P' = 0. \tag{4.12}$$

In the case of adiabatic oscillation, pressure and density fluctuations are connected by

$$P' = c_{s,0}^2 \rho', \tag{4.13}$$

where $c_s = \sqrt{(\partial P / \partial \rho)_{\mathrm{ad}}}$ is the adiabatic sound speed. Substituting Eq. (4.13) into

[1]Perturbations at constant geometric depth (or radius)

Eq. (4.12) gives the wave equation (Aerts et al. 2010 Eq. 3.51):

$$\frac{\partial^2 \rho'}{\partial t^2} - c_{s,0}^2 \nabla^2 \rho' = 0. \tag{4.14}$$

If we now consider a pure radial sound wave in which all quantities depend only on the y-coordinate, then density and pressure fluctuation can be written as

$$\begin{aligned} \rho' &= a \cos(ky - \omega t), \\ P' &= c_{s,0}^2 a \cos(ky - \omega t), \end{aligned} \tag{4.15}$$

where a and k denote amplitude and wave number, respectively. The dispersion relation is therefore

$$\omega^2 = c_{s,0}^2 k^2. \tag{4.16}$$

Based on Eqs. (4.11), (4.15) and the dispersion relation (4.16), the expression of fluid velocity can be written as

$$V = \frac{c_{s,0}}{\rho_0} a \cos(ky - \omega t). \tag{4.17}$$

Comparing Eq. (4.15) and Eq. (4.17) gives the relation between pressure fluctuation and fluid velocity:

$$P' = \rho_0 c_{s,0} V. \tag{4.18}$$

We recall that, for adiabatic oscillations, pressure and temperature fluctuations are related via

$$\frac{T'}{T_0} = \nabla_{\mathrm{ad},0} \frac{P'}{P_0}, \tag{4.19}$$

with $\nabla_{\mathrm{ad}} = (\partial \ln T / \partial \ln P)_{\mathrm{ad}}$ being the adiabatic temperature gradient. The relation between the temperature fluctuation and the fluid velocity is given by

$$T' = \frac{\rho_0 c_{s,0} T_0 \nabla_{\mathrm{ad},0}}{P_0} V. \tag{4.20}$$

For additional information about relevant discussion and derivations, see Landau & Lifshitz (1987) chapter 64 and Aerts et al. (2010) chapter 3.1.4.

We have now obtained the relationship between $\delta L / L_0$ and δT (the temperature fluctuation at constant optical depth), as well as the relationship between V and T' (the temperature fluctuation at constant geometric depth). The next step is to link these two temperature fluctuations. Considering only first order perturbations, the temperature at given optical depth τ at any given time can be separated as

$$T(\tau, t) = T_0(\tau) + \delta T(\tau, t). \tag{4.21}$$

At fixed geometric depth near the photosphere, the optical depth varies with time because of the time-dependent nature of convection. Therefore, the temperature at fixed geometric depth, if expressed as a function of τ, reads

$$T(\tau + d\tau, t) = T(\tau, t) + \frac{\partial T}{\partial \tau} d\tau = T_0(\tau) + \delta T(\tau, t) + \frac{\partial T}{\partial \tau} d\tau. \tag{4.22}$$

Because $T_0(\tau)$ represents the equilibrium state, the Eulerian perturbation to temperature is therefore

$$T'(\tau, t) = T(\tau + d\tau, t) - T_0(\tau) = \delta T(\tau, t) + \frac{\partial T}{\partial \tau} d\tau. \tag{4.23}$$

This equation demonstrates the relationship between two different kinds of perturbation, it can be expanded further by analysing the term $d\tau$. In the equilibrium state, the optical depth is, by definition,

$$\tau = \int_{-\infty}^{y_0} \alpha_0 \, dy, \tag{4.24}$$

where y is the geometric depth as before and α_0 is the mean absorption coefficient. Recalling that at a given time t, $\tau + d\tau$ corresponds to the same geometric depth y_0, we have

$$\tau + d\tau = \int_{-\infty}^{y_0} \alpha(t) \, dy. \tag{4.25}$$

Subtracting Eq. (4.24) from Eq. (4.25) gives

$$d\tau = \int_{-\infty}^{y_0} \delta\alpha(t) \, dy, \tag{4.26}$$

which relates the perturbation of the absorption coefficient at constant τ to the change in optical depth at fixed geometric depth. The value of the absorption coefficient, however, depends on the opacity source of the plasma in a complex way. As such, there is no simple analytical function to describe the relationship between α and the thermodynamical quantities. Nevertheless, given the fact that the H^- opacity is the dominant source of opacity near the solar photosphere, we adopt the simplification that the mass absorption coefficient consists only of H^- opacity: κ_{H^-} (units $cm^2 g^{-1}$). Here we adopt a power-law fit of κ_{H^-} (Hansen et al. 2004 Eq. 4.65), which gives reasonable results in our range of interest ($3000 \lesssim T \lesssim 6000$ K; $10^{-10} \lesssim \rho \lesssim 10^{-5}$ g/cm^3; hydrogen mass fraction of around 0.7; metal mass fraction $0.001 \lesssim Z \lesssim 0.03$):

$$\begin{aligned} \kappa_{H^-} &\simeq 2.5 \times 10^{-31} (Z/0.02) \rho^{1/2} T^9 \qquad \mathrm{cm}^2/\mathrm{g}, \\ \alpha \simeq \rho \kappa_{H^-} &\simeq 2.5 \times 10^{-31} (Z/0.02) \rho^{3/2} T^9 \qquad \mathrm{cm}^{-1}. \end{aligned} \tag{4.27}$$

The perturbation of the absorption coefficient is then

$$\delta\alpha \simeq \alpha_0 \left(\frac{3\delta\rho}{2\rho_0} + \frac{9\delta T}{T_0} \right), \tag{4.28}$$

where $\delta\rho$ is the perturbation of density at fixed optical depth. As indicated by 3D surface convection simulations, the magnitude of $\delta\rho$ and ρ' are similar around photosphere (Fig. 3 of Magic et al. 2013b). Hence, using also Eqs. (4.13), (4.18) and (4.20), we have

$$\delta\rho \simeq \rho' = \frac{P_0}{c_{s,0}^2 \nabla_{\rm ad,0} T_0} T'. \tag{4.29}$$

Substituting Eqs. (4.28) and (4.29) into Eq. (4.26) yields

$$d\tau \simeq \int_{-\infty}^{y_0} \alpha_0 \left(\frac{3P_0}{2\rho_0 c_{s,0}^2 \nabla_{\rm ad,0} T_0} T' + \frac{9}{T_0}\delta T \right) dy. \tag{4.30}$$

As the absorption coefficient α_0 increases rapidly when moving from the upper atmosphere to photosphere (Eq. (4.27)), the main contribution to the right hand side of Eq. (4.30) comes from a thin layer just above y_0. Therefore, Eq. (4.30) can be approximated by

$$d\tau \simeq \tau \left(\frac{3P_0}{2\rho_0 c_{s,0}^2 \nabla_{\rm ad,0} T_0} T' + \frac{9}{T_0}\delta T \right)_\tau . \tag{4.31}$$

Under the assumption of the Eddington grey atmosphere and LTE, the temperature stratification is

$$T(\tau) = T_{\rm eff} \left(\frac{3}{4}\tau + \frac{1}{2} \right)^{\frac{1}{4}}, \tag{4.32}$$

which is the so-called Eddington $T-\tau$ relation. Making use of the Eddington $T-\tau$ relation and plugging Eq. (4.31) into Eq. (4.23), we have

$$T' \simeq \delta T + \frac{3}{16} T_{\rm eff,0} \left(\frac{3}{4}\tau + \frac{1}{2} \right)^{-\frac{3}{4}} \tau \left(\frac{3P_0}{2\rho_0 c_{s,0}^2 \nabla_{\rm ad,0} T_0} T' + \frac{9}{T_0}\delta T \right)_\tau . \tag{4.33}$$

Evaluating the equation above at $\tau = 2/3$ gives the relationship between T' and δT at the optical surface:

$$\left(1 - \frac{3P_0}{16\rho_0 c_{s,0}^2 \nabla_{\rm ad,0}} \right)_{\tau=\frac{2}{3}} T'(\tau = 2/3, t) \simeq \frac{17}{8} \delta T(\tau = 2/3, t). \tag{4.34}$$

The ratio between T' and δT at $\tau = 2/3$ computed based on Eq. (4.34) is approximately 3.2 for our solar atmosphere model, in reasonable agreement with the corresponding result evaluated directly from simulation data, which is approximately 2.3 (see also Magic et al. 2013b Sect. 4.1).

Finally, combining Eqs. (4.6), (4.20) and (4.34) gives the relationship between the luminosity and velocity amplitudes:

$$\frac{\delta L}{L_0} \simeq \frac{32}{17} \times 10^6 \left(\frac{\rho_0 c_{s,0} \nabla_{\rm ad,0}}{P_0} - \frac{3}{16 c_{s,0}} \right)_{\tau=\frac{2}{3}} V(\tau = 2/3). \tag{4.35}$$

Eq. (4.35) demonstrates that, to first order, the ratio between relative luminosity variation and photosphere velocity depends only on the equilibrium state of the thermodynamic quantities. We are now equipped to address the question put forward at the end of Sect. 4.3: it is thus demonstrated that 3D surface convection simulations do have the potential to reliably predict the luminosity and velocity amplitude ratio, because the ratio does not depend on the luminosity or velocity amplitude nor on any other term that is subject to overestimation by our box-in-a-star models.

We note that a number of approximations and simplifications have been employed when deriving Eq. (4.35). Itemized, these assumptions are:

- The Eddington-Barbier approximation
- Local thermodynamic equilibrium
- Grey atmosphere
- Convective velocities are regarded as the "equilibrium state", such that fluid velocity V consists only of an oscillation component and is small compared to the sound speed
- Spatially homogeneous medium
- The Cowling approximation
- Adiabatic oscillations
- H^- is the only source of opacity in the stellar photosphere, such that it can be represented by a power law $\kappa_{H^-} \propto \rho^{1/2}T^9$
- The magnitude of $\delta\rho$ and ρ' are similar around photosphere

Some of these assumption, such as the grey atmosphere and spatially homogeneous medium assumptions, are obviously not correct in the near-surface regions. Therefore, the analysis above is only to illustrate that 3D simulations are capable of providing a reliable luminosity and velocity amplitude ratio. We emphasise, however, that Eq. (4.35) is not used to calculate the ratio between luminosity and velocity amplitude; rather, we evaluate luminosity variation and radial velocity directly from 3D simulations that do not rely on these assumptions.

4.5 Evaluating luminosity amplitude

4.5.1 Intrinsic bolometric amplitude

Intrinsic bolometric flux is an output quantity from the 3D stellar surface convection simulations. It is computed from the radiative transfer calculations performed at each time step of the simulation (Sect. 4.3). The theoretical bolometric flux as a function of time, which is analogous to the intrinsic light curve of star, is converted to $\delta L/L_0$ according to Eq. (4.1). This is then transformed to the (oscillation) frequency domain using a Lomb-Scargle Periodogram algorithm (Lomb, 1976; Scargle, 1982) to obtain

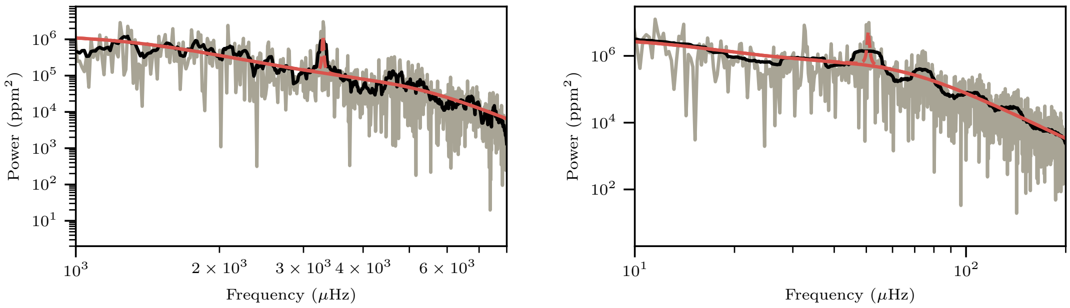

(a) (b)

Figure 4.2: 4.2(a): Grey line is the luminosity power spectrum computed from the solar simulation, and the black curve is the result after smoothing with a running mean with width equals to 100 μHz. Red solid line represents the granulation background of the solar simulation, as modelled based on Eq. (4.38). A Lorentzian fit to the dominant simulation mode is also shown in red dashed line. 4.2(b): Luminosity power spectrum and granulation background predicted from our ϵ Tau simulation. The black curve is obtained by smoothing the luminosity power spectrum with a running mean with width equals to 10 μHz.

the luminosity power spectrum shown in Fig. 4.2 (grey lines). A general trend of the luminosity power spectra is that the luminosity power is higher at low frequencies and decreases with increasing frequency. In the solar case, a peak located around 3.3 mHz is clearly seen in the spectrum. This feature is associated with surface convection (granulation), where up- and downflows shift the location of the optical surface, producing fluctuations in bolometric flux. The peak around 3.3 mHz is caused by the main oscillation mode of the simulation box. Acoustic waves naturally excited in the simulation domain periodically change the location of optical surface, leading to coherent variations in bolometric flux. The variation due to granulation happens on all time-scales and thus provides the background signal in the power spectrum; for an even longer time-sequence this granulation signal becomes more and more smooth, making it easier to discern the frequencies of the oscillation modes.

In order to obtain the luminosity amplitude for the simulation mode, it is necessary to filter out the contribution from granulation. At a given spatial position near the photosphere, granulation emerges, evolves, and disappears with a typical time scale t_{gran}. Having the insight that granulation (essentially surface velocity field) is constantly evolving, Harvey (1985) proposed that the autocorrelation function of stellar granulation can be described by exponential function $\exp(-t/t_{\text{gran}})$. That is, the correlation between granulation at moments t_0 and $t_0 + t$ decreases exponentially with increasing time interval. Because the autocorrelation of a signal corresponds to the Fourier transform of its power spectrum, the power spectrum of granulation background is the Fourier transform of

$$\mathcal{V}(t) = \begin{cases} \mathcal{V}_0 e^{-t/t_{\mathrm{gran}}} & (t \geq 0) \\ 0 & (t < 0) \end{cases}, \tag{4.36}$$

which is

$$\mathcal{B}(\nu) = \frac{C\mathcal{V}_0^2 t_{\mathrm{gran}}}{1 + (2\pi\nu t_{\mathrm{gran}})^2}. \tag{4.37}$$

This is a Lorentzian function. The term $\mathcal{V}_0$ is the velocity amplitude associated with granulation, ν is cyclic frequency and C is a normalization constant such that the power spectrum satisfies the Parseval theorem (see also Eq. 5 of Lund et al. 2017). In recognition of this, we modelled the oscillation background caused by granulation with the sum of one or more (generalized) Lorentzian profiles:[2]

$$\mathcal{B}(\nu) = \sum_{i=1}^{N} \frac{2\sqrt{2}}{\pi} \frac{a_{1,i}^2 / a_{2,i}}{1 + (\nu / a_{2,i})^{a_{3,i}}}, \tag{4.38}$$

which is similar to the functional forms commonly applied to real observational data (e.g. Lund et al. 2017; Li et al. 2020). Here, the free parameters are $\{a_{1,i}, a_{2,i}, a_{3,i}\}$ and N is the number of Lorentzian components. As multiple Lorentzian components are often employed to achieve a better fit to the observed stellar background, the interpretation is that in real stars, there exists more than one granulation scale as well as contributions from stellar activity. Nevertheless, the true analytical form of stellar granulation background remains elusive (Lundkvist et al., 2021). Therefore, we test granulation background models with one, two and three components ($N = 1, 2, 3$) by computing the Bayesian evidence (marginal likelihood) for each model. The Bayesian evidence $p(D|\mathcal{M})$, which is the probability of the power spectrum data D given a granulation model $\mathcal{M}$, is frequently used to evaluate the relative probability of the models for given data. We find that for both the Sun and ϵ Tau, the Bayesian evidence of the single-component background model is significantly smaller than multi-component models while $p(D|\mathcal{M})$ of $N = 2$ and $N = 3$ models are not significantly different. Our Bayesian approach therefore shows that given the theoretical luminosity spectrum, the granulation background is better described by multi-component Lorentzian profiles. In this study, we choose the two-component ($N = 2$) model, because it performs equally well as the three-component one but involves fewer free parameters. We refer the readers to Lundkvist et al. (2021) for a detailed examination of different granulation background models against results from 3D surface convection simulations.

The granulation background fitting is performed with the parallel tempering MCMC (Markov chain Monte Carlo) algorithm of Vousden et al. (2016). The best-fitting results are demonstrated in red solid lines in Fig. 4.2. The amplitude of the granulation background at the frequency of the dominant simulation mode is

[2] Strictly speaking, Eq. (4.38) is the sum of generalized Lorentzian profiles because $a_{3,i}$ is a free parameter rather than fixed to 2. Here we refer them as Lorentzian profiles for simplicity.

Table 4.2: Conversion factor $c_{P-\text{bol}}$ computed for *Kepler* for the Sun and ϵ Tau. "3D" , "ATLAS9" and "Planck" represent the choice of model atmosphere (3D model atmosphere in this work, ATLAS9 model atmosphere, and black body respectively) applied in the computation. The "ATLAS9" and "Planck" results are obtained by interpolating the data provided in Lund (2019).

Star	3D	ATLAS9	Planck
Sun	0.92	0.94	0.98
ϵ Tau	0.68	0.79	0.87

343.6 ± 14.7 ppm for the solar simulation and 726.0 ± 31.2 ppm for the ϵ Tau case. Uncertainties presented here are returned from the MCMC samples, representing the statistical errors associated with the background fitting. We then subtracted the power spectrum with the best fitting background. The bolometric oscillation amplitude is determined by taking the square root of the peak value (corresponds to the value at the frequency of the dominant simulation mode) of the subtracted spectrum, which is 1714.0 ± 3.0 ppm for the solar simulation and 3070.3 ± 7.4 ppm for ϵ Tau (also tabulated in Table 4.4). We note that another frequently used method to extract the oscillation amplitude is to fit a parametric model to the peak region, then take the peak value of the fitted curve. However, in our solar simulation, the width of the simulation mode, which is connected to the mode damping rate, is on the order of $10 - 100$ μHz (see also Table 1 of Belkacem et al. 2019), being much larger than the width of solar p-modes. The reason is that the simulations modes have much less mode mass than stellar p-modes. Therefore, to avoid further complications about the reliability of the width, we measure only the peak amplitude at the frequency of the dominant simulation mode in our analysis.

4.5.2 The conversion factor between intrinsic and measured luminosity amplitude

Space-based missions such as CoRoT, *Kepler* and TESS measure starlight in a certain band-pass. What is measured from these space-based observations is stellar flux in certain wavelength ranges, rather than the intrinsic bolometric stellar flux. In order to connect the luminosity amplitude provided by 3D simulations with observables, it is necessary to quantify the conversion factor between intrinsic and measured luminosity amplitude (also called bolometric correction factor for luminosity amplitude) which is defined as

$$A_{\text{bol}} = c_{P-\text{bol}} A_P, \tag{4.39}$$

where $c_{P-\text{bol}}$ is the conversion factor. The term A_{bol} and A_P are intrinsic luminosity amplitude and luminosity amplitude measured in a certain band-pass respectively. The conversion factor was first investigated by Michel et al. (2009) for CoRoT and Ballot et al. (2011) for *Kepler*. Recently, Lund (2019) quantified $c_{P-\text{bol}}$ values for CoRoT, *Kepler* and TESS across the HR diagram based on a grid of ATLAS9 model fluxes

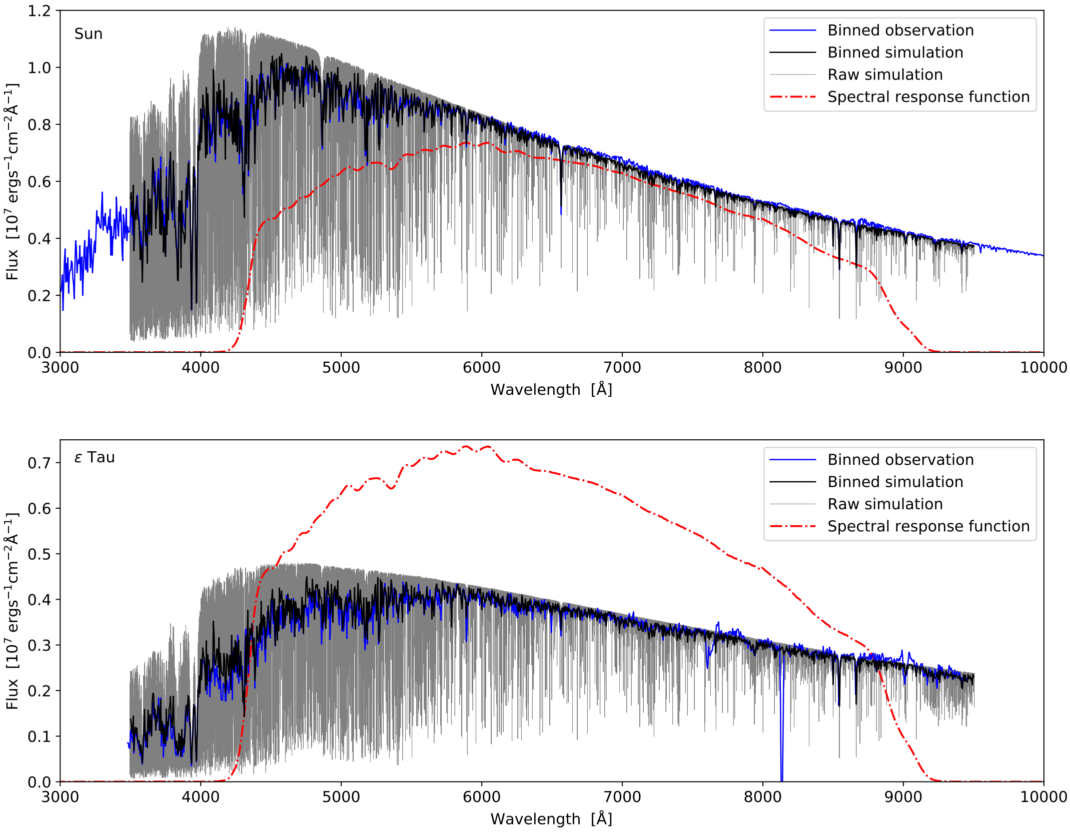

Figure 4.3: *Upper panel*: Thin grey line is the emergent flux between 3500 and 9500 Å computed based on one example snapshot of our 3D solar model atmosphere (at a resolution of $15\,\mathrm{km\,s^{-1}}$). The re-sampled synthetic spectrum using a 5 Å wavelength bin is depicted with the black line. The observed high resolution solar flux spectrum of Kurucz (2005) is also binned every 5 Å (blue line) in order to facilitate comparison between simulation and observation. Red dash-dotted line is the mean spectral response function of *Kepler* averaged from its 84 channels (Thompson et al., 2016). *Lower panel*: Similar to the upper panel, but the result for ϵ Tau. Because the observed ϵ Tau spectrum of Valdes et al. (2004) lacks an absolute flux level, we normalise the original observation data such that its magnitude generally matches the 4976 K (the reference effective temperature of ϵ Tau) black body spectrum between 7000 and 9000 Å. We note that data shown in this figure is not used to calculate $c_{P-\mathrm{bol}}$. Instead, the synthetic spectra that enter into Eq. (4.40) have a lower wavelength resolution (1 nm, see text).

(Castelli & Kurucz, 2003). Here we follow their theoretical formulation, but we calculate the flux spectrum from our 3D models to obtain self-consistent conversion factors for the two stars investigated in this work. For radial oscillations, the expression of $c_{P-\mathrm{bol}}$, as given in Lund (2019), is

$$c_{P-\mathrm{bol}} = \frac{4\int \mathcal{T}_P(\lambda)F(\lambda)d\lambda}{T_{\mathrm{eff}}\int \mathcal{T}_P(\lambda)\frac{\partial F(\lambda)}{\partial T_{\mathrm{eff}}}d\lambda}, \tag{4.40}$$

where λ is wavelength. Note that the stellar spectral flux $F(\lambda)$ also depends on basic stellar parameters i.e. T_{eff}, $\log g$ and [Fe/H]. The instrumental transfer function $\mathcal{T}_P(\lambda)$ is connected with the spectral response function $\mathcal{S}_\lambda$ via $\mathcal{T}_P(\lambda) = \mathcal{S}_\lambda/(hc/\lambda)$, where the latter represents the band-pass of the instrument. In this study we choose the *Kepler* spectral response function as an example.

The stellar spectral flux $F(\lambda)$ in Eq. (4.40) is computed using the 3D radiative transfer code SCATE (Hayek et al., 2011). SCATE solves the 3D, time-dependent radiative transfer problem for both spectral lines and the background continuum. The computation is carried out under the LTE assumption, but with the ability to include isotropic continuum scattering in opacities and source functions. Simulation snapshots generated from the STAGGER code are input models in SCATE. The equation-of-state, continuum absorption and scattering coefficients, and the pre-tabulated line opacities adopted in SCATE are identical to those used in STAGGER, thereby ensuring full consistency between the 3D surface convection simulations and 3D LTE line formation calculations. For more information about the code and the numerical method therein, we refer the readers to Hayek et al. (2010, 2011).

Here we use the spectrum synthesis mode of SCATE. In this scenario, the code delivers the angle-resolved surface fluxes for many wavelength points while treating scattering as pure absorption; test calculations reveal that for our target stars and for the wavelengths of interest here, this is an excellent approximation. At a given wavelength, continuum opacities are computed on-the-fly based on the microphysics and 3D atmosphere models mentioned above; line opacities are read from the pre-tabulated opacity sampling data. Specific intensities are calculated by tilting the simulation domain to represent five different polar angles θ, and rotated to yield four equidistant azimuthal angles ϕ, for a total of 20 rays. The emergent flux is finally computed through integration of the specific intensities on a Gauss-Legendre quadrature in the polar direction, and trapezoidal integration in the azimuthal direction. We compute the emergent flux between 350 and 950 nm, covering the entire spectral response function of *Kepler*, in steps of 1 nm. In order to reduce the computational cost, we compute the spectral energy distribution only for a subset of the simulation sequence covering four periods of the dominant simulation mode. This corresponds to 40 snapshots in the solar simulation and 55 snapshots in the red giant simulation. The spectral flux distributions computed based on one example snapshot of our 3D solar and ϵ Tau model atmosphere are depicted in Fig. 4.3, together with the spectral response function $\mathcal{S}_\lambda$ for *Kepler* which is taken from Thompson et al. (2016). From Fig. 4.3 we can see that for both stars, the predicted spectral flux distributions agree reasonably well with observations, both in magnitude and in overall trend.

The time-averaged (average over all selected snapshots) spectral flux $F(\lambda)$ is used to calculate $c_{P-\mathrm{bol}}$ through Eq. (4.40). The derivative term $\partial F(\lambda)/\partial T_{\mathrm{eff}}$ can be evaluated from the same simulation snapshots. More specifically, by synthesising the flux spectrum for each individual simulation snapshot, we can obtain $F(\lambda)$ as a function of T_{eff} because different simulation snapshots correspond to different bolometric flux, hence effective temperature. This then permits the numerical evaluation of $\partial F(\lambda)/\partial T_{\mathrm{eff}}$ at the reference effective temperature of the star. The $c_{P-\mathrm{bol}}$ values computed based on the aforementioned simulation configuration are presented in Table 4.2. In the case of ϵ Tau, the conversion factor calculated from the 3D model is 0.68, more than 10% less than the corresponding ATLAS9 result given in Lund (2019). We have verified for both the Sun and ϵ Tau that our $c_{P-\mathrm{bol}}$ value is robust, as (1) increasing the number of polar angles in the radiative transfer calculation from five to ten has negligible effect on the final $c_{P-\mathrm{bol}}$ value; and (2) neither increasing the wavelength resolution from 1 nm to 1 Å nor doubling the simulation time sequence in the flux spectrum calculation changes the outcome. Different model atmospheres is a likely cause of the discrepancy in $c_{P-\mathrm{bol}}$, as $c_{P-\mathrm{bol}}$ computed from the black body spectrum also differs clearly from the one computed from ATLAS9, as seen in Table 4.2.

It is worth noting that in principle the conversion factor $c_{P-\mathrm{bol}}$ is not strictly a constant because the flux emitted by a star fluctuates with time. The fluctuation is caused by stellar granulation and oscillation for solar-type stars with the contribution from granulation generally being much larger (Kallinger et al. 2014). According to Kallinger et al. (2014), the measured solar bolometric granulation amplitude is $A_{\mathrm{gran}} = 41$ ppm, corresponding to a fluctuation of approximately 0.06 K in effective temperature. Assuming a black body spectrum, the 0.06 K fluctuation in T_{eff} will result in a relative change of less than 10^{-5} in $c_{P-\mathrm{bol}}$. For ϵ Tau, the bolometric granulation amplitude, estimated from the scaling relation $A_{\mathrm{gran}} \propto (g^2 M)^{-1/4}$ (Kallinger et al. 2014 Eq. 5), is roughly 250 ppm, corresponding to a ~ 0.3 K temperature fluctuation and a relative change in $c_{P-\mathrm{bol}}$ of less than 10^{-4}. Therefore, regarding the conversion factor as a constant is a suitable approximation.

4.6 Evaluating radial velocity amplitude

In the spectroscopic method of measuring stellar oscillations, variations in the radial (i.e. line-of-sight) velocity near the stellar photosphere are quantified by analysing the Doppler shift of certain spectral lines. Two representative efforts based on this method are the Birmingham Solar Oscillations Network (BiSON, Chaplin et al. 1996) and Stellar Oscillations Network Group (SONG, Grundahl et al. 2006). As implied by its name, BiSON focus solely on helioseismology: it detects solar oscillations using the Doppler shift of the disk-integrated solar potassium (K I) 7698 Å line. The spectrograph operates by imposing a magnetic field on a sample of potassium gas; the anomalous Zeeman effect produces line splitting where the σ_- and σ_+ line components located in the blue and red wings of the solar K I line exhibit circular polarisation with opposite orientation. Incident sunlight fed through the instrument passes through a linear polarizer and a quarter-wave plate, which induces circular polarization that can be rapidly switched between left- and right-handedness in order to produce resonant scattering with either line component. This allows the measurement of the relative intensity between the blue and red wing, which reflects the Doppler shift of solar K I line that is caused by the velocity field of the solar surface. A thorough explanation of the BiSON instrumentation and observation technique can be found in Chaplin et al. (1996).

In contrast, SONG measures the radial velocity signal simultaneously from a large number of spectral lines through a traditional echelle spectrograph that covers the wide spectral range 4400–6900 Å (Grundahl et al., 2017). The incident starlight passes through an iodine cell, which superimposes on the stellar spectrum a large number of weak absorption lines; these act as a highly accurate simultaneously recorded wavelength reference. The overall Doppler shift is inferred by cross-correlating the observed spectrum with a reference spectrum that was recorded without the iodine cell. Because radial velocity quantified in this manner takes many spectral lines into account, the result reflects the mean velocity of the photosphere rather than the velocities at the specific heights where certain lines are formed. A more detailed description of the iodine cell method is given by Butler et al. (1996), and its application to SONG is described in detail by Antoci et al. (2013). To make theoretical predictions as consistent as possible with observations, we extract the radial velocity from our 3D atmosphere models through line formation calculations with a method resembling the BiSON and SONG observational setups in the following subsections.

4.6.1 Simulating the BiSON radial velocity signal

Although 3D hydrodynamic simulations are able to realistically predict the convective velocities throughout the simulation domain (e.g. Asplund et al., 2000; Nordlund et al., 2009; Pereira et al., 2013), what BiSON measures is a radial velocity as imprinted on a particular spectral line, which is connected but not equivalent to the fluid velocity given by 3D simulations. In practice, spectral lines form over a range of atmospheric heights, and velocity fields are thus imprinted to varying extent on the core and wings (see e.g. Asplund et al., 2000; Chiavassa et al., 2018). We therefore opt to carry out a forward-modelling approach by performing line formation calculations for the solar K I line. Due to the pronounced departures from LTE for the K I 7698 Å resonance line (Bruls et al., 1992; Reggiani et al., 2019), it is crucial to carry out full 3D non-LTE radiative transfer computations to obtain realistic atmospheric velocity information.

The line formation calculations are performed using BALDER (Amarsi et al., 2016a,b, 2018), a 3D non-LTE radiative transfer code based on the MULTI3D code (Botnen & Carlsson, 1999; Leenaarts & Carlsson, 2009). Our model atom contains 29 levels of K I plus the K II ground state, and resolves the fine structure in all doublets of K I.

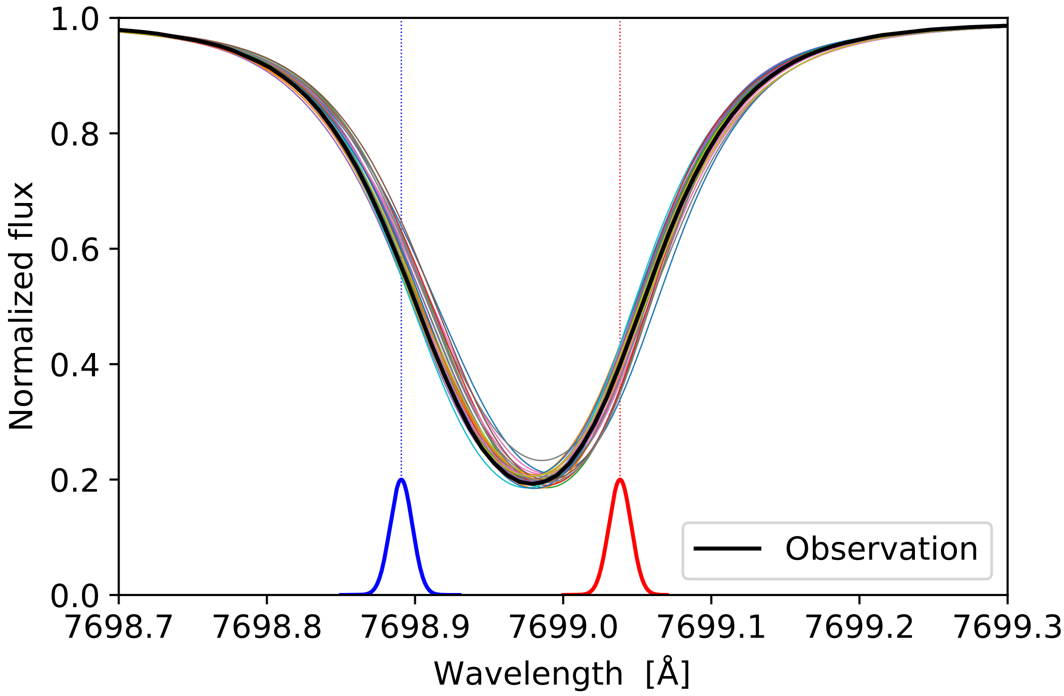

Figure 4.4: Spatially averaged K I line profiles predicted from our 3D non-LTE line formation calculations. The line formation calculation is done for every simulation snapshot, but only one in every 100 snapshots are shown here to avoid over-crowded figure. The observed solar K I line profile is plotted in black line for comparison (Neckel, 1999). The effects of gravitational redshift (633 $\mathrm{m\,s^{-1}}$ for the Sun, Dravins 2008) are included in both the theoretical and the observed line profiles. The blue and red Gaussian profiles schematically represent the two laboratory potassium lines used in BiSON, whose central wavelengths are marked by vertical dotted lines.

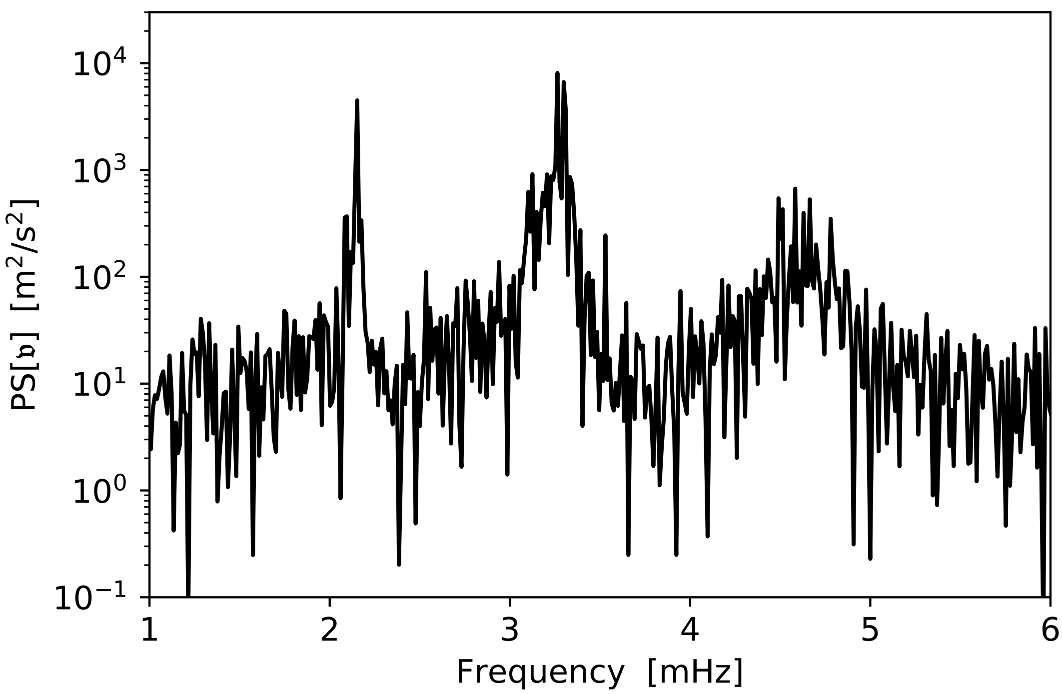

Figure 4.5: The power spectrum of radial velocity amplitude, with three peaks correspond to three simulation modes. The power spectrum here should not be confused with the grey line in Fig. 4.1(a), the plot here reflects radial velocity variation in the K I line forming regions while the latter is the fluctuation of vertical component of fluid velocity near the photosphere.

Atomic energy levels and oscillator strengths originate from NIST (Sansonetti, 2008), and collisional line broadening is computed following the method of Barklem et al. (1998). We implement transition rates due to collisions with electrons and hydrogen atoms following Reggiani et al. (2019). For radiative transitions our simplified atom considers only the 7664–7698 Å resonance line doublet, as their departure from LTE is almost entirely explained through photon losses in the resonance lines themselves which produces a characteristic sub-thermal source function that deepens the line (Reggiani et al., 2019). This simplification was a necessary trade-off to obtain line profiles across the entire simulation time series. In any case, test calculations indicated that this two-line atom differs from a comprehensive K I model atom with 134 levels and 250 bound-bound radiative transitions (Reggiani et al., 2019) by about 1 % in the depth of the 7698 Å line and with negligible differences in inferred radial velocities. Moreover, we rescaled the hydrodynamic simulations from a resolution of 240^3 to $120^2 \times 220$. We solve the statistical equilibrium by computing the monochromatic radiation field using 26 short characteristics (eight polar angles, and four azimuthal angles for each non-vertical ray), and typically find convergence after six accelerated lambda iterations. The emergent spectra are computed with 57 rays (seven outgoing polar angles, and eight azimuthal angles for each non-vertical ray), sampling the spectral line at a spectral resolution of $40\,\mathrm{m\,s^{-1}}$.

We adopted a solar abundance $A(\mathrm{K}) = 5.10$ as this produced good agreement with observations of the K I 7698 Å line, but did not fine-tune this value. Figure 4.4 demonstrates the spatially averaged, disk integrated K I line profiles computed with BALDER, which are in excellent agreement with the observed line profile. The calculations were carried out for every snapshot in the 3D solar simulation (2880 in total) to obtain the temporal evolution of the solar K I line. The location and shape of the line varies from snapshot to snapshot as a consequence of varying line-of-sight velocity fields in the line forming region.

Radial velocities are extracted from our theoretical K I lines in a way that is fully consistent with the BiSON observational setup. Under a magnetic field of 0.2 T, which is approximately the magnetic field strength imposed in the BiSON spectrometer (Brookes et al., 1978), the K I 7698 Å line is split into two components centred at $\lambda_- = 7698.8907$ Å and $\lambda_+ = 7699.0384$ Å due to the Zeeman effect. Assuming the apparatus holds a temperature of 400 K yields a thermal broadening of $400\,\mathrm{m\,s^{-1}}$for the two laboratory lines. Their Gaussian profiles are schematically shown in Fig. 4.4. We compute the convolution between the spatially and temporally averaged theoretical solar K I line profile and each of the laboratory lines:

$$\begin{aligned} F_\mathrm{B} &= f_\lambda * G_{\lambda_-} \\ F_\mathrm{R} &= f_\lambda * G_{\lambda_+}, \end{aligned} \tag{4.41}$$

and subsequently the normalised flux difference

$$\mathcal{R} = \frac{F_\mathrm{B} - F_\mathrm{R}}{F_\mathrm{B} + F_\mathrm{R}}, \tag{4.42}$$

where "*" is the convolution operator, f_λ is the solar flux spectrum and $G_{\lambda_{-(+)}}$ is the blue (red) component of laboratory potassium line after Zeeman splitting[3]. The normalised flux difference $\mathcal{R}$ is proportional to the radial velocity (Chaplin et al., 1996). In order to quantify the proportionality constant, we translate the averaged K I line back and forth in velocity space in steps of $3\,\mathrm{m\,s^{-1}}$. The aforementioned calculation (Eqs. (4.41) and (4.42)) is repeated each time to obtain the velocity shift as a function of $\mathcal{R}$, which is well described by a linear function

$$\mathfrak{v} = 3020.576\mathcal{R} - 556.903\ \mathrm{m\,s^{-1}}, \tag{4.43}$$

over the interval $[-500, 500]\,\mathrm{m\,s^{-1}}$. The slope of Eq. (4.43) is in good agreement with the proportionality constant used in BiSON[4], which is typically $3000\,\mathrm{m\,s^{-1}}$ (Chaplin et al., 1996), implying that our synthesised line profile describes the solar K I line in a realistic way.

The above procedure is identical to the means by which BiSON extracts radial velocity from the solar K I line. We therefore apply Eqs. (4.41)-(4.43) to every snapshot in the 3D solar simulation. The thus evaluated radial velocity $\mathfrak{v}$ as a function of time has the same physical meaning as what BiSON measures. The fluctuation of radial velocity is mainly caused by radial oscillations in the simulation box. We note that temporal variations of granulation also contribute to a velocity fluctuation. However, by performing a horizontal average over more than ten granules, the influence of granulation on velocity fluctuation largely cancels out (Asplund et al. 2000, Sect. 4.2). Finally, we apply a Fourier transform to the temporal evolution of $\mathfrak{v}$ into the frequency domain to obtain the radial velocity power spectrum presented in Fig. 4.5. The radial velocity amplitude of the dominant simulation mode is $81.6\,\mathrm{m\,s^{-1}}$ at frequency 3.299 mHz.

4.6.2 Simulating the SONG radial velocity signal

SONG is a high-resolution spectrograph that covers a broad wavelength range, 4400–6900 Å, containing thousands of spectral absorption lines. For computational reasons, it is not feasible to perform high-resolution 3D radiative transfer over such a broad wavelength range for our very long hydrodynamic time series. Instead, we develop a simplified method that relies on computing synthetic spectra for representative lines covering a range of atomic line properties.

First, in order to have a macroscopic perception of absorption lines in the wavelength region covered by SONG, we computed the strength of every atomic absorption line between 4400 and 6900 Å with the TurboSpectrum code (v15.1; Plez 2012) for the stellar parameters of the Sun and ϵ Tau, using an atomic linelist from the Vienna Atomic Line Database (VALD, Ryabchikova et al. 2015). Selecting only lines with a line strength $W_\lambda/\lambda \geq 10^{-5}$ (corresponding to an equivalent width $W_\lambda = 5\,\mathrm{m\AA}$

[3] We note that the magnitude of $G_{\lambda_{-(+)}}$ has no effect on our results, as it cancels out in Eq. (4.42)

[4] In practice, the diurnal change of the measured normalized flux difference $\mathcal{R}$ due to the rotation of the Earth is used to calibrate the proportionality constant. A third-order polynomial relation, calibrated on a daily basis, is used.

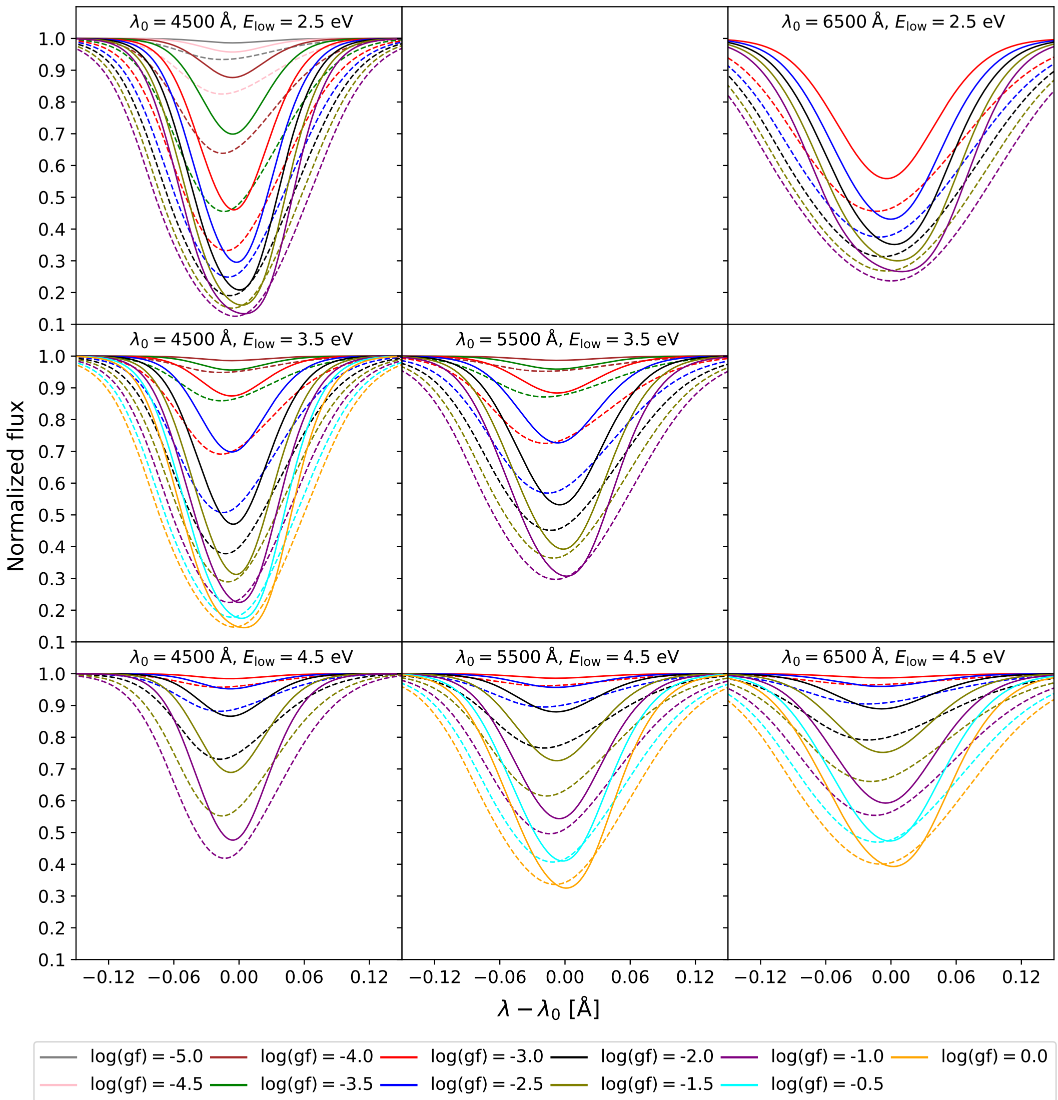

Figure 4.6: Spatially averaged Fe I line profiles of all line parameters tabulated in Table 4.3 computed from SCATE. Results from one example simulation snapshot are shown here for both the Sun (solid lines) and ϵ Tau (dashed lines). Reference wavelength λ_0 and $E_{\rm low}$ are marked in the figures, and log(gf) values are colour-coded as indicated in the legend. The top middle and middle right panels are left blank, because the corresponding $\{\lambda, E_{\rm low}\}$ combinations are not selected as representative line parameters (see Table 4.3).

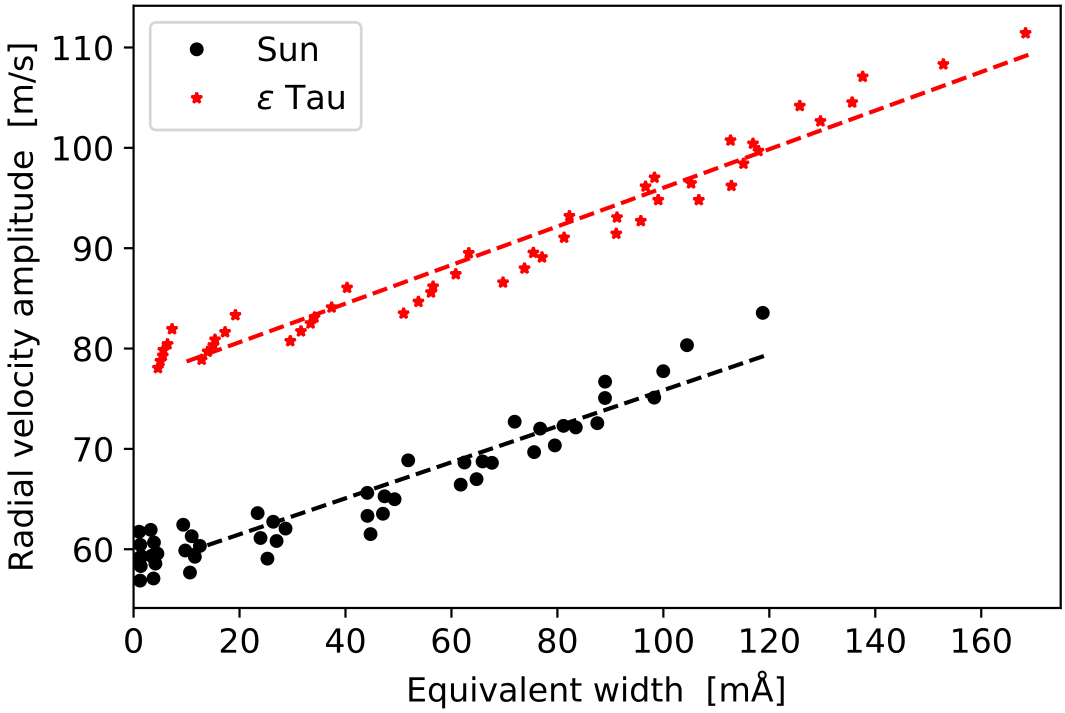

Figure 4.7: Radial velocity amplitude at the frequency of the dominant simulation mode evaluated from 49 fictitious Fe I lines are plotted against the equivalent width of these lines. Results from the solar and red giant simulations are shown in black dots and red asterisks, respectively. Linear fits to these data points are presented in dashed lines.

Table 4.3: Selected parameters of fictitious Fe I lines. Here log(gf) values are distributed in steps of 0.5. There are totally 49 lines covering typical Fe I lines in the Sun and ϵ Tau within the SONG wavelength range.

Wavelength (Å)	E_{low} (eV)	log(gf)
4500	2.5	$[-5, -1]$
	3.5	$[-4, 0]$
	4.5	$[-3, -1]$
5500	3.5	$[-4, -1]$
	4.5	$[-3, 0]$
6500	2.5	$[-3, -1]$
	4.5	$[-3, 0]$

at $\lambda = 5000\,\text{Å}$), we find a total of 4100 atomic lines for the Sun, and 7000 for ϵ Tau. Of these, 40 % are due to Fe I, and another 40 % are due to neutral species of other Fe-peak elements. These numbers are in good agreement with the list of lines identified over the same wavelength range in the spectrum of Arcturus by Hinkle et al. (2000). As the vast majority of spectral lines in the optical region are due to the neutral species of iron or elements with similar electron structure to iron, we use Fe I as a representative species.

The problem now is to determine a set of Fe I lines that can reasonably simulate SONG observations. The strength and shape of an absorption line is mainly governed by three parameters: the wavelength λ, which controls the background opacity due largely to H^-, the excitation potential of the lower ionization state $E_{\rm low}$, which determines the population of the level in LTE and thus the number of absorbers, and the oscillator strength $\log(\rm gf)$, which represents roughly the likelihood that a photon is absorbed by the line. It is therefore necessary to select representative values of λ, $E_{\rm low}$ and $\log(\rm gf)$ combinations, ensuring the corresponding artificial Fe I lines cover the properties of most observed Fe I lines. Firstly, we choose three wavelength ranges: 4400–4600 Å, 5400–5600 Å, and 6400–6600 Å. In a given wavelength region, we pick all Fe I lines with equivalent width greater than 10 mÅ from the aforementioned solar and ϵ Tau line lists. All selected lines from the two theoretical line lists are then classified into different groups based on their $E_{\rm low}$. For example, the thus determined typical $E_{\rm low}$ values for Fe I lines between 4400 and 4600 Å are 2.5, 3.5 and 4.5 eV. Next, for a given $E_{\rm low}$, we further select a set of $\log(\rm gf)$ values that span the entire $\log(\rm gf)$ range seen in the theoretical line list. The selection procedure gives 49 line parameter combinations listed in Table 4.3, which are reasonable representation of Fe I lines from the Sun and ϵ Tau between 4400 and 6900 Å.

We carry out 3D LTE line formation calculations for these 49 fictitious Fe I lines using the SCATE code (Hayek et al., 2011). In these high-resolution calculations, we tabulate continuum opacities and photon destruction probabilities for a set of temperatures and densitites and use these to compute the effects of continuum scattering at run time. Line opacities are likewise evaluated at run time, taking into account local velocity fields that produce Doppler shifts in the line profiles. Specific intensities are computed for 20 rays, along five different polar and four azimuthal angles; the former are distributed on a Gauss-Legendre quadrature and the latter are equidistant. We compute the spectral lines at high resolution, with a velocity step of just $40\,\rm m\,s^{-1}$, over a range $\pm 10\,\rm km\,s^{-1}$ that samples the entire line. We perform these calculations on each snapshot from the simulations of the Sun and ϵ Tau, and note that in the case of ϵ Tau, the Fe abundance used in the line formation calculation is adopted from the reference metallicity $[\rm Fe/H] = 0.15$. Example theoretical line profiles, i.e. the normalized emergent flux as a function of wavelength, computed from one simulation snapshot of the Sun and ϵ Tau are shown in Fig. 4.6. The theoretical lines in ϵ Tau are broader than the corresponding solar lines for all line parameters, due to the larger velocity field in red giant stars.

The line formation calculation introduced above gives the time evolution of all 49 fictitious Fe I lines, from which we can then extract the corresponding radial velocity variation. As reference, we use template spectra computed as the temporal averages from the two simulation sequences. For each $\{\lambda, E_{\rm low}, \log({\rm gf})\}$ combination, a certain theoretical Fe I line from a given snapshot is fitted to the template line profile using a χ^2 technique to obtain the wavelength shift $\Delta\lambda$ of this line. This method closely resembles the cross correlation technique often used in observational work (e.g. Butler et al., 1996).

The thus obtained radial velocity as a function of time is translated to the frequency domain through a Fourier transform, which gives radial velocity amplitude at the frequency of the dominant simulation mode. Radial velocity amplitudes for the 49 lines range from roughly 60 to 80 $\mathrm{m\,s^{-1}}$ in the solar case and 80–110 $\mathrm{m\,s^{-1}}$in the case of ϵ Tau, as shown in Fig. 4.7. The next question is how then to reliably determine a final radial velocity amplitude, given these 49 different values. Recall that strong absorption lines tend to form higher up in the stellar photosphere than weak lines (e.g. Rutten, 2003), where the velocity fields are typically larger due to the substantially smaller densities. It is therefore anticipated that the magnitude of radial velocity amplitude is correlated with the strength of the line, and Fig. 4.7 indeed follows an approximately linear relationship between the radial velocity amplitude and equivalent width for the Fe I lines considered for both stars.

We select from our theoretical line list every Fe I line in the SONG spectral range with equivalent width between 10 and 200 mÅ, and use our fitted linear relations to estimate the radial velocity variation amplitude for each line. We exclude weaker lines as these are unlikely to significantly influence the radial velocity determination in a real stellar spectrum. Very strong lines with $W_\lambda > 200$ mÅ are also excluded, because extrapolations to even higher equivalent width are not guaranteed to be reliable. In total, 1407 and 2224 lines are selected this way for the Sun and ϵ Tau, respectively. The ensemble of estimated radial velocity amplitudes are averaged to a final value, weighted by the equivalent width. The weighted average is performed with the understanding that the signal to noise ratio of weak lines is typically smaller than stronger lines, meaning a relatively larger error and thus a smaller influence on the final result (see Fig. 2 of Antoci et al. 2013).

Although the method developed here is not identical to the means by which SONG determines radial velocity from the observed spectra, it simulates the SONG observations sufficiently well. First, the set of fictitious Fe I lines carefully chosen in this work is able to represent the properties of most Fe I lines seen between 4400 and 6900 Å, which constitute a large part of all lines in this wavelength interval. Second, the procedure to extract radial velocity from theoretical spectral lines is similar to how radial velocities are typically obtained from observed spectra. Third, the evaluation of our final radial velocity amplitude includes the information of many spectral lines that span the whole range in observation. The major uncertainty in our method is associated with the linear relationship between radial velocity amplitude and equivalent width. Due to the complicated physical processes involved in spectral line formation in a 3D atmosphere (e.g. Asplund et al., 2000), it is difficult to quantify higher order effects beyond the linear relation between $\mathfrak{v}$ and W_λ; that is, the systematic uncertainty of the linear fitting. Nevertheless, it is still illuminating to

Table 4.4: Summary of predicted and observed oscillation amplitudes and amplitude ratios for the Sun and ϵ Tau. Here we emphasize again that individual oscillation amplitudes from 3D atmosphere simulations are not comparable to the corresponding observations (cf. Sect. 4.3 and 4.4).

Sun	Modelling	Observation
Bolometric (ppm)	1714.0 ± 3.0	3.58 ± 0.16 (a)
BiSON ($\mathrm{m\,s^{-1}}$)	81.6	0.187 ± 0.007 (b)
SONG ($\mathrm{m\,s^{-1}}$)	72.2 ± 0.5	0.166 ± 0.004 (c)
Bolometric/BiSON (ppm/[$\mathrm{m\,s^{-1}}$])	21.0 ± 0.04	19.1 ± 1.1
Bolometric/SONG (ppm/[$\mathrm{m\,s^{-1}}$])	23.7 ± 0.2	21.6 ± 1.1
ϵ Tau	Modelling	Observation
Bolometric (ppm)	3070.3 ± 7.4	—
K2 (ppm)	4515.1 ± 10.9	39.8 ± 1.4 (d)
SONG ($\mathrm{m\,s^{-1}}$)	93.2 ± 0.3	0.94 ± 0.04 (d)
K2/SONG (ppm/[$\mathrm{m\,s^{-1}}$])	48.4 ± 0.2	42.2 ± 2.3 (d)

Reference: (a): Michel et al. (2009); (b): Kjeldsen et al. (2008); (c): Fredslund Andersen et al. (2019); (d): Arentoft et al. (2019)

provide the statistical uncertainty. The statistical uncertainty is quantified using the bootstrap method. The data set considered here is the radial velocity amplitude and equivalent width of 49 fictitious Fe I lines. We conduct 10000 bootstrap samplings, that is, generating 10000 data sets each containing 49 randomly sampled $\mathfrak{v}$ and W_λ pairs. A linear regression between equivalent width and radial velocity is then performed for each re-sampled data set. For each fitting, we compute the equivalent width weighted mean radial velocity amplitude for all selected Fe I lines. The bootstrap method therefore results in 10000 weighted mean radial velocity amplitudes, their mean and variance is the desired final radial velocity amplitude and its statistical uncertainty, which is $72.2 \pm 0.5\,\mathrm{m\,s^{-1}}$ for the 3D solar model and $93.2 \pm 0.3\,\mathrm{m\,s^{-1}}$ for the ϵ Tau model.

4.7 Results

Our results, together with the corresponding observations, are summarised in Table 4.4.

The predicted ratio between luminosity and BiSON radial velocity amplitude at approximately 3.3 mHz is 1714.0 ppm $\div$ $81.6\,\mathrm{m\,s^{-1}} \approx 21.0$ ppm/[$\mathrm{m\,s^{-1}}$]. Observationally, the measured maximum bolometric amplitude per radial mode for the Sun is 3.58 ± 0.16 ppm according to Michel et al. (2009); the value presented in their paper is multiplied by $\sqrt{2}$ to convert the root mean square luminosity variation to luminosity amplitude. The peak radial velocity amplitude per radial mode measured by BiSON is $18.7 \pm 0.7\,\mathrm{cm\,s^{-1}}$ (Kjeldsen et al., 2008). Therefore, the amplitude ratio determined from observation is approximately 19.1 ± 1.1 ppm/[$\mathrm{m\,s^{-1}}$], in good agreement with the result predicted by our simulations. However, we caution that the above observed solar amplitude ratio is evaluated at the frequency of maximum power $\nu_{\max}$, that is, 3.1 mHz for the Sun (Kjeldsen et al., 2008), whereas our theoretical result is obtained at the frequency of the dominant simulation mode (3.3 mHz). The two values are hence not strictly comparable because amplitude ratio depends on frequency in principle. Nevertheless, the frequency dependence is weak, especially for frequencies near $\nu_{\max}$, as shown in detailed asteroseismic observations (for example, Fig. 13 of Arentoft et al. 2019). Therefore, as an initial effort to this topic, a single amplitude ratio value is likely to be sufficient to describe the relationship between luminosity and radial velocity variation for a given star.

The predicted ratio between luminosity and SONG radial velocity amplitudes (at approximately 3.3 mHz) is 23.7 ± 0.2 ppm/[m s^{-1}] for the Sun. We emphasise that the presented uncertainty reflects the combined statistical error of the granulation background fitting (Sect. 4.5.1) and the linear fit to radial velocities (Sect. 4.6.2). On the other hand, the measured solar maximum bolometric amplitude is 3.58 ± 0.16 ppm, whereas the maximum radial velocity amplitude obtained from SONG observations of the Sun is $16.6 \pm 0.4\,\mathrm{cm\,s^{-1}}$ (Fredslund Andersen et al., 2019). Together, the observed solar amplitude ratio is 21.6 ± 1.1 ppm/[m s^{-1}], being consistent with our theoretical result. For ϵ Tau, the amplitude ratio measured by Arentoft et al. (2019) is 42.2 ± 2.3 ppm/[m s^{-1}], which is the ratio between *K2* luminosity amplitude and the SONG radial velocity amplitude. The intrinsic luminosity amplitude computed from our simulations is 3070.3 ± 7.4 ppm at the frequency of the dominant simulation mode, and the conversion factor between intrinsic and *Kepler* luminosity amplitude is 0.68 for ϵ Tau as quantified in Sect. 4.5.2. According to Eq. (4.39), the theoretical luminosity amplitude in the *Kepler* band-pass turns out to be 4515.1 ± 10.9 ppm. Dividing this value by the theoretical SONG radial velocity amplitude gives the predicted amplitude ratio between *Kepler* (*K2*) and SONG for ϵ Tau, which is 48.4 ± 0.2 ppm/[m s^{-1}]. Again, we find reasonable agreement between our theoretical calculations and the observations.

We note that the amplitude ratio estimated from the widely used empirical relationship of Kjeldsen & Bedding (1995, their Eq. 5) is 23.2 ppm/[m s^{-1}] for ϵ Tau, being significantly lower than the observed value by almost a factor of two. The good agreement between observation and our theoretical result based on detailed modelling therefore shows great potential to accurately quantify the relationship between luminosity and radial velocity amplitude, especially for red giant stars where the empirical amplitude ratio relation may fail. Nonetheless, we are aware that our predicted ratios are systematically larger than corresponding observations by about 10%. The underlying reason for this small discrepancy is not entirely clear and will be investigated in future work.

4.8 Conclusions

In this work, we investigated the relationship between photometric and spectroscopic measurements of solar-like oscillations using 3D radiative-hydrodynamical stellar atmosphere simulations with the Stagger code. We used as test cases the Sun and the Hyades red giant ϵ Tau. Our simulations provide realistic descriptions of fluid motions from first principles, hence naturally yield compressible effects such as sound waves. Although sound waves emerging in the simulation domain are analogous to p-modes in solar-type oscillating stars, the simulation modes have much larger oscillation amplitudes than observed stellar p-modes due to the limited extent of simulation box. Therefore, we first analytically demonstrated that 3D simulations are still able to reliably predict the ratio between luminosity and velocity amplitudes, despite the individual amplitude values not being comparable with observations.

Having established the basis of our analysis, we computed the spectrum of luminosity variation based on bolometric fluxes predicted by the state-of-the-art radiative transfer module in our simulation. Contribution from the granulation background was modelled in a way similar to what is applied to real observations. The modelled granulation background was then subtracted from the luminosity spectrum to obtain the intrinsic luminosity amplitude of the dominant simulation mode. To enable comparison with amplitudes measured with a given spacecraft, it was necessary to quantify the conversion factor (also called bolometric correction) between the intrinsic and measured luminosity amplitudes. We adopted the theoretical formulation of Michel et al. (2009), Ballot et al. (2011) and Lund (2019) for the evaluation of the conversion factor, whose components are consistently computed via 3D spectrum synthesis using the code scate. As an initial step, we evaluated the conversion factor between intrinsic and *Kepler* luminosity amplitude for the two stars studied in this work. For ϵ Tau, our result differs from Lund (2019) by roughly 10%, implying that the conversion factors of red giant stars are likely to be sensitive to the choice of model atmosphere.

In turn, we have developed novel methods to simulate the spectroscopic measurement of stellar oscillations from numerical simulations for the first time. Theoretical radial velocities are obtained from realistic spectral line formation calculations with 3D time-dependent atmosphere models as input. In order to simulate BiSON, which measures solar oscillations through the K i line, we performed detailed 3D non-LTE K i line formation calculations with balder for our solar model atmosphere. The computed K i line profile is in excellent agreement with observation, its temporal evolution (that is, Doppler shift) gives radial velocities whose physical meaning is identical to what measured by BiSON. In addition, we carried out 3D LTE line formation calculations for a large set of fictitious Fe i lines using scate to simulate SONG observations which determines radial velocities from a forest of absorption lines between 4400 and 6900 Å. The parameters of the chosen Fe i lines were carefully selected such that their properties cover most lines typically seen in the Sun and a warm giant within the SONG wavelength range. For each selected line, radial velocities were extracted according to the Doppler shift of line profiles with method that resemble observations. This procedure was repeated for all selected lines, thereby giving rise to a set of independent radial velocity amplitudes. With the insight that the radial velocity amplitude computed from a certain line is correlated with its strength, we fit a linear function between radial velocity amplitude and equivalent width based on results from all selected fictitious lines. The linear relation was further used to estimate radial velocity amplitudes for all visible lines within the SONG wavelength range in our theoretical line list, which were subsequently reduced to a final radial velocity amplitude value via weighted average.

In concert, the calculations gave us the ratio between luminosity and radial velocity amplitude, which characterize the relationship between photometric and spectroscopic measurement of stellar oscillations. Given the 3D atmosphere simulations and line formation calculations presented in this work, our approach to quantify the amplitude ratio is free from any empirical parameters that have to be assumed or calibrated from observations. The *ab initio* nature of our numerical modelling therefore not only reveals the underlying physics behind asteroseismic observations but also enables an independent comparison between theoretical results and observed amplitude ratio. For the Sun, our theoretical bolometric and BiSON ratio as well as bolometric and SONG ratio are compared with helioseismic observations with good agreements, thus validate our numerical approach. In the case of ϵ Tau, the predicted ratio between *K2* and SONG amplitude matches corresponding observations as well, which is particularly encouraging as the observed amplitude ratio of this star cannot be explained by the widely used empirical amplitude ratio scaling relation. The good theoretical–observational consistency achieved for both the Sun and a red giant star suggested that our method of connecting the luminosity and radial velocity measurements of solar-like oscillations is robust, effective, and likely applicable to a wide range of stellar parameters. This demonstrates great potential in the era of simultaneous observations of stellar oscillation with both space-photometry (such as TESS) and ground-based spectroscopy (such as SONG).

In the future we plan to extend our analysis to cover the parameter space of solar-like oscillating stars across the HR diagram (i.e. dwarfs, subgiants and red giants), which will give amplitude ratios as a function of basic stellar parameters. These theoretical amplitude ratios can provide valuable insight to asteroseismic observations by helping to determine whether a star is better observed in photometry or spectroscopy. Conversely, it is possible to determine radial velocity oscillation amplitude from *Kepler* or TESS data through the theoretical amplitude ratio relation, thereby quantifying the oscillation part of the so-called "radial velocity jitter" (see Yu et al. 2018 for a pioneering study in this direction) which is of great importance in exoplanet science.

Chapter 5

Conclusions

5.1 Summary of thesis

Asteroseismology of solar-type stars has thrived thanks to the CoRoT, *Kepler* and TESS space missions, which have detected solar-like oscillations in thousands of stars. With more detailed asteroseismic observations available, it is important to fully understand how oscillations are driven and dissipated in solar-type stars. This thesis has made substantial contributions to this long-standing problem from a theoretical perspective. By using state-of-the-art 3D hydrodynamical simulations of stellar surface convection, I have been able to quantify the excitation and damping processes of solar-like oscillations from first principles, which then allows for the prediction of oscillation amplitude and the frequency of maximum power, $\nu_{\rm max}$, for the first time. The numerical method developed in this thesis is free from tunable free parameters adopted in previous investigations, thereby providing valuable physical insights into the stochastic excitation of solar-type oscillations. Meanwhile, the ability to predict the important asteroseismic observable $\nu_{\rm max}$ achieved in this thesis opens the exciting prospect of examining the widely used seismic scaling relation from detailed modelling of stellar oscillations.

Using such 3D surface convection simulations, I also investigated the relationship between photometric and spectroscopic measurements of solar-like oscillations. For both the Sun and the red giant ϵ Tau analysed in this initial study, I find good agreement between the theoretically predicted and observed amplitude ratio. This pioneering work not only reveals the underlying physics of asteroseismic observations, but also shows great potential of bridging two different measurements of stellar oscillation using 3D atmosphere models.

5.1.1 Quantifying the excitation and damping of solar-like oscillations

For the excitation rate, I adopted the theoretical framework developed by Nordlund & Stein (2001) and Stein & Nordlund (2001). Components in the expression of excitation rate were evaluated from 3D simulations as well as the stellar oscillation calculation. The numerical results demonstrated that mode excitation is weak at low frequencies, then increases with frequency to a plateau[1] that contains $\nu_{\max}$ before slightly declining at higher frequencies. It was also verified that mode excitation stems from the coupling between convection-induced pressure fluctuation and pulsation-induced fluid compression. Excitation rates computed from the solar simulation are consistent with previous theoretical investigation (e.g., Stein & Nordlund 2001) and corresponding helioseismic observations.

In order to extract reliable damping rates from 3D simulations, it is necessary to separate the density fluctuation $\delta\rho$ caused by pulsation from "convective noise." To this end, I carried out artificial mode-driving simulations where a target radial oscillation is artificially driven to large amplitude so that $\delta\rho$ at the driving frequency results predominantly from pulsation. Theoretical damping rates at each frequency were computed from such numerical experiments and compared in detail with observed frequency-dependent line widths. Encouraging agreement was achieved between simulations and observation: For all five stars investigated, the numerical damping rates are of the same order of magnitude as the corresponding measured values, and in most cases the $\eta - \nu$ relation matches observation. This validates our numerical approach for calculating the damping rate for radial modes.

There is no doubt that the development and application of 1D non-local time-dependent MLT convection models (Gough, 1977; Balmforth, 1992a; Gabriel, 1996; Grigahcène et al., 2005) have enriched our understanding of the mode stability problem remarkably. The damping rates computed based on these 1D non-local time-dependent models also agree well with the observed linewidth for the Sun and other solar-like oscillating stars (see e.g., Houdek et al. 2019). Nevertheless, the 1D calculation involves adjustable parameters that need to be calibrated from 3D simulations and observational data. For example, the non-local time-dependent convection model developed by Gough (1977) contains free parameters a, b, c and Φ, where a is relevant to the convective flux, b controls the degree to which the turbulent fluxes are coupled to the local stratification, c affects the momentum flux, and Φ describes the anisotropy of the convective velocity field. In practice, the parameters c and Φ are calibrated from the corresponding 3D surface convection simulation while a and b are adjusted to achieve a best fit between theoretical and observed linewidth (Houdek et al., 2019). On the other hand, theoretical damping rates calculated based on 3D simulations with the numerical method developed in this thesis do not rely on any adjustable parameters other than those used to specify the artificial driving. This thus allows, for the first time, independent comparisons between observed linewidth and theoretical predictions.

With both mode excitation and damping rates extracted from the model, it is possible to predict the theoretical velocity spectrum, from which $\nu_{\max}$ can be estimated. The velocity amplitude is obtained by assuming exact balance between energy gain from stochastic excitation and energy loss by linear damping. Based on the synthetic velocity amplitude, I report, to my knowledge, the first purely theoretical $\nu_{\max}$

[1] It is worth noting that such plateau is not observed by Stein et al. (2004), who computed the excitation rates for several F, G and K type stars based on their 3D models. This difference between Stein et al. (2004) and this work is not clear and will be investigated in detail.

estimations for solar-like oscillating stars. I compared my results against the corresponding observations. In particular, the estimated $\nu_{\max}$ is consistent overall with measured values. This finding foreshadows exciting opportunities for predicting this important asteroseismic observable for solar-type oscillators from first principles using 3D hydrodynamical simulations.

Studying several stars also allows for comparison between excitation/damping rates and fundamental stellar parameters. Qualitative relationships between $\mathcal{P}_{\mathrm{exc}}$, η, $\nu_{\max}$ and T_{eff}, g were found from the simulations. Namely, both excitation and damping rates are positively correlated with the effective temperature, which accords with empirical relations derived from other theoretical investigations (Samadi et al., 2007) and those summarised from observations (Chaplin et al., 2009). Meanwhile, theoretical $\nu_{\max}$ values estimated from our simulations broadly obey the $\nu_{\max}$ scaling relation, reaffirming it at solar-metallicity.

5.1.2 Quantifying the relationship between photometric and spectroscopic oscillation amplitudes

As an initial study of this topic, I used as test cases the Sun and the Hyades red giant ϵ Tau. Although sound waves emerging in the simulation domain are analogous to p-modes in solar-type oscillating stars, the simulation modes have much larger oscillation amplitudes than observed stellar p-modes due to the limited extent of simulation box. Therefore, I first analytically demonstrated that 3D simulations are still able to reliably predict the ratio between luminosity and velocity amplitudes, despite the individual amplitude values not being comparable with observations.

I then computed the spectrum of luminosity variation based on bolometric fluxes predicted by the state-of-the-art radiative transfer module in our simulation. The contribution from the granulation background was modelled in a way similar to what is applied to real observations. The modelled granulation background was then subtracted from the luminosity spectrum to obtain the intrinsic luminosity amplitude of the dominant simulation mode. To enable comparison with amplitudes measured with a given spacecraft, it was necessary to quantify the conversion factor (also called bolometric correction) between the intrinsic and measured luminosity amplitudes. I adopted the theoretical formulation of Michel et al. (2009), Ballot et al. (2011) and Lund (2019) for the evaluation of the conversion factor, whose components are consistently computed via 3D spectrum synthesis using the code SCATE. As an initial step, I evaluated the conversion factor between intrinsic and *Kepler* luminosity amplitude for the Sun and ϵ Tau.

In turn, I have developed novel methods to simulate the spectroscopic measurement of stellar oscillations from numerical simulations for the first time. Theoretical radial velocities are obtained from realistic spectral line formation calculations with 3D time-dependent atmosphere models as input. In order to simulate BiSON, which measures solar oscillations through the K I line, I performed detailed 3D non-LTE K I line formation calculations with BALDER for our solar model atmosphere. The computed K I line profile is in excellent agreement with observation, its temporal evolution (that is, Doppler shift) gives radial velocities whose physical meaning is identical to that measured by BiSON. In addition, I carried out 3D LTE line formation calculations for a large set of synthetic Fe I lines using SCATE to simulate SONG observations, which determines radial velocities from a forest of absorption lines between 4400 and 6900 Å.

In concert, the calculations yield the ratio between luminosity and radial velocity amplitude, which characterizes the relationship between photometric and spectroscopic measurements of stellar oscillations. For the Sun, the theoretical bolometric and BiSON ratio, as well as the bolometric and SONG ratio, are compared with helioseismic observations with good agreements, thus validating my numerical approach. In the case of ϵ Tau, the predicted ratio between *K2* and SONG amplitudes matches corresponding observations as well, which is particularly encouraging as the observed amplitude ratio of this star cannot be explained by the widely used empirical amplitude ratio scaling relation. The good theoretical–observational consistency achieved for both the Sun and a red giant star suggested that my method of connecting the luminosity and radial velocity measurements of solar-like oscillations is robust, effective, and likely applicable to a wide range of stellar parameters. This demonstrates great potential in the era of simultaneous observations of stellar oscillation with both space-photometry (such as TESS) and ground-based spectroscopy (such as SONG).

5.2 Future Work

Although I have made notable progress on quantifying the excitation/damping rate and velocity amplitude with 3D simulations, I caution that disagreements do exist between simulations and observations. For example, for Procyon, it seems that 3D simulations overestimate excitation rates. At lower frequencies, the models tend to underestimate damping rates due to the limited simulation domain. This suggests that there is room for improvement to the numerical methods or indicates the necessity of more detailed numerical simulations. In the future, I plan to carry out more detailed 3D surface (magneto-)convection simulations with higher numerical resolution and deeper vertical coverage, as their attributes can be helpful towards improving the agreement between theory and observation (Sect. 3.6.2). Meanwhile, a larger number of such simulations that covers adequate parameter combinations (e.g. $\{T_{\text{eff}}, \log g, [\text{Fe/H}]\}$) could be used to quantify the relationship between mode excitation/damping and fundamental stellar parameters. I note that several works have suggested corrections to the widely-used $\nu_{\max}$ scaling relation (Belkacem et al., 2011, 2013; Viani et al., 2017). For example, Belkacem et al. (2011, 2013) recommended that the $\nu_{\max}$ scaling relation should have a non-linear Mach number dependence:

$$\nu_{\max} \propto \mathcal{M}_a^3 \nu_{\text{ac}}, \tag{5.1}$$

where $\mathcal{M}_a$ and ν_{ac} are Mach number and acoustic cut-off frequency, respectively. It will be worthwhile to test the proposed correction using 3D hydrodynamical simulations for solar-like oscillators across the HR diagram. In particular, I am interested in extending my analysis to cover red giant stars with a wide range of metallicities, as these make up the bulk of the *Kepler* and TESS surveys. As red giant stars are intrinsically bright, they are visible at great distances and are thus critical probes of the whole Milky Way galaxy; the possibility to accurately measure their interior structure, composition, mass, and age by means of asteroseismology is of major importance for Galactic archaeology.

I have also demonstrated in this thesis that it is possible to accurately quantify the relationship between photometric and spectroscopic oscillation amplitudes using 3D simulations. As a continuation of this project, I plan to extend such analysis to cover the parameter space of solar-like oscillating stars across the HR diagram (i.e. dwarfs, subgiants and red giants), which will give amplitude ratios as a function of basic stellar parameters. These theoretical amplitude ratios can provide valuable insight to asteroseismic observations by helping to determine whether a star is better observed via photometry or spectroscopy. Conversely, it is possible to determine radial velocity oscillation amplitude from *Kepler* or TESS data through the theoretical amplitude ratio relation, thereby quantifying the oscillation part of the so-called "radial velocity jitter" (see Yu et al. 2018 for a pioneering study in this direction). This is of great importance in exoplanet science.

In this thesis, I focus mainly on quantifying the amplitude of solar-like oscillations. Nevertheless, 3D stellar surface convection simulations can be applied to study various other asteroseismic problems: It was shown that 3D simulations are a promising solution to the asteroseismic surface effect (e.g. Trampedach et al. 2017; Jørgensen et al. 2017). The asteroseismic surface effect, which is briefly mentioned in Sect. 1.2.1, refers to the discrepancy between observed and predicted p-mode oscillation frequencies at high frequencies in solar-type stars, which is due to the inadequate description of the outer stellar convection zone and atmospheric structure by traditional 1D models, as well as the adiabatic assumption when computing theoretical oscillation frequencies. It is one of the most important problems in asteroseismology, as the surface effect significantly limited the potential of utilizing measured oscillation frequencies to constrain the interior structure of stars. By replacing the outer layers of 1D models with corresponding averaged 3D models, the surface effect can be reduced because of the refined near-surface structure. This solves the so-called "structural effect". The remaining discrepancy arises from the adiabatic assumption when computing oscillation frequencies: high-frequency modes are generally non-adiabatic, therefore their true frequency differs from those calculated with adiabatic approximation. This is the so-called "modal effect". The modal effect is believed to be equally important as the structural effect (Houdek et al., 2017), but it is still not thoroughly studied. I plan to quantify the frequency shift caused by non-adiabatic effects using 3D simulations in the near future. I note that the non-adiabatic frequency shift can be computed in a way that is very similar to the linear damping rate. I plan to start from the Sun then extend to other benchmark stars and Stagger-grid models

(Magic et al., 2013a). The goal is to quantify both structural and modal effect from 3D simulations for a variety of stars covering a broad range of $T_{\rm eff}$, $\log g$ and [Fe/H] and propose a correction formula with solid physical bases.

Bibliography

Aerts, C. 2021, Reviews of Modern Physics, 93, 015001 (cited on page 2)

Aerts, C., Christensen-Dalsgaard, J., & Kurtz, D. W. 2010, Asteroseismology (cited on pages xi, 2, 4, 5, 6, 8, 10, 29, 34, 39, 43, 46, 72, 83, 84, 85, 86, 103, and 104)

Allende Prieto, C., Asplund, M., García López, R. J., & Lambert, D. L. 2002, ApJ, 567, 544 (cited on page 51)

Amarsi, A. M., Asplund, M., Collet, R., & Leenaarts, J. 2016a, MNRAS, 455, 3735 (cited on page 114)

Amarsi, A. M., Lind, K., Asplund, M., Barklem, P. S., & Collet, R. 2016b, MNRAS, 463, 1518 (cited on pages 55 and 114)

Amarsi, A. M., Nordlander, T., Barklem, P. S., et al. 2018, A&A, 615, A139 (cited on page 114)

Ando, H., & Osaki, Y. 1975, PASJ, 27, 581 (cited on page 8)

Antoci, V., Handler, G., Grundahl, F., et al. 2013, MNRAS, 435, 1563 (cited on pages 114 and 122)

Applegate, J. H. 1988, ApJ, 329, 803 (cited on page 1)

Appourchaux, T., Belkacem, K., Broomhall, A.-M., et al. 2010, A&A Rev, 18, 197 (cited on page 5)

Appourchaux, T., Benomar, O., Gruberbauer, M., et al. 2012, A&A, 537, A134 (cited on pages 48 and 77)

Appourchaux, T., Antia, H. M., Benomar, O., et al. 2014, A&A, 566, A20 (cited on pages 80 and 81)

Arentoft, T., Kjeldsen, H., Bedding, T. R., et al. 2008, ApJ, 687, 1180 (cited on pages xiv, xix, 9, 51, 52, and 67)

Arentoft, T., Grundahl, F., White, T. R., et al. 2019, A&A, 622, A190 (cited on pages xix, 96, 97, 98, 123, and 124)

Asplund, M., Grevesse, N., Sauval, A. J., & Scott, P. 2009, ARA&A, 47, 481 (cited on pages 20, 27, 55, and 99)

Asplund, M., Nordlund, Å., Trampedach, R., Allende Prieto, C., & Stein, R. F. 2000, A&A, 359, 729 (cited on pages 20, 28, 114, 118, and 122)

Aufdenberg, J. P., Ludwig, H. G., & Kervella, P. 2005, ApJ, 633, 424 (cited on pages 50, 51, and 52)

Baines, E. K., Armstrong, J. T., Schmitt, H. R., et al. 2018, AJ, 155, 30 (cited on page 97)

Ball, W. H., Beeck, B., Cameron, R. H., & Gizon, L. 2016, A&A, 592, A159 (cited on page 20)

Ballot, J., Barban, C., & van't Veer-Menneret, C. 2011, A&A, 531, A124 (cited on pages 110, 125, and 129)

Balmforth, N. J. 1992a, MNRAS, 255, 603 (cited on pages 11, 25, 48, 51, 80, 81, and 128)

—. 1992b, MNRAS, 255, 639 (cited on pages 11 and 48)

Barklem, P. S., Anstee, S. D., & O'Mara, B. J. 1998, PASA, 15, 336 (cited on page 117)

Basu, S., & Antia, H. M. 1995, MNRAS, 276, 1402 (cited on page 9)

—. 1997, MNRAS, 287, 189 (cited on pages 9, 24, and 48)

Basu, S., Chaplin, W. J., Elsworth, Y., New, R., & Serenelli, A. M. 2009, ApJ, 699, 1403 (cited on pages 4 and 24)

Basu, S., Christensen-Dalsgaard, J., Chaplin, W. J., et al. 1997, MNRAS, 292, 243 (cited on page 34)

Beck, P. G., Montalban, J., Kallinger, T., et al. 2012, Nature, 481, 55 (cited on page 24)

Bedding, T. R., & Kjeldsen, H. 2003, PASA, 20, 203 (cited on page 10)

Bedding, T. R., Kjeldsen, H., Butler, R. P., et al. 2004, ApJ, 614, 380 (cited on page 10)

Bedding, T. R., Kjeldsen, H., Reetz, J., & Barbuy, B. 1996, MNRAS, 280, 1155 (cited on page 72)

Bedding, T. R., Butler, R. P., Kjeldsen, H., et al. 2001, ApJL, 549, L105 (cited on pages 10, 14, 52, and 96)

Bedding, T. R., Kjeldsen, H., Arentoft, T., et al. 2007, ApJ, 663, 1315 (cited on pages xiii, xiv, 51, 52, 61, 64, and 68)

Bedding, T. R., Kjeldsen, H., Campante, T. L., et al. 2010, ApJ, 713, 935 (cited on pages xiii, xiv, 9, 51, 52, 61, 63, and 71)

Belkacem, K., Dupret, M. A., Baudin, F., et al. 2012, A&A, 540, L7 (cited on pages 11, 48, and 87)

Belkacem, K., Goupil, M. J., Dupret, M. A., et al. 2011, A&A, 530, A142 (cited on pages 24, 90, and 130)

Belkacem, K., Kupka, F., Samadi, R., & Grimm-Strele, H. 2019, A&A, 625, A20 (cited on pages 45, 49, 101, and 110)

Belkacem, K., Samadi, R., Goupil, M. J., et al. 2010, A&A, 522, L2 (cited on page 24)

Belkacem, K., Samadi, R., Mosser, B., Goupil, M.-J., & Ludwig, H.-G. 2013, in Astronomical Society of the Pacific Conference Series, Vol. 479, Progress in Physics of the Sun and Stars: A New Era in Helio- and Asteroseismology, ed. H. Shibahashi & A. E. Lynas-Gray, 61 (cited on page 130)

Bergemann, M., Lind, K., Collet, R., Magic, Z., & Asplund, M. 2012, MNRAS, 427, 27 (cited on pages 50 and 51)

Böhm-Vitense, E. 1958, Zeitschrift für Astrophysik, 46, 108 (cited on page 16)

Bonanno, A., Corsaro, E., Del Sordo, F., et al. 2019, A&A, 628, A106 (cited on page 74)

Borucki, W. J., Koch, D., Basri, G., et al. 2010, Science, 327, 977 (cited on pages 7, 24, 48, and 96)

Botnen, A., & Carlsson, M. 1999, Astrophysics and Space Science Library, Vol. 240, Multi3D, 3D Non-LTE Radiative Transfer, ed. S. M. Miyama, K. Tomisaka, & T. Hanawa, 379 (cited on page 114)

Bouchy, F., & Carrier, F. 2001, A&A, 374, L5 (cited on page 10)

—. 2003, Ap&SS, 284, 21 (cited on pages 10 and 52)

Brandão, I. M., Doğan, G., Christensen-Dalsgaard, J., et al. 2011, A&A, 527, A37 (cited on pages 50 and 52)

Bressan, A., Marigo, P., Girardi, L., et al. 2012, MNRAS, 427, 127 (cited on page 16)

Brookes, J. R., Isaak, G. R., & van der Raay, H. B. 1978, MNRAS, 185, 1 (cited on page 117)

Brown, T. M., Gilliland, R. L., Noyes, R. W., & Ramsey, L. W. 1991, ApJ, 368, 599 (cited on pages 9, 12, 14, 24, 47, 52, 77, 96, and 97)

Bruls, J. H. M. J., Rutten, R. J., & Shchukina, N. G. 1992, A&A, 265, 237 (cited on page 114)

Bruntt, H., Bedding, T. R., Quirion, P. O., et al. 2010, MNRAS, 405, 1907 (cited on pages 50 and 51)

Bruntt, H., Basu, S., Smalley, B., et al. 2012, MNRAS, 423, 122 (cited on pages 49 and 50)

Butler, R. P., Marcy, G. W., Williams, E., et al. 1996, PASP, 108, 500 (cited on pages 114 and 122)

Canuto, V. M., & Mazzitelli, I. 1991, ApJ, 370, 295 (cited on page 16)

Casagrande, L., Silva Aguirre, V., Schlesinger, K. J., et al. 2016, MNRAS, 455, 987 (cited on pages 12 and 78)

Castelli, F., & Kurucz, R. L. 2003, in IAU Symposium, Vol. 210, Modelling of Stellar Atmospheres, ed. N. Piskunov, W. W. Weiss, & D. F. Gray, A20 (cited on page 112)

Chaplin, W. J., Elsworth, Y., Isaak, G. R., et al. 1998, MNRAS, 298, L7 (cited on pages xii, 37, 38, 40, and 42)

Chaplin, W. J., Elsworth, Y., Isaak, G. R., Miller, B. A., & New, R. 2000, MNRAS, 313, 32 (cited on page 74)

Chaplin, W. J., Houdek, G., Elsworth, Y., et al. 2005, MNRAS, 360, 859 (cited on pages xv, 25, 42, 71, 93, and 94)

Chaplin, W. J., Houdek, G., Karoff, C., Elsworth, Y., & New, R. 2009, A&A, 500, L21 (cited on pages 48, 77, 82, and 129)

Chaplin, W. J., Elsworth, Y., Howe, R., et al. 1996, SoPh, 168, 1 (cited on pages 9, 96, 113, 114, and 118)

Chaplin, W. J., Kjeldsen, H., Christensen-Dalsgaard, J., et al. 2011, Science, 332, 213 (cited on page 13)

Chiavassa, A., Casagrande, L., Collet, R., et al. 2018, Astronomy and Astrophysics, 611, A11 (cited on page 114)

Christensen-Dalsgaard, J. 1989, MNRAS, 239, 977 (cited on page 43)

—. 2002, Reviews of Modern Physics, 74, 1073 (cited on page 9)

—. 2008, Ap&SS, 316, 113 (cited on pages 35 and 61)

Christensen-Dalsgaard, J., Duvall, T. L., J., Gough, D. O., Harvey, J. W., & Rhodes, E. J., J. 1985, Nature, 315, 378 (cited on page 9)

Christensen-Dalsgaard, J., & Gough, D. O. 1982, MNRAS, 198, 141 (cited on page 43)

Christensen-Dalsgaard, J., Gough, D. O., & Thompson, M. J. 1991, ApJ, 378, 413 (cited on page 9)

Christensen-Dalsgaard, J., Dappen, W., Ajukov, S. V., et al. 1996, Science, 272, 1286 (cited on pages 16 and 34)

Claverie, A., Isaak, G. R., McLeod, C. P., van der Raay, H. B., & Cortes, T. R. 1979, Nature, 282, 591 (cited on pages 9, 14, and 96)

Collet, R., Nordlund, Å., Asplund, M., Hayek, W., & Trampedach, R. 2018, MNRAS, 475, 3369 (cited on pages 18, 19, 25, 53, 99, and 100)

Cyburt, R. H., Amthor, A. M., Ferguson, R., et al. 2010, ApJS, 189, 240 (cited on page 58)

Davies, G. R., Broomhall, A. M., Chaplin, W. J., Elsworth, Y., & Hale, S. J. 2014, MNRAS, 439, 2025 (cited on pages xv, 93, and 94)

Deheuvels, S., Brandão, I., Silva Aguirre, V., et al. 2016, A&A, 589, A93 (cited on pages 24 and 48)

Deubner, F. L. 1975, A&A, 44, 371 (cited on page 9)

Dotter, A., Conroy, C., Cargile, P., & Asplund, M. 2017, ApJ, 840, 99 (cited on page 58)

Doğan, G., Bonanno, A., Bedding, T. R., et al. 2010, Astronomische Nachrichten, 331, 949 (cited on page 52)

Dravins, D. 2008, A&A, 492, 199 (cited on pages xvii and 115)

Dupret, M. A., Grigahcène, A., Garrido, R., Gabriel, M., & Scuflaire, R. 2005, A&A, 435, 927 (cited on page 7)

Dupret, M. A., Belkacem, K., Samadi, R., et al. 2009, A&A, 506, 57 (cited on page 11)

Epstein, C. R., Elsworth, Y. P., Johnson, J. A., et al. 2014, ApJL, 785, L28 (cited on page 13)

Frandsen, S., Carrier, F., Aerts, C., et al. 2002, A&A, 394, L5 (cited on page 10)

Fredslund Andersen, M., Pallé, P., Jessen-Hansen, J., et al. 2019, A&A, 623, L9 (cited on pages 123 and 124)

Freytag, B., Steffen, M., Ludwig, H. G., et al. 2012, Journal of Computational Physics, 231, 919 (cited on page 18)

Fuller, G. M., Fowler, W. A., & Newman, M. J. 1985, ApJ, 293, 1 (cited on page 58)

Gabriel, M. 1996, Bulletin of the Astronomical Society of India, 24, 233 (cited on pages 11 and 128)

GarcÍa, R. A., Régulo, C., Turck-Chièze, S., et al. 2001, SoPh, 200, 361 (cited on pages xi and 26)

Gelly, B., Lazrek, M., Grec, G., et al. 2002, A&A, 394, 285 (cited on pages xi and 26)

Goldreich, P., & Keeley, D. A. 1977a, ApJ, 211, 934 (cited on page 11)

—. 1977b, ApJ, 212, 243 (cited on pages 9, 11, 24, and 48)

Goldreich, P., Murray, N., & Kumar, P. 1994, ApJ, 424, 466 (cited on pages 11, 24, and 29)

Gough, D. 1985, SoPh, 100, 65 (cited on page 9)

Gough, D. O. 1977, ApJ, 214, 196 (cited on pages 11 and 128)

Grec, G., Fossat, E., & Pomerantz, M. 1980, Nature, 288, 541 (cited on page 9)

Grigahcène, A., Dupret, M. A., Gabriel, M., Garrido, R., & Scuflaire, R. 2005, A&A, 434, 1055 (cited on pages 7, 11, and 128)

Grundahl, F., Kjeldsen, H., Frandsen, S., et al. 2006, Memorie della Società Astronomica Italiana, 77, 458 (cited on pages 14, 48, 96, and 113)

Grundahl, F., Fredslund Andersen, M., Christensen-Dalsgaard, J., et al. 2017, ApJ, 836, 142 (cited on page 114)

Guenther, D. B., Demarque, P., & Gruberbauer, M. 2014, ApJ, 787, 164 (cited on page 52)

Gustafsson, B., Edvardsson, B., Eriksson, K., et al. 2008, A&A, 486, 951 (cited on pages 16, 53, and 99)

Guzik, J. A., Kaye, A. B., Bradley, P. A., Cox, A. N., & Neuforge, C. 2000, ApJL, 542, L57 (cited on page 7)

Hansen, C. J., Kawaler, S. D., & Trimble, V. 2004, Stellar interiors : physical principles, structure, and evolution (cited on pages 2 and 105)

Harvey, J. 1985, in ESA Special Publication, Vol. 235, Future Missions in Solar, Heliospheric & Space Plasma Physics, ed. E. Rolfe & B. Battrick, 199 (cited on page 108)

Hayek, W., Asplund, M., Carlsson, M., et al. 2010, A&A, 517, A49 (cited on pages 19, 27, 53, 99, and 112)

Hayek, W., Asplund, M., Collet, R., & Nordlund, Å. 2011, A&A, 529, A158 (cited on pages 112 and 121)

Heiter, U., Jofré, P., Gustafsson, B., et al. 2015, A&A, 582, A49 (cited on pages 50 and 52)

Hekker, S., & Christensen-Dalsgaard, J. 2017, A&A Rev, 25, 1 (cited on page 52)

Henyey, L., Vardya, M. S., & Bodenheimer, P. 1965, ApJ, 142, 841 (cited on page 59)

Hinkle, K., Wallace, L., Valenti, J., & Harmer, D. 2000, Visible and Near Infrared Atlas of the Arcturus Spectrum 3727-9300 A (cited on page 121)

Houdek, G. 2010, Ap&SS, 328, 237 (cited on page 97)

Houdek, G., Balmforth, N. J., Christensen-Dalsgaard, J., & Gough, D. O. 1999, A&A, 351, 582 (cited on pages 11, 25, 41, 45, 48, 51, and 97)

Houdek, G., & Dupret, M.-A. 2015, Living Reviews in Solar Physics, 12, 8 (cited on pages 8, 11, 25, 40, 41, 70, 77, 87, and 94)

Houdek, G., & Gough, D. O. 2007, MNRAS, 375, 861 (cited on page 9)

Houdek, G., Lund, M. N., Trampedach, R., et al. 2019, MNRAS, 487, 595 (cited on pages xiii, 49, 51, 62, 80, and 128)

Houdek, G., Trampedach, R., Aarslev, M. J., & Christensen-Dalsgaard, J. 2017, MNRAS, 464, L124 (cited on pages 20, 34, and 131)

Houdek, G., Chaplin, W. J., Appourchaux, T., et al. 2001, MNRAS, 327, 483 (cited on page 74)

Howell, S. B., Sobeck, C., Haas, M., et al. 2014, PASP, 126, 398 (cited on page 97)

Huber, D., Bedding, T. R., Arentoft, T., et al. 2011a, ApJ, 731, 94 (cited on pages 74, 96, and 97)

Huber, D., Bedding, T. R., Stello, D., et al. 2011b, ApJ, 743, 143 (cited on page 48)

Huber, D., Zinn, J., Bojsen-Hansen, M., et al. 2017, ApJ, 844, 102 (cited on page 13)

Huber, D., Basu, S., Beck, P., et al. 2019, arXiv e-prints, arXiv:1903.08188 (cited on pages 14 and 96)

Iglesias, C. A., & Rogers, F. J. 1996, ApJ, 464, 943 (cited on page 58)

Irwin, A. W. 2012, FreeEOS: Equation of State for stellar interiors calculations, ascl:1211.002 (cited on page 55)

Jørgensen, A. C. S., Mosumgaard, J. R., Weiss, A., Silva Aguirre, V., & Christensen-Dalsgaard, J. 2018, MNRAS, 481, L35 (cited on page 20)

Jørgensen, A. C. S., & Weiss, A. 2019, MNRAS, 488, 3463 (cited on page 59)

Jørgensen, A. C. S., Weiss, A., Mosumgaard, J. R., Silva Aguirre, V., & Sahlholdt, C. L. 2017, MNRAS, 472, 3264 (cited on pages 20, 34, and 131)

Joyce, M., & Chaboyer, B. 2018, ApJ, 856, 10 (cited on pages 16 and 81)

Kallinger, T., Weiss, W. W., Barban, C., et al. 2010, A&A, 509, A77 (cited on page 13)

Kallinger, T., De Ridder, J., Hekker, S., et al. 2014, A&A, 570, A41 (cited on pages 54 and 113)

Kippenhahn, R., & Weigert, A. 1990, Stellar Structure and Evolution (cited on page 2)

Kjeldsen, H., & Bedding, T. R. 1995, A&A, 293, 87 (cited on pages xiv, 12, 24, 48, 66, 72, 77, 96, 97, and 124)

Kjeldsen, H., Bedding, T. R., Viskum, M., & Frand sen, S. 1995, AJ, 109, 1313 (cited on page 9)

Kjeldsen, H., Bedding, T. R., Baldry, I. K., et al. 2003, AJ, 126, 1483 (cited on page 96)

Kjeldsen, H., Bedding, T. R., Butler, R. P., et al. 2005, ApJ, 635, 1281 (cited on pages 10, 14, and 96)

Kjeldsen, H., Bedding, T. R., Arentoft, T., et al. 2008, ApJ, 682, 1370 (cited on pages xiii, 42, 44, 45, 72, 123, and 124)

Kritsuk, A. G., Nordlund, Å., Collins, D., et al. 2011, ApJ, 737, 13 (cited on page 18)

Kumar, P., Goldreich, P., & Kerswell, R. 1994, ApJ, 427, 483 (cited on page 71)

Kurucz, R. L. 1979, ApJS, 40, 1 (cited on page 16)

—. 2005, Memorie della Societa Astronomica Italiana Supplementi, 8, 189 (cited on pages xvi and 111)

Landau, L. D., & Lifshitz, E. M. 1987, Fluid Mechanics (cited on page 104)

Langanke, K., & Martínez-Pinedo, G. 2000, Nuclear Physics A, 673, 481 (cited on page 58)

Leenaarts, J., & Carlsson, M. 2009, Astronomical Society of the Pacific Conference Series, Vol. 415, MULTI3D: A Domain-Decomposed 3D Radiative Transfer Code, ed. B. Lites, M. Cheung, T. Magara, J. Mariska, & K. Reeves, 87 (cited on page 114)

Leighton, R. B., Noyes, R. W., & Simon, G. W. 1962, ApJ, 135, 474 (cited on page 8)

Li, G., Van Reeth, T., Bedding, T. R., Murphy, S. J., & Antoci, V. 2019, MNRAS, 487, 782 (cited on page 7)

Li, Y., Bedding, T. R., Li, T., et al. 2020, MNRAS, 495, 2363 (cited on pages xiv, 53, 64, 65, and 109)

Lomb, N. R. 1976, Ap&SS, 39, 447 (cited on page 107)

Ludwig, H.-G., Freytag, B., & Steffen, M. 1999, A&A, 346, 111 (cited on pages 16, 20, and 81)

Lund, M. N. 2019, MNRAS, 489, 1072 (cited on pages xix, 110, 112, 113, 125, and 129)

Lund, M. N., Silva Aguirre, V., Davies, G. R., et al. 2017, ApJ, 835, 172 (cited on pages xiii, xiv, 48, 49, 50, 51, 61, 62, 63, 66, 71, and 109)

Lundkvist, M. S., Ludwig, H.-G., Collet, R., & Straus, T. 2021, MNRAS, 501, 2512 (cited on page 109)

Magic, Z. 2014, PhD thesis, Max Planck Institute for Astrophysics (cited on pages xi and 17)

Magic, Z., Collet, R., Asplund, M., et al. 2013a, A&A, 557, A26 (cited on pages 27, 46, 53, 55, 58, 80, 81, 99, and 132)

Magic, Z., Collet, R., Hayek, W., & Asplund, M. 2013b, A&A, 560, A8 (cited on pages 77 and 106)

Magic, Z., Weiss, A., & Asplund, M. 2015, A&A, 573, A89 (cited on pages 16, 20, 59, and 81)

Mayor, M., Pepe, F., Queloz, D., et al. 2003, The Messenger, 114, 20 (cited on page 14)

Michel, E., Samadi, R., Baudin, F., et al. 2009, A&A, 495, 979 (cited on pages 110, 123, 125, and 129)

Michel, E., Baglin, A., Auvergne, M., et al. 2008, Science, 322, 558 (cited on pages 7, 24, 48, and 96)

Mihalas, D., Dappen, W., & Hummer, D. G. 1988, ApJ, 331, 815 (cited on pages 19, 25, 53, and 99)

Mosser, B., Belkacem, K., Goupil, M. J., et al. 2010, A&A, 517, A22 (cited on page 13)

Mosser, B., Goupil, M. J., Belkacem, K., et al. 2012a, A&A, 540, A143 (cited on page 24)

—. 2012b, A&A, 548, A10 (cited on page 48)

Mosumgaard, J. R., Ball, W. H., Silva Aguirre, V., Weiss, A., & Christensen-Dts alsgaard, J. 2018, MNRAS, 478, 5650 (cited on pages 20, 58, and 59)

Muthsam, H. J., Kupka, F., Löw-Baselli, B., et al. 2010, New Astronomy, 15, 460 (cited on page 18)

Neckel, H. 1999, SoPh, 184, 421 (cited on pages xvii and 115)

Nordlund, A. 1982, A&A, 107, 1 (cited on pages 19, 27, 53, and 99)

—. 1985, SoPh, 100, 209 (cited on page 20)

Nordlund, Å., & Galsgaard, K. 1995, Tech. rep., Astronomical Observatory, Copenhagen University (cited on pages 18, 25, 53, 91, and 99)

Nordlund, A., & Stein, R. F. 1998, in IAU Symposium, Vol. 185, New Eyes to See Inside the Sun and Stars, ed. F.-L. Deubner, J. Christensen-Dalsgaard, & D. Kurtz, 199 (cited on pages 40 and 55)

Nordlund, Å., & Stein, R. F. 2001, ApJ, 546, 576 (cited on pages 12, 20, 25, 29, 48, 70, 81, 86, 87, and 127)

Nordlund, Å., Stein, R. F., & Asplund, M. 2009, Living Reviews in Solar Physics, 6, 2 (cited on pages 16, 74, and 114)

North, J. R., Davis, J., Bedding, T. R., et al. 2007, MNRAS, 380, L80 (cited on page 52)

Oda, T., Hino, M., Muto, K., Takahara, M., & Sato, K. 1994, Atomic Data and Nuclear Data Tables, 56, 231 (cited on page 58)

Papaloizou, J., & Pringle, J. E. 1978, MNRAS, 182, 423 (cited on page 5)

Paxton, B., Bildsten, L., Dotter, A., et al. 2011, ApJS, 192, 3 (cited on pages 16, 55, 58, and 60)

Paxton, B., Cantiello, M., Arras, P., et al. 2013, ApJS, 208, 4 (cited on page 55)

Paxton, B., Marchant, P., Schwab, J., et al. 2015, ApJS, 220, 15 (cited on page 55)

Pereira, T. M. D., Asplund, M., Collet, R., et al. 2013, A&A, 554, A118 (cited on pages 28 and 114)

Plez, B. 2012, Turbospectrum: Code for spectral synthesis, ascl:1205.004 (cited on page 118)

Prša, A., Harmanec, P., Torres, G., et al. 2016, AJ, 152, 41 (cited on pages xix, 27, and 98)

Reggiani, H., Amarsi, A. M., Lind, K., et al. 2019, A&A, 627, A177 (cited on pages 114 and 117)

Rempel, M., Schüssler, M., Cameron, R. H., & Knölker, M. 2009, Science, 325, 171 (cited on page 20)

Ricker, G. R., Winn, J. N., Vanderspek, R., et al. 2015, Journal of Astronomical Telescopes, Instruments, and Systems, 1, 014003 (cited on pages 7, 24, 48, and 96)

Rosenthal, C. S., Christensen-Dalsgaard, J., Nordlund, Å., Stein, R. F., & Trampedach, R. 1999, A&A, 351, 689 (cited on pages 20, 31, and 34)

Rutten, R. J. 2003, Radiative Transfer in Stellar Atmospheres (cited on page 122)

Ryabchikova, T., Piskunov, N., Kurucz, R. L., et al. 2015, Physica Scripta, 90, 054005 (cited on page 118)

Sahlholdt, C. L., Feltzing, S., Lindegren, L., & Church, R. P. 2019, MNRAS, 482, 895 (cited on page 52)

Samadi, R., Belkacem, K., Goupil, M. J., Dupret, M.-A., & Kupka, F. 2008, A&A, 489, 291 (cited on page 24)

Samadi, R., Georgobiani, D., Trampedach, R., et al. 2007, A&A, 463, 297 (cited on pages xiv, 12, 27, 55, 75, 76, 77, 82, and 129)

Samadi, R., & Goupil, M.-J. 2001, A&A, 370, 136 (cited on pages 12, 24, 29, and 48)

Samadi, R., Nordlund, Å., Stein, R. F., Goupil, M. J., & Roxburgh, I. 2003, A&A, 404, 1129 (cited on page 12)

Sansonetti, J. E. 2008, Journal of Physical and Chemical Reference Data, 37, 7 (cited on page 117)

Sato, B., Izumiura, H., Toyota, E., et al. 2007, ApJ, 661, 527 (cited on page 97)

Scargle, J. D. 1982, ApJ, 263, 835 (cited on page 107)

Schmid, V. 2018, PhD thesis, KU Leuven (cited on pages xi and 6)

Schutz, B. F. 1979, ApJ, 232, 874 (cited on page 85)

Shapiro, S. L., & Teukolsky, S. A. 1983, Black holes, white dwarfs, and neutron stars : the physics of compact objects (cited on pages 83 and 84)

Silva Aguirre, V., Casagrande, L., Basu, S., et al. 2012, ApJ, 757, 99 (cited on page 49)

Silva Aguirre, V., Lund, M. N., Antia, H. M., et al. 2017, ApJ, 835, 173 (cited on pages 49 and 51)

Sonoi, T., Samadi, R., Belkacem, K., et al. 2015, A&A, 583, A112 (cited on page 20)

Stein, R., Georgobiani, D., Trampedach, R., Ludwig, H.-G., & Nordlund, Å. 2004, SoPh, 220, 229 (cited on pages 12, 38, 75, and 128)

Stein, R. F., & Leibacher, J. 1974, ARA&A, 12, 407 (cited on page 9)

Stein, R. F., & Nordlund, A. 1989, ApJL, 342, L95 (cited on page 20)

Stein, R. F., & Nordlund, Å. 1991, in Lecture Notes in Physics, Berlin Springer Verlag, Vol. 388, Challenges to Theories of the Structure of Moderate-Mass Stars, ed. D. Gough & J. Toomre, 195 (cited on page 41)

Stein, R. F., & Nordlund, Å. 1998, ApJ, 499, 914 (cited on pages 20, 28, and 91)

—. 2001, ApJ, 546, 585 (cited on pages 12, 20, 25, 30, 48, 70, 75, 81, 85, 127, and 128)

Stello, D., Bruntt, H., Preston, H., & Buzasi, D. 2008, ApJL, 674, L53 (cited on page 13)

Stello, D., Huber, D., Grundahl, F., et al. 2017, MNRAS, 472, 4110 (cited on page 97)

Thompson, S. E., Fraquelli, D., Van Cleve, J. E., & Caldwell, D. A. 2016, Kepler Archive Manual, Kepler Science Document KDMC-10008-006 (cited on pages xvi, 111, and 112)

Tian, Z. J., Bi, S. L., Yang, W. M., et al. 2014, MNRAS, 445, 2999 (cited on pages 49 and 50)

Trampedach, R., Aarslev, M. J., Houdek, G., et al. 2017, MNRAS, 466, L43 (cited on pages 20, 34, and 131)

Trampedach, R., Asplund, M., Collet, R., Nordlund, Å., & Stein, R. F. 2013, ApJ, 769, 18 (cited on pages 19, 25, 53, and 99)

Trampedach, R., Stein, R. F., Christensen-Dalsgaard, J., Nordlund, Å., & Asplund, M. 2014a, MNRAS, 442, 805 (cited on page 58)

Trampedach, R., Stein, R. F., Christensen-Dalsgaard, J., Nordlund, Å., & Asplund, M. 2014b, MNRAS, 445, 4366 (cited on pages 16, 20, 31, 59, and 81)

Ulrich, R. K. 1970, ApJ, 162, 993 (cited on page 8)

—. 1986, ApJ, 306, L37 (cited on pages 12 and 24)

Unno, W. 1967, PASJ, 19, 140 (cited on page 11)

Valdes, F., Gupta, R., Rose, J. A., Singh, H. P., & Bell, D. J. 2004, ApJS, 152, 251 (cited on pages xvi and 111)

Van Reeth, T., Tkachenko, A., & Aerts, C. 2016, A&A, 593, A120 (cited on pages 5 and 7)

Varenne, O., & Monier, R. 1999, A&A, 351, 247 (cited on page 58)

Verma, K., & Silva Aguirre, V. 2019, MNRAS, 489, 1850 (cited on page 58)

Vernazza, J. E., Avrett, E. H., & Loeser, R. 1981, ApJS, 45, 635 (cited on page 97)

Viani, L. S., Basu, S., Chaplin, W. J., Davies, G. R., & Elsworth, Y. 2017, ApJ, 843, 11 (cited on page 130)

Vögler, A., Shelyag, S., Schüssler, M., et al. 2005, A&A, 429, 335 (cited on page 18)

Vousden, W. D., Farr, W. M., & Mandel, I. 2016, MNRAS, 455, 1919 (cited on page 109)

Vrard, M., Kallinger, T., Mosser, B., et al. 2018, A&A, 616, A94 (cited on pages 48 and 77)

Walmswell, J. J., Tout, C. A., & Eldridge, J. J. 2015, MNRAS, 447, 2951 (cited on page 8)

White, T. R., Bedding, T. R., Stello, D., et al. 2011, ApJ, 743, 161 (cited on pages xix and 51)

Xiong, D. R., Cheng, Q. L., & Deng, L. 2000, MNRAS, 319, 1079 (cited on page 11)

Yu, J., Huber, D., Bedding, T. R., & Stello, D. 2018, MNRAS, 480, L48 (cited on pages 126 and 131)

Zhou, Y., Asplund, M., & Collet, R. 2019, ApJ, 880, 13 (cited on pages xiii, 49, 55, 61, 70, 72, 73, 75, 77, 81, 82, 85, 90, 94, and 101)

Zinn, J. C., Pinsonneault, M. H., Huber, D., et al. 2019, ApJ, 885, 166 (cited on page 13)